GRAVITATIONAL WAVE ASTROPHYSICS WITH PULSAR TIMING ARRAYS

CHIARA MARIA FRANCESCA MINGARELLI

A thesis submitted to the
University of Birmingham
for the degree of
DOCTOR OF PHILOSOPHY

Astrophysics and Space Research
School of Physics and Astronomy
College of Engineering and Physical Sciences
University of Birmingham
May 2014

DECLARATION

I declare that the work submitted in this thesis is my own. Work that is not original is cited, with a full reference given in the bibliography. Some of my own work has already been published, and this material is present in this thesis. The following is a summary of my contributions to Mingarelli et al. [2012], Mingarelli et al. [2013] and Mingarelli and Sidery (2014), in prep., which appear as Chapters in this thesis. Specifically,

- The Abstract of this thesis contains text from Mingarelli et al. [2013], Mingarelli et al. [2012] and Mingarelli and Sidery (2014), in prep.

- In Chapter 1, Section 1.5 is from Mingarelli et al. [2012] and Sections 1.5.3, 1.6, 1.7 have been taken verbatim from Mingarelli et al. [2013]. Section 1.8 is a summary of the thesis as taken from the abstracts of Mingarelli et al. [2013] , Mingarelli et al. [2012] and Mingarelli and Sidery (2014), in prep. My contributions to these research papers are listed below.

- Chapter 2 is based on: C. M. F. Mingarelli, T. Sidery, I. Mandel, A. Vecchio, "Characterizing stochastic gravitational wave background anisotropy with pulsar timing arrays", Physical Review D, Vol 88, 062005 (2013), cited as Mingarelli et al. [2013]. I am the lead author on this paper. As such I wrote the draft of this paper including the appendix. Moreover, I derived all of the generalized overlap reduction functions, examined the behaviour of the pulsar term, wrote the codes and made all of the figures. This chapter varies slightly from the published version: introductory material on stochastic gravitational wave backgrounds from Sections II and III of the

paper have been moved to the Introduction of the thesis, see above bullet point. The Appendix from Mingarelli et al. [2013] appears in this thesis as Appendix A.1.

- Chapter 3 is currently being prepared for publication in Physical Review D as "C. M. F. Mingarelli and T. Sidery, The effect of small pulsar distance variations in stochastic gravitational wave background searches with Pulsar Timing Arrays". I calculated the magnitude of the overlap reduction functions presented here, the Taylor series expansion, wrote and executed all the numerical codes used to make Table 3.1 and all the figures except for the contour plots. I wrote the draft of this paper, and all the text included here.

- Chapter 4 is based on C. M. F Mingarelli, K. Grover, R. J. E. Smith, T. Sidery, A. Vecchio, "Observing the dynamical evolution of a super massive black hole binary using Pulsar Timing Arrays", Physical Review Letters, Volume 109, Issue 8 (2012), cited as Mingarelli et al. [2012]. I am the lead author of this paper and wrote draft. Moreover, I calculated the precession rate of the orbital angular momentum and the orbital evolution timescale and velocity of the binaries. For the purposes of this thesis, I have made minor modifications to the published version of this paper. Specifically: Fig 4.2 (which I produced) has been included and equations which were previously inline are now in standard form. These changes are meant to improve the readability of the text, and were not possible in the published version due to word restrictions from Physical Review Letters. Equations which were derived in the introduction are referenced and not repeated.

CHIARA M. F. MINGARELLI, BIRMINGHAM UK, 7 MAY 2014

For my family who has always believed in me, and for children who dream of black holes, spaceships and other worlds.

Acknowledgements

I would like to express my sincerest gratitude and thanks to Alberto Vecchio, my supervisor and mentor. His help, encouragement and advice have been invaluable over the course of my PhD. Alberto played to my strengths and helped me to develop my weaknesses, and importantly, gave me projects which I could really sink my teeth into. I would also like to thank Will Farr for his frequent clear and insightful comments on my work, and my thesis examiners Ian Stevens and Ik Siong Heng for their astute and penetrating comments and questions during my viva voce exam. Their comments have without a doubt made this thesis better.

I am very much obliged to all my colleagues and friends at the University of Birmingham for making my time there very special, most of all to: Alberto Vecchio, Andreas Freise, Will Farr, Mike Cruise, Katherine Grover, Ben Aylott, Trevor Sidery, Ilya Mandel, Carl-Johan Haster, John Veitch, Christopher Berry, Ben Farr, Dan Brown, Haixing Miao, Mengyao Wang, Charlotte Bond, Will Vousden, Melissa Gillone, Richard Pearson and Maggie Lieu. Maggie, I hope you never change, except for when you become the Queen of Mars.

I also owe a great deal to Michaela Nelson, Chris Collins, Eleanor Chalkey, Stuart Aston and Ludovico Carbone for their encouragement and their help with my experimental work in the first year of my PhD. I don't recall there ever being a more beautiful (or larger!) Mach Zender interferometer :) Moreover, my genuine and sincerest thanks are owed to Andreas Freise, Yvonne Elsworth, and Eleanor Chalkley, who helped me to believe in myself in moments of doubt.

Furthermore, I would like to thank all my colleagues in the EPTA for their interest in my work, their support and constant encouragement– especially Michael

Kramer, Ben Stappers, Gemma Janssen, Rutger van Haasteren, David Champion, KJ Lee, Antoine Lassus, Stephen Taylor, Jonathan Gair, Delphine Perrodin and Marta Burgay.

A special thanks to Ingrid Stairs, Joseph Lazio, Sarah Burke-Spolaor, Michele Vallisneri, Maura McLaughlin, Joseph Romano, Andrea Lommen and Xavier Siemens, who have shown enthusiasm and interest in my work. I am very much looking forward to working with NANOGrav in the future.

For having passed on my acute caffeine addiction, I must offer my sincerest apologies to Katherine Grover, Trevor Sidery and Carl-Johan Haster. Our frequent trips to Starbucks, however, are amongst my fondest memories of my time at the University of Birmingham.

The unconditional love, support and kindness from my husband, Daniel Macleod, and my family have made this work possible. Thank you to Angelo Mingarelli and Jean Anderson, for being excellent parents who answer phone calls in the middle of the night, give me constant encouragement and support, and spoil me when I go home. Thank you to Oliviana, Giovanna, Bernardo, Giordano, Angela and Michelangelo for being the best brothers and sisters anyone has the right to ask for. My entire (very extended and large!) family have also been hugely enthusiastic about my work, especially Karen Mingarelli, Zio Marco and Zia Suzanne, Uncle Rob and Aunt Barbara, Uncle Bill, Heather Anderson, Brandon Lee, Imobach Gil Bolaños, Natalie Garside, Sarah Macleod and Laura Macleod.

Last but not in any way least, I would like to thank my dearest friends Ashlea Wells, Giorgia Monti, Katherine Grover, Brenda Murphy and Amy Miville for their love, encouragement, and moral support.

This work has been supported by the Institute of Physics, the Royal Astronomical Society and Universitas 21.

Abstract

One of the main goals of a Pulsar Timing Array (PTA)– a network of one or more radio telescopes which regularly monitor millisecond pulsars– is to detect ripples in the fabric of space-time, produced by accelerating masses, called gravitational waves (GWs). Currently, PTAs are the only way to search for GWs in the nanohertz band– a portion of the spectrum in which a promising class of sources are supermassive black hole binary (SMBHB) systems with masses in the range of $\sim 10^7 - 10^9\ M_\odot$ during their slow, adiabatic inspiral phase. The majority of the sources in the PTA frequency band are individually unresolvable, but together, these sources contribute to a stochastic GW background which may soon be detectable.

The focus of this research begins on the stochastic GW background. It is shown that a level of anisotropy in the stochastic GW background may be present and that the characterization of the GW energy density at different angular scales carries important information. The standard analysis for isotropic backgrounds is then generalized by decomposing the angular distribution of the GW energy density into multipole moments. Generalized overlap reduction functions are computed for a generic level of anisotropy and PTA configuration.

Following this, a rigorous analysis is done of the assumptions made when calculating the standard overlap reduction functions. It is shown that for all the overlap reduction functions, correlated phase changes introduce previously unmodelled effects for pulsars pairs that are separated by less than a radiation wavelength.

The research then turns to the study of continuous GW sources from SMBHBs.

Here it shown that the detection of gravitational radiation from individually resolvable SMBHB systems can yield direct information about the masses and spins of the black holes, provided that the GW-induced timing fluctuations both at the pulsar and at Earth are detected. This in turn provides a map of the nonlinear dynamics of the gravitational field and a new avenue to tackle open problems in astrophysics connected to the formation and evolution of SMBHs.

Contents

List of Figures

LIST OF FIGURES

List of Tables

LIST OF TABLES

Chapter 1

INTRODUCTION

1.1 Gravitational Waves

Gravitational waves (GWs) are *ripples* of space-time travelling at the speed of light, originating from some of the most violent events in the Universe. In particular, they provide a new means for studying black holes and addressing open questions in astrophysics and fundamental physics: from their formation, evolution and demographics, to the assembly history of galactic structures and the dynamical behaviour of gravitational fields in the strong non-linear regime. Specifically, GW observations through a network of radio pulsars used as ultra-stable clocks called a Pulsar Timing Array (PTA), cf. Detweiler [1979]; Estabrook and Wahlquist [1975]; Sazhin [1978], currently represent the only *direct* observational avenue for the study of individual supermassive black hole binary (SMBHB) systems in the $\sim 10^8 - 10^9 M_\odot$ mass range, with orbital periods between ~ 1 month and a few years. Moreover, the incoherent superposition of the cosmic population of SMBHBs is expected to form a diffusive GW background, which has yet

to be detected, cf. Demorest et al. [2013]; Hellings and Downs [1983]; Jaffe and Backer [2003]; Jenet et al. [2006]; Rajagopal and Romani [1995]; Sesana et al. [2004, 2008]; van Haasteren et al. [2011]; Wyithe and Loeb [2003].

Ongoing observations with some of the most sensitive radio telescopes around the world, detailed in Ferdman et al. [2010]; Hobbs et al. [2010]; Jenet et al. [2009]; Verbiest et al. [2010] for example, as well as instrumental improvements culminating with the Square Kilometre Array, cf. SKA [2014], are expected to yield the necessary timing precision to observe the stochastic GW background, cf. Liu et al. [2011]; Verbiest et al. [2009]. In addition to stochastic GW background searches, searches for SMBHBs which are sufficiently high mass and high frequency to rise above the background radiation are also underway, e.g. Babak and Sesana [2012]; Ellis et al. [2012a,b]; Jenet et al. [2004]; Lee et al. [2011]; Sesana and Vecchio [2010]; Sesana et al. [2009]; Wen et al. [2011]; Yardley et al. [2010].

1.1.1 Evidence for Gravitational Waves

The discovery of pulsar PSR B1913 + 16 – a pulsar with a companion neutron star– by Hulse and Taylor in 1974 was the first instance where compact objects in a relativistic system could be monitored. Hulse and Taylor [1975] claimed that the binary should be emitting GWs, and consequently, the binary's orbital period P_b should shrink by an amount $\dot{P}_b$ due to the energy loss from gravitational radiation. This would in turn change the time of periastron of the binary, i.e. the point of closest approach, which was observed via radio observations of the pulsar at the Arecibo Radio Telescope by Taylor and Weisberg [1982], see Fig 1.1. They

showed that $\dot{P}_b/(\dot{P}_b)_{\rm GR} = 1.0013(21)$, where $(\dot{P}_b)_{\rm GR}$ is the prediction of $\dot{P}_b$ from GR. One can see that these quantities are in excellent agreement. This has been hailed as the first discovery of gravitational wave emission, and for this, Hulse and Taylor were awarded Nobel prize in 1993, see Nobelprize.org [1993]. More recently, the highly relativistic double pulsar PSR J0737 − 3039A/B, see Burgay et al. [2003]; Lyne et al. [2004a], has yielded constraints on GR which surpass those of Taylor and Weisberg [1982] by an order of magnitude, see e.g. Kramer and Wex [2009] and references therein.

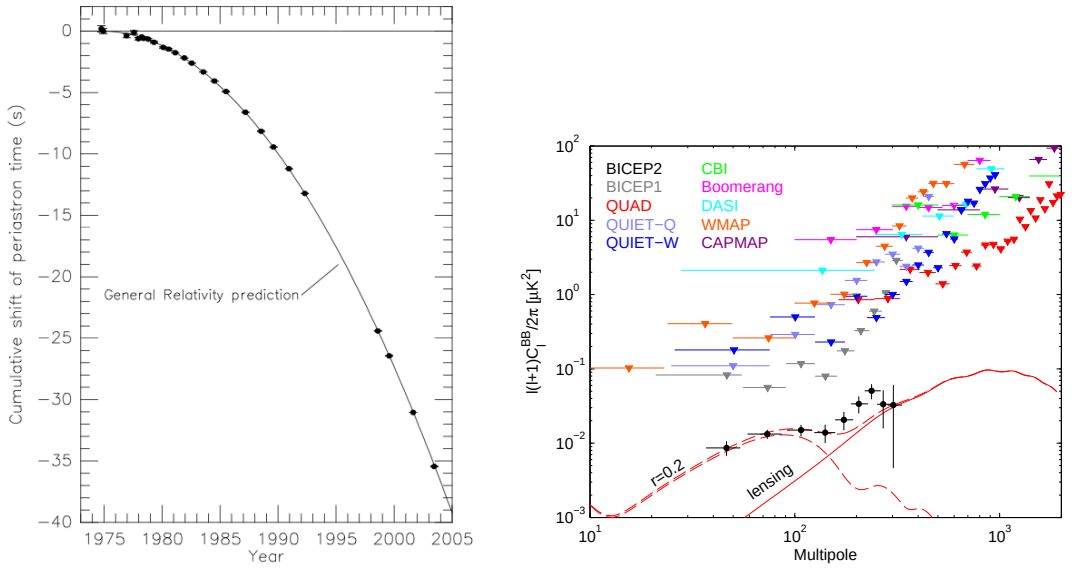

(a) Evidence for GWs, PSR 1913 + 16 (b) Evidence for primordial GWs from BICEP2

Figure 1.1: Left: Evidence for GWs form the change in the periastron of PSR 1913 + 16, updated in Weisberg and Taylor [2005]. Experimental data are the filled circles, error bars are half a percent, and the solid line is the change in periastron according to the gravitational wave emission model proposed by General Relativity. Right: evidence for B-modes in the CMB polarization. Upper triangles represent previous upper limits from other experiments, BICEP2 results are the black circles. Figure reproduced from BICEP2 Collaboration et al. [2014].

The Background Imaging of Cosmic Extragalactic Polarization (BICEP) Col-

laboration claim to have detected primordial GW signatures, called B-modes, in the polarization of the Cosmic Microwave Background (CMB), cf. BICEP2 Collaboration et al. [2014]. The BICEP2 instrument was designed to measure the polarization of the CMB on angular scales of 1 to 5 degrees ($l = 40 - 200$), near the expected peak of the B-mode polarization signature of primordial GWs from cosmic inflation BICEP2 Collaboration et al. [2014]; Guth [1981]; Linde [1982]. Cosmological B-modes also come from gravitational lensing of polarization by the large-scale structure of the universe, see e.g. Zaldarriaga and Seljak [1998], occurring at much higher angular scales, $l \sim 10^3$. These B-modes were discovered in 2013 by the South Pole Telescope collaboration, cf. Hanson et al. [2013]. The BICEP2 researchers also reported a relatively large number for r: the ratio of the GW fluctuations in the CMB to the fluctuations caused by perturbations in the density of matter. This quantity is especially interesting, as it is determined by the energy scale of inflation, see BICEP2 Collaboration et al. [2014] for details. The previous upper limits this ratio was $r < 0.11$, based on all-sky CMB maps from the Wilkinson Microwave Anisotropy Probe (WMAP) and the Planck Collaboration, see Planck Collaboration et al. [2013]. BICEP2's value, however, is around $r \sim 0.20$, in contention with previous upper limits. At the time of writing, there is some contention as to whether or not the BICEP2 collaboration have underestimated the galactic foreground emission, as discussed by Falkowski [2014], which may affect the value of r.

Confirmation of BICEP2's findings may be possible via other CMB experiments such as Planck, a European space-based CMB mission e.g. Planck Collaboration et al. [2013], the Atacama B-mode Search (ABS), e.g. Sievers and ABS Collaboration [2014] and POLARBEAR, e.g. The POLARBEAR Collaboration

et al. [2014].

1.1.2 Useful Definitions and Conventions

Before moving forward, a list of common definitions and equations is presented for ease of reference.

Useful definitions

The following are commonly used formulae which will be used throughout the text. Unless otherwise specified, natural units of $c = G = 1$ are used. Therefore,

$$1 \text{ s} = 299,792,458 \text{ m} \sim 3 \times 10^8 \text{ m}, \tag{1.1}$$

and by using the Schwarzschild radius of the sun, $r_S = GM_\odot/c^2 \sim 1480$ m, one can write the mass of the sun in units of seconds:

$$1 \ M_\odot = \frac{r_S}{c} = \frac{GM_\odot}{c^3} \sim 4.9 \ \mu\text{s}. \tag{1.2}$$

Common units used in this research are the light year, denoted "ly", where

$$1 \text{ ly} = 9.4 \times 10^{15} \text{ m} \sim 3.2 \times 10^7 \text{s}\,, \tag{1.3}$$

and the parsec, denoted "pc", where

$$1 \text{ pc} = 3.3 \text{ ly} \sim 10^8 \text{ s}\,. \tag{1.4}$$

Other useful definitions include the **total mass** M of a binary with component masses m_1, m_2:

$$M = m_1 + m_2, \tag{1.5}$$

the **reduced mass**, μ

$$\mu = \frac{m_1 m_2}{M}, \tag{1.6}$$

the **symmetric mass ratio** η,

$$\eta = \frac{m_1 m_2}{M^2}, \tag{1.7}$$

and the **chirp mass** $\mathcal{M}$

$$\mathcal{M}^{5/3} = m_1 m_2 M^{-1/3} = \mu M^{2/3}. \tag{1.8}$$

Useful forms of Kepler's 3rd Law.

Consider a binary system in a circular orbit with total mass M at orbital separation r and period P. One can write Kepler's 3rd Law as:

$$\left(\frac{2\pi}{P}\right)^2 = \frac{M}{r^3}, \tag{1.9}$$

$$(2\pi f)^2 = \frac{M}{r^3}, \tag{1.10}$$

where $P = 1/f$ and f is the orbital frequency of the binary. The velocity v of the binary can be expressed in terms of the orbital frequency as

$$v = \frac{2\pi r}{P} = 2\pi r f, \tag{1.11}$$

where $2\pi r$ is the circumference of a circle with radius r. Hence,

$$r = \frac{v}{2\pi f} \,. \tag{1.12}$$

Substituting Eq (1.12) into Eq (1.10) and using the fact that $f_{\rm GW} = 2f_{\rm orb}$, see Eq (1.57), one can write

$$\begin{aligned} (\pi f_{\rm GW})^2 &= \frac{M}{v^3} (\pi f_{\rm GW})^3 \,, \\ v &= (\pi M f_{\rm GW})^{1/3} \,. \end{aligned} \tag{1.13}$$

Anther useful manipulation of Eq (1.10) is

$$r = M^{1/3} \pi^{-2/3} f_{\rm GW}^{-2/3} \,. \tag{1.14}$$

1.1.3 Linearized Field Equations

> *Matter tells space how to curve, and space tells matter how to move.*
>
> $\sim$ John A. Wheeler

Einstein's theory of General Relativity (GR) introduced a new way of thinking about gravity, which was fundamentally different from the Newtonian paradigm. In this section the linearized field equations will be derived and the GW solution in a vacuum will be given. Furthermore, it will be shown that GWs have two polarizations and travel at the speed of light. Several excellent texts on the subject have been written, including Flanagan and Hughes [2005]; Hawking and Israel [1987]; Misner et al. [1973]; Schutz and Ricci [1999], which can be consulted

for more details.

Mathematically, Einstein's field equations are written as a tensor equation,

$$R_{\mu\nu} - \frac{1}{2} g_{\mu\nu} R = 8\pi T_{\mu\nu}, \qquad \mu, \nu = 0, 1, 2, 3, 4 \tag{1.15}$$

where $R_{\mu\nu}$ is the Ricci tensor, R is the scalar curvature, $g_{\mu\nu}$ is the metric tensor and $T_{\mu\nu}$ is the stress-energy tensor. A more compact form of the field equations is sometimes used, where the right-hand side is rewritten as the so-called "Einstein tensor", $G_{\mu\nu}$ such that

$$G_{\mu\nu} = 8\pi T_{\mu\nu}. \tag{1.16}$$

In the above form of the field equations, it is perhaps clearer that the stress-energy tensor $T_{\mu\nu}$ at a given event generates curvature $G_{\mu\nu}$ at the same event.

Gravitational waves arise a natural solutions to the field equations. The cleanest way to show this is to make a few simplifying assumptions: assume a flat background metric $\eta_{\mu\nu}$ and a small perturbation to this metric $h_{\mu\nu} \ll \eta_{\mu\nu}$. In the presence of this small metric perturbation, $g_{\mu\nu}$ can be written as

$$g_{\mu\nu} = \eta_{\mu\nu} + h_{\mu\nu}, \tag{1.17}$$

where $\eta_{\mu\nu}$ is the flat Minkowski metric, $\mathrm{diag}(-1, 1, 1, 1)$. Writing the metric tensor as a sum of a flat space-time and a small perturbation is called the "linear approximation", and is correct to first order in $h_{\mu\nu}$. The indices for the metric perturbation are raised and lowered by $\eta_{\mu\nu}$:

$$h^{\mu\nu} = \eta^{\mu\rho}\eta^{\nu\sigma} h_{\rho\sigma}. \tag{1.18}$$

Let $h = \eta_{\mu\nu}h^{\mu\nu}$. The following math is simpler if the "trace-reversed" metric perturbation[1], $\bar{h}_{\mu\nu}$ is used, where

$$\bar{h}_{\mu\nu} = h_{\mu\nu} - \frac{1}{2}\eta_{\mu\nu}h. \tag{1.19}$$

The coordinate freedom in the $h_{\mu\nu}$ components is still considerable: $h_{\mu\nu}$, like the metric tensor, is a 4×4 matrix with 16 components. However, both $g_{\mu\nu}$ and $h_{\mu\nu}$ are symmetric and therefore have 10 independent components. To restrict some the degrees of freedom, we impose the gauge condition

$$\partial_\nu \bar{h}^{\mu\nu} = 0, \tag{1.20}$$

called the Lorentz gauge (also called the de Donder gauge), where ∂_ν is partial differentiation with respect to x^ν. The choice of this gauge applies 4 independent conditions to 10 independent components of $h_{\mu\nu}$, reducing the freedom to 6.

Substituting Eq (1.19) into Eq (1.16) under the Lorentz gauge conditions, Eq (1.20), yields a rather simple result,

$$G_{\mu\nu} = -\frac{1}{2}\left(-\frac{\partial^2}{\partial t^2} + \nabla^2\right)\bar{h}_{\mu\nu} = -\frac{1}{2}\Box\bar{h}_{\mu\nu}, \tag{1.21}$$

where $\Box$ is the D'Alembert, or wave, operator. For more details, see e.g. Flanagan and Hughes [2005]; Misner et al. [1973]. Therefore, the linearized field equations reduce to wave equations:

$$\Box\bar{h}_{\mu\nu} = -16\pi T_{\mu\nu}. \tag{1.22}$$

[1] This is called "trace-reversed since $\bar{h}^\mu_\mu = -h$

The most straightforward solution to Eq (1.22) is the vacuum solution, where $T_{\mu\nu} = 0$,

$$\Box \bar{h}^{\mu\nu} = 0. \tag{1.23}$$

Eq (1.23) is a wave equation, and therefore admits a plane wave solution of the form

$$\bar{h}^{\mu\nu} = A\mathbf{e}_{\mu\nu} e^{ik_\alpha x^\alpha} = A\mathbf{e}_{\mu\nu} e^{i(\mathbf{k}\cdot\mathbf{x} - \omega t)}, \tag{1.24}$$

where A is the amplitude, $\mathbf{e}^{\mu\nu}$ is the polarization tensor and and k_α is the wave vector, $k^\alpha = (\omega, \mathbf{k})$. The properties of the wave vector can be derived by taking two derivatives of Eq (1.24):

$$\partial_{\alpha,\beta} h^{\mu\nu} = k_\alpha k_\beta h^{\mu\nu} \tag{1.25}$$

$$\eta^{\alpha\beta}\partial_{\alpha,\beta} h^{\mu\nu} = \eta^{\alpha\beta} k_\alpha k_\beta h^{\mu\nu}\,. \tag{1.26}$$

The lefthand side of Eq (1.26) is the wave equation, as required, if $\eta^{\alpha\beta} k_\alpha k_\beta = 0$, which is generically true if $k_\alpha k^\alpha = 0$, i.e. if $\mathbf{k}$ is light-like. One can therefore conclude that GWs propagate at the speed of light.

Recall that there are still 6 degrees of freedom left in $h_{\mu\nu}$. Indeed, it is still possible to perform a small change in coordinates

$$\bar{x}^\mu = x^\mu + \xi^\mu, \tag{1.27}$$

which preserves the Lorentz gauge condition if $\partial_\nu \xi^{\mu\nu} = 0$. It is possible, however, to remove 4 more degrees of requiring that the wave be transverse, Eq (1.28), and

traceless, Eq (1.29), i.e.

$$h^{0\mu} = 0\,, \tag{1.28}$$

$$h^{\mu}_{\mu} = 0. \tag{1.29}$$

These conditions put the metric into what's known as the Transverse and Traceless (TT) gauge. Since the metric perturbation is traceless, $\bar{h}^{TT}_{\mu\nu} = h^{TT}_{\mu\nu}$. From hereon, the metric perturbation $h^{TT}_{\mu\nu}$ will be assumed to be given in the TT gauge and will be denoted by h_{ij}, $ij = 1, 2, 3$, when referring to the spatial components only. This is a natural way of writing the metric perturbation, since the transverse condition, Eq (1.28), ensures that it is purely spatial.

There are now just two degrees of freedom remaining which cannot be fixed by a choice of gauge, and these are the GW polarizations: "plus" and "cross", whose form will be given in Sec 1.1.4, see Fig 1.2.

1.1.4 Generating Gravitational Waves: the Quadrupole Formula

The most straightforward way to derive the GW solution of the linearized field equations was to solve the the equations in a vacuum, thereby setting the source term (or the stress-energy tensor) in Eq (1.22) to zero. GWs, however, are generated by $T^{\mu\nu}$– the right hand side of Eq (1.22). In the following paragraphs, the leading order contributions to the spatial components of the metric perturbation will be calculated, in an effort to present the standard quadrupole formula for the emitted gravitational radiation. The steps here closely follow Flanagan and

Hughes [2005]; Hawking and Israel [1987]; Misner et al. [1973]; Schutz and Ricci [1999]; Shapiro and Teukolsky [1983], which may be consulted for the detailed calculations. Here boldface is used to indicate a vector.

The linearized field equations, Eq (1.22), can be solved using a well-known Green's function associated with the wave operator $\Box$,

$$G(t, \mathbf{x}; t', \mathbf{x}') = -\frac{\delta\left(t' - [t - |\mathbf{x} - \mathbf{x}'|]\right)}{4\pi|\mathbf{x} - \mathbf{x}'|}, \tag{1.30}$$

where $t - |\mathbf{x} - \mathbf{x}'|$ is called the "retarded time", which emphasizes that there is lag between points $\mathbf{x}$ and $\mathbf{x}'$, due to the finiteness of the speed of light. Applying this Green's function, Eq (1.30), to Eq (1.22) yields

$$\bar{h}_{\mu\nu}(t, \mathbf{x}) = 4 \int d^3x' \frac{T_{\mu\nu}(t - |\mathbf{x} - \mathbf{x}'|, \mathbf{x}')}{|\mathbf{x} - \mathbf{x}'|}. \tag{1.31}$$

This quantity is then evaluated far away from the source, such that $D = |\mathbf{x} - \mathbf{x}'|$. This approximation leads to a fractional error of order L_{source}/D, where L_{source} is the size of the source. For compact GW sources such as black holes, cf Sec 1.3 and neutron stars, cf Sec 1.5.1, $L_{\text{source}}/D \ll 1$. This substitution in the denominator of Eq (1.31) and in the time argument of T_{ij}:

$$T_{ij}(t - |\mathbf{x} - \mathbf{x}'|, \mathbf{x}') \approx T_{ij}(t - D, \mathbf{x}'), \tag{1.32}$$

such that

$$\bar{h}_{\mu\nu}(t, \mathbf{x}) \approx \frac{4}{D} \int d^3x' T_{ij}(t - D, \mathbf{x}'). \tag{1.33}$$

Eq (1.33) is the first term in the expansion of the gravitational radiation field. In the linearized theory, however, it is required that $\partial_\mu T^{\mu\nu} = 0$. Physically, this can

be thought of as the conservation of momentum of the system, or in other words, the stress-energy tensor must be conserved.

From the gauge condition, one can massage Eq (1.33) into the form

$$\frac{4}{D}\int d^3x' T_{ij} = \frac{2}{D}\frac{\partial^2}{\partial t^2}\int d^3x' \rho x'_i x'_j, \tag{1.34}$$

where $\rho = T_{tt}$ is the mass density. This manipulation is quite involved– the reader is referred to the careful steps outlined by Flanagan and Hughes [2005] for details.

Let I_{ij} be the quadrupole (or second) moment of the mass distribution:

$$I_{ij} \equiv \int d^3x' \rho x'_i x'_j \,. \tag{1.35}$$

Eq (1.34) relates the second time derivative of the mass quadrupole to the metric perturbation $\bar{h}_{ij}$, in the source's rest frame in a relatively simple form:

$$\bar{h}_{ij}(t, \mathbf{x}) \approx \frac{2}{D}\ddot{I}_{ij} \,. \tag{1.36}$$

Mathematically, one can now see that the second moment of the mass distribution is the lowest order contribution to the strain. The lower order contributions were eliminated based on mathematical arguments going from Eq (1.31) to (1.33), detailed in e.g. Flanagan and Hughes [2005]; Misner et al. [1973], however a physical explanation of why these terms vanish may prove enlightening.

The zeroth moment of the mass distribution M_0 is the mass itself,

$$M_0 = \int d^3x \rho = M \,. \tag{1.37}$$

The dipole (or first) mass moment is defined as

$$M_1 \equiv \int d^3x \rho x_i = M L_i \tag{1.38}$$

where L_i is a vector with dimension of length. If the mass distribution displays internal motion, then the moments of the mass current, $j_i = \rho v_i$ may also be important. The first moment of the mass current is the spin angular momentum, S_1,

$$S_1 \equiv \int d^3x \rho v_j x_k \epsilon_{ijk} = S_i \,, \tag{1.39}$$

where the cross product is written in terms of the Levi-Civita symbol, ϵ_{ijk}, which is 1 for an even permutation of ijk, -1 for an odd permutation of the indices and 0 if there is a repeated index.

The contribution to the strain h_{ij} from Eqs (1.37), (1.38), and (1.39) can now be calculated. The Green's function solution to the wave equation, Eq (1.30) tells us that the strain magnitude h scales as $1/D$. The contribution from M_0 is

$$h \sim \frac{M}{D} \,, \tag{1.40}$$

but the mass does not vary dynamically since $dM/dt = 0$. The mass monopole therefore does not contribute to the strain. Next consider the mass dipole, Eq (1.38). Its contribution to the strain would be

$$h \sim \frac{M L_i}{D}, \tag{1.41}$$

however from the conservation of momentum, it is clear that $d^2 M_1/dt^2 = 0$, and

therefore does not contribute to the strain. Similarly, the contribution from the angular momentum S_i to the strain is zero since $dS_i/dt = 0$, from conservations laws. Therefore, it the first non-vanishing contribution to the strain comes from the mass quadrupole, I_{ij}, as described in Eq (1.36).

Now, let

$$\begin{aligned} \text{Ī}_{ij} &= I_{ij} - \frac{1}{3}\delta_{ij}\,\mathrm{trace}(I), && (1.42) \\ &= \int d^3x'\rho\left(x'_i x'_j - \frac{1}{3}\delta_{ij}\,\mathrm{trace}(I)\right), && (1.43) \end{aligned}$$

be the "reduced" quadrupole moment, cf. Misner et al. [1973]. The "reduced" part refers to the 1/3 term which multiplies the trace of I.

The energy E carried away by the GWs can also be written in terms of the mass quadrupole:

$$\frac{dE}{dt} = \frac{1}{5}\left\langle \dddot{\mathbf{I}}^{\mathbf{2}} \right\rangle \equiv \frac{1}{5}\left\langle \dddot{\text{Ī}}_{ij}\,\dddot{\text{Ī}}_{ij} \right\rangle , \tag{1.44}$$

where the angled brackets represent the average value. Eq (1.44) is also called the gravitational luminosity $\mathcal{L}$ of the source.

An example from Wheeler [2013] will help to solidify these ideas. Consider a circular binary with orbital separation r, component masses m_1 and m_2, and reduced mass μ, cf. Eq (1.6). Confining the orbit of the binary to the $x-y$ plane, one may write the barycentric the coordinate as $m_1 x_1 = m_2 x_2$, where $r = x_1 + x_2$ is the orbital separation of the binary. This yields to coordinates

$$x_1 = \frac{r\mu}{m_1}(\cos\theta, \sin\theta, 0)\,, \tag{1.45}$$
$$x_2 = \frac{r\mu}{m_2}(-\cos\theta, -\sin\theta, 0), \tag{1.46}$$

where θ is the polar angle, which can be expressed in terms of the orbital frequency, $f_{\rm orb}$, as $\theta = 2\pi f_{\rm orb} t = \omega t$.

It is now straightforward to substitute the above components into Eq (1.35):

$$I^{xx} = \int \rho x_i^2 d^3x = m_1 x_1^2 + m_2 x_2^2 \tag{1.47}$$
$$= \mu^2 r^2 \left(\frac{1}{m_1} + \frac{1}{m_2}\right) \cos^2\theta \tag{1.48}$$
$$= \mu r^2 \cos^2(\omega t) \tag{1.49}$$
$$= \frac{1}{2}\mu r^2 [1 + \cos(2\omega t)]. \tag{1.50}$$

Similarly,

$$I^{yy} = \frac{1}{2}\mu r^2 [1 - \cos(2\omega t)]\,, \tag{1.51}$$
$$I^{xy} = I^{yx} = \frac{1}{2}\mu r^2 \sin(2\omega t). \tag{1.52}$$

In order to obtain the reduced quadrupole moment $\bar{I}_{ij}$, the traceless component must be subtracted, as in Eq (1.43):

$$\frac{1}{3}\delta^{ij}\delta_{lm} I^{lm} = \frac{1}{3}\delta^{ij}[I^{xx} + I^{yy}]\,, \tag{1.53}$$
$$= \frac{1}{6}\delta^{ij}\mu r^2 \left[1 + \cos(2\omega t) + 1 - \cos(2\omega t)\right]\,, \tag{1.54}$$
$$= \frac{1}{3}\delta^{ij}\mu r^2. \tag{1.55}$$

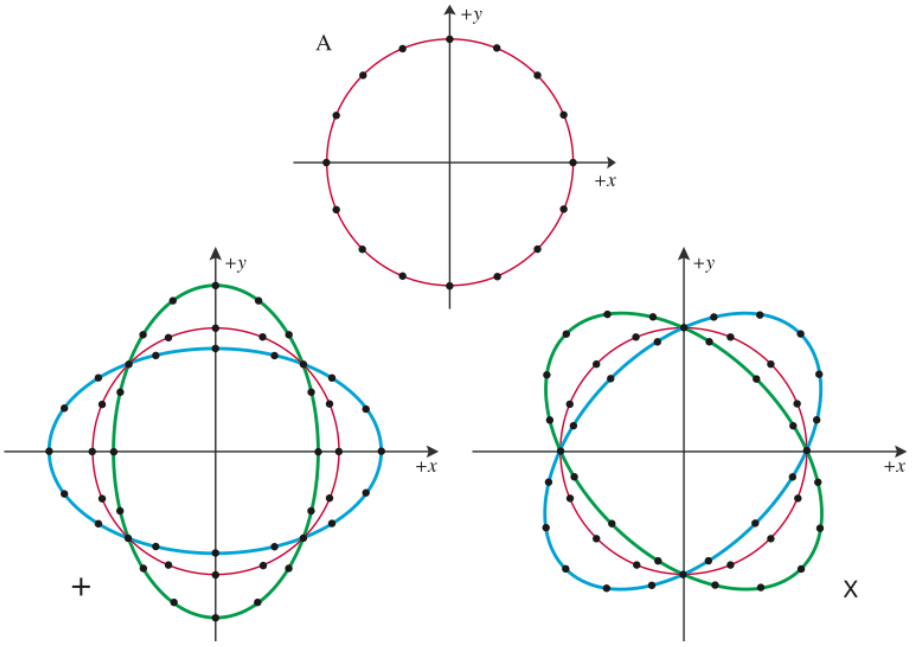

Figure 1.2: The plus and cross polarizations of a gravitational wave. A represents a circle of test masses at rest, in the absence of a GW. the lower left image is the response to a "+" polarized GW, and the lower right image is the response to a "×" polarized GW. This is the characteristic stretching and squashing of spacetime, due to a GW. Imagine reproduced from Wheeler [2013].

The matrix $\bar{I}$ can now be written down, as all of its components have been calculated:

$$\bar{I}^{ij} = \frac{1}{2}\mu r^2 \begin{bmatrix} 1/3 + \cos(2\omega t) & \sin(2\omega t) & 0 \\ \sin(2\omega t) & 1/3 - \cos(2\omega t) & 0 \\ 0 & 0 & -2/3 \end{bmatrix}. \tag{1.56}$$

The second time derivative of the mass quadrupole is of particular interest as it is related to the GW strain, Eq (1.36). Moreover, the energy E emitted in

GWs is $E = \left\langle \ddot{I}_{ij} \right\rangle$. Taking two derivatives of Eq (1.56) one can write:

$$\ddot{I}^{ij} = -2\mu r^2 \omega^2 \begin{bmatrix} \cos(2\omega t) & \sin(2\omega t) & 0 \\ \sin(2\omega t) & -\cos(2\omega t) & 0 \\ 0 & 0 & 0 \end{bmatrix} . \tag{1.57}$$

Note that the GW frequency in a circular binary is twice the orbital frequency. In other words, for each cycle made by the binary motion, the GW signal goes through two full cycles and $f_{\rm GW} = 2f_{\rm orb}$. From Eq (1.57), it is clear that the magnitude of the GW energy is

$$E = -2\mu r^2 \omega^2 \,, \tag{1.58}$$

and from Kepler's 3rd Law to relate the binary mass, angular frequency and orbital separation, cf. Sec 1.1.2, one can write the GW energy in the familiar form,

$$E = -\frac{1}{2}\frac{\mu M}{r} \,. \tag{1.59}$$

Eq (1.57) also highlights the two independent GW polarizations amplitudes, h_+ and $h_\times$, defined as

$$h_+(t) = \frac{2}{D}\left(\frac{\ddot{I}^{11} - \ddot{I}^{22}}{2}\right) = -\frac{4}{D}\mu r^2 \omega^2 \cos(2\omega t) \tag{1.60}$$

$$h_\times(t) = \frac{2}{D}\left(\frac{\ddot{I}^{12} + \ddot{I}^{21}}{2}\right) = -\frac{4}{D}\mu r^2 \omega^2 \sin(2\omega t) \,. \tag{1.61}$$

The magnitude h of a typical non-zero component of h_{ij} is readily obtained by

using Eq (1.14):

$$\begin{aligned} h &= \frac{4\omega^{2/3}\mu M^{2/3}}{D} \\ &= \frac{4}{D}\pi^{2/3} f_{\rm GW}^{2/3}\mathcal{M}^{5/3}. \end{aligned} \tag{1.62}$$

Finally, the gravitational luminosity $\mathcal{L}$ is calculated from the third time derivative of the mass quadrupole $\dddot{I}^{ij}$,

$$\dddot{I}^{ij} = -4\mu r^2\omega^3 \begin{bmatrix} -\sin(2\omega t) & \cos(2\omega t) & 0 \\ \cos(2\omega t) & \sin(2\omega t) & 0 \\ 0 & 0 & 0 \end{bmatrix}, \tag{1.63}$$

and by Eq (1.44),

$$\begin{aligned} \frac{dE}{dt} &= -\frac{1}{5}\left\langle \dddot{I}_{jk}\dddot{I}_{jk}\right\rangle \\ &= -\frac{1}{5}(4\mu r^2\omega^3)^2\left\langle 2\sin^2(2\omega t) + 2\cos^2(2\omega t)\right\rangle \qquad (1.64) \\ &= -\frac{32}{5}\frac{\mu^2 M^3}{r^5}, \qquad (1.65) \end{aligned}$$

where Kepler's 3rd Law was used to write ω in terms of mass and orbital separation.

A useful quantity which can now be derived from Eqs (1.65) and (1.59) is the change in the GW frequency per unit time, $\dot{f}_{\rm GW}$. This quantity can be derived

by taking the time derivative of Kepler's 3rd Law:

$$(\pi f_{\rm GW})^2 = \frac{M}{r^3} \tag{1.66}$$

$$2(\pi^2 f_{\rm GW})\frac{df_{\rm GW}}{dt} = -\frac{3M}{r^4}\frac{dr}{dt} \tag{1.67}$$

$$f_{\rm GW}\frac{df_{\rm GW}}{dt} = -\frac{3M}{2\pi^2}\frac{1}{r^4}\frac{dr}{dE}\frac{dE}{dt}\,, \tag{1.68}$$

but dr/dE is simply $(dE/dr)^{-1}$, which is easily calculated from Eq (1.59):

$$\frac{dE}{dr} = \frac{1}{2}\frac{\mu M}{r^2} = -\frac{E}{r}\,. \tag{1.69}$$

Substituting Eqs (1.69) and (1.65) into (1.68) yields

$$f_{\rm GW}\frac{df_{\rm GW}}{dt} = -\left(\frac{3M}{2\pi^2 r^4}\right)\left(\frac{2r^2}{\mu M}\right)\left(\frac{32}{5}\frac{\mu^2 M^3}{r^5}\right)\,. \tag{1.70}$$

Eq (1.14) was used to write r in terms of the mass and frequency of the binary, and applying the definition of chirp mass, Eq (1.8), gives the final result:

$$\frac{df_{\rm GW}}{dt} = \frac{96}{5}\pi^{8/3}\mathcal{M}^{5/3} f_{\rm GW}^{11/3}\,. \tag{1.71}$$

The expression for $f_{\rm GW}(t)$ is obtained by integrating Eq (1.71) from some time t to the time of coalescence, t_c:

$$f_{\rm GW}(t) = \pi^{-1}\mathcal{M}^{-5/8}\left[\frac{256}{5}(t_c - t)\right]^{-3/8}\,. \tag{1.72}$$

Similarly, one can derive the orbital separation of the binary at any time by writing $dE/dt = (dE/dr)(dr/dt)$ and substituting Eqs (1.65), (1.59) and (1.69).

Integrating r from some time t to the time of coalescence t_c, gives:

$$r(t) = \left(\frac{256}{5}\mu M^2\right)^{1/4} (t_c - t)^{1/4}. \tag{1.73}$$

1.2 The post-Newtonian Approximation

There are very few exact solutions to Einstein's field equations – see e.g. Stephani et al. [2003] for a collection of known exact solutions– and numerical solutions to the field equations are still very computationally demanding, e.g. Bona et al. [1995]; Centrella et al. [2010]; Pretorius [2005]. Instead of writing down the exact solution for 2-body dynamics, a perturbative expression– the so-called post-Newtonian (pN) approximation– is often used. The pN approximation is used to compute the amplitude of the GW and the evolution of the orbital phase of a compact binary. Here the perturbation parameter is the characteristic velocity v of the binary, Eq (1.13), where $v \ll 1$. Expansions in terms of other parameters, such as the mass ratio, are also used when appropriate, cf. Buonanno et al. [2009]. The order n of the expansion is denoted by $\mathrm{p}^n\mathrm{N}$, which is given in terms of $(v/c)^{2n}$. The evolution of the orbital phase during the binary's inspiral is complete to order $(v/c)^7$, see Blanchet [2014]; Buonanno et al. [2009]; Damour et al. [2009]. The Newtonian approximation is the $n = 0$ leading order term. Note that n can take on integer and half integer values, and that in General Relativity, $\mathrm{p}^{0.5}\mathrm{N} = 0$, see e.g. Blanchet [2014] and references therein.

The pN approximation for the change in GW frequency, df/dt is given by several authors, e.g. up to $\mathrm{p}^{1.5}\mathrm{N}$ by Cutler and Flanagan [1994] and up to $\mathrm{p}^2\mathrm{N}$ by Blanchet et al. [1995]; Poisson and Will [1995]. Consider a compact binary with

GW frequency f, component masses m_1, m_2 at a distance D from the observer. From Eq (1.57), one can write the GW strain as

$$h \sim A\cos(\pi f_{\rm GW} t), \tag{1.74}$$

where $A \sim f_{\rm GW}^{2/3}\mathcal{M}^{5/3}Q(\text{angles})/D$ is the GW amplitude, cf. Eq (1.62), and $Q(\text{angles})$ contains the geometric parameters of the binary (right asenction, declination, orbital inclination). If the total angular momentum of the binary is $\hat{\mathbf{L}}$, and each compact object has a spin $\hat{\mathbf{S}}_1$, $\hat{\mathbf{S}}_2$, the pN approximation for the change in the GW frequency $\dot{f}_{\rm GW}$ to p^{2}N order is

$$\frac{df_{\rm GW}}{dt} = \frac{96}{5}\pi^{8/3}\mathcal{M}^{5/3}f_{\rm GW}^{11/3}\left[1-\left(\frac{743}{336}+\frac{11}{4}\eta\right)(\pi M f_{\rm GW})^{2/3}+(4\pi-\beta)(\pi M f_{\rm GW})\right.$$
$$\left.+\left(\frac{34103}{18144}+\frac{13661}{2016}\eta+\frac{59}{18}\eta^2+\sigma\right)(\pi M f_{\rm GW})^{4/3}+\cdots\right] \tag{1.75}$$

where

$$\beta = \frac{1}{12}\sum_{i=1}^{2}\left[113\left(\frac{m_i}{M}\right)^2+75\eta\right]\hat{\mathbf{L}}\cdot\hat{\mathbf{S}}_i\,, \tag{1.76}$$

$$\sigma = \frac{\eta}{48}\left[-247\left(\hat{\mathbf{S}}_1\cdot\hat{\mathbf{S}}_2\right)+721\left(\hat{\mathbf{L}}\cdot\hat{\mathbf{S}}_1\right)\left(\hat{\mathbf{L}}\cdot\hat{\mathbf{S}}_2\right)\right]. \tag{1.77}$$

For more details on this, the "Taylor F2" expansion, see e.g. Blanchet [2014]; Buonanno et al. [2009]. Note that the chirp mass $\mathcal{M}$ dominates the Newtonian contribution, and the symmetric mass ratio η enters the expansion at p^{1}N. Contributions from the spins enter at p$^{1.5}$N via the β term, hence this order is usually called the "spin-orbit" coupling. In this case, the coupling is between the spin of

the compact object and the orbital angular momentum, $\hat{\mathbf{L}} \cdot \hat{\mathbf{S}}_i$. The p^{2}N contribution is called the "spin-spin" contribution, as this term includes the interaction of the binary's spins with each other, $\hat{\mathbf{S}}_1 \cdot \hat{\mathbf{S}}_2$.

The maximum value of Eq (1.76) is achieved for an equal mass binary when its spins $\hat{\mathbf{S}}_i$ are aligned with the orbital angular momentum $\hat{\mathbf{L}}$, such that

$$\beta_{\rm max} = \frac{2}{12}\left[113\left(\frac{1}{2}\right)^2 + 75\left(\frac{1}{4}\right)\right] = \frac{47}{6} \approx 7.83. \tag{1.78}$$

The maximum value of Eq (1.77), σ, is also achieved for an equal mass binary with spins aligned with the total angular momentum:

$$\sigma_{\rm max} = \frac{1}{48}\frac{1}{4}\left(-247 + 721\right) = \frac{474}{192} \approx 2.47\,. \tag{1.79}$$

The pN approximation is truncated at p^{2}N since higher order terms will be further suppressed by factors of v^{2n}. Recall from Eqs (1.13) and (1.75) that

$$v_{\rm p^1N} = (\pi M f_{\rm GW})^{2/3} \approx 8.4\times10^{-3}\left(\frac{M}{10^9 M_\odot}\right)^{2/3}\left(\frac{f_{\rm GW}}{50\ {\rm nHz}}\right)^{2/3}, \tag{1.80}$$

$$v_{\rm p^{1.5}N} = (\pi M f_{\rm GW}) \approx 7.7\times10^{-4}\left(\frac{M}{10^9 M_\odot}\right)\left(\frac{f_{\rm GW}}{50\ {\rm nHz}}\right), \tag{1.81}$$

$$v_{\rm p^2N} = (\pi M f_{\rm GW})^{4/3} \approx 7.1\times10^{-5}\left(\frac{M}{10^9 M_\odot}\right)^{4/3}\left(\frac{f_{\rm GW}}{50\ {\rm nHz}}\right)^{4/3}. \tag{1.82}$$

A multiplicative factor of $(4\pi - \beta) \sim 5$, Eq (1.75), boosts the contribution to the p$^{1.5}$N term, for optimal β, cf. Eq (1.76), to $\sim 10^{-3}$, which is comparable to the p^{1}N term. For optimal alignments and mass ratios, the p^{2}N contribution gains an additional factor of order 10, cf. Eqs (1.75) and (1.77), however, it is still at

least an order of magnitude smaller than the $p^{1.5}N$ contribution.

1.3 Supermassive Black Holes

Supermassive black holes (SMBHs) in the range $10^6 - 10^9\ M_\odot$ are found in the centres of most nearby galaxies, cf. e.g. Ferrarese and Ford [2005]; Magorrian et al. [1998]. Moreover, studies by e.g. Ghez et al. [2005] indicate that the centre of our own Milky Way hosts a $\sim 4 \times 10^6\ M_\odot$ SMBH, see e.g. the review by Genzel et al. [2010]. The focus of this section will be on SMBH binaries, and how galaxy mergers– and therefore SMBHB mergers– can lead to GWs in the PTA band.

The origin of SMBHs is still a very active area of research: there are currently three main competing theories on their formation, with the SMBH progenitors commonly referred to as "seeds", e.g. Volonteri [2010], which are summarized in Fig 1.3. The first theory proposes that SMBH seeds form from Pop III stars which collapse into BHs with masses in the range of $100 - 300 M_\odot$, see e.g. Alvarez et al. [2009]; Whalen and Fryer [2012], top evolutionary track in Fig 1.3. The second theory claims that $10^4 - 10^6 M_\odot$ seeds form directly from baryon collapse in dark matter halos e.g. Regan and Haehnelt [2009]; Shang et al. [2010]; Wise et al. [2008], see middle evolutionary track in Fig 1.3. The third competing argument presented in Djorgovski et al. [2008] supports the formation of $10^4 - 10^6 M_\odot$ SMBH seeds from the relativistic collapse of the first star clusters, see lower evolutionary track of BH seeds in Fig 1.3. Low frequency GW signatures from these seeds (or the lack thereof) will be a useful tool to distinguish between the aforementioned theories, e.g. Arun et al. [2009]; Sesana et al. [2004, 2007]; Volonteri [2010].

The current paradigm is that these massive black holes grow by accretion and

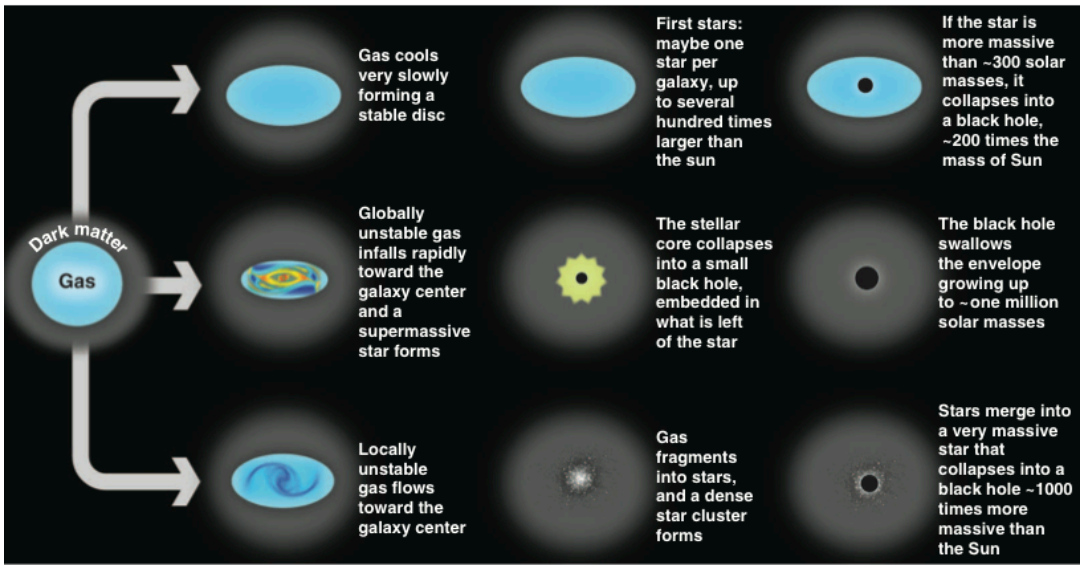

Figure 1.3: The three principal black hole seed theories, from Volonteri [2012].

mergers, e.g. King [2003]; Volonteri [2010, 2012] and references therein. Observations of distant active galactic nuclei, e.g. Haehnelt and Rees [1993], imply that SMBHs were also common in the past. If, as the current paradigm suggests, the SMBH host galaxy experiences many mergers during its lifetime, see e.g. Peebles [1982]; White and Rees [1978], then SMBHBs are the natural product of cosmic evolution.

Observational evidence for SMBHBs exists in the quasar OJ287: a 12 yr light structure arises from the SMBHB system where a secondary SMBHB, $m_2 = 1.4\times10^8 M_\odot$, perturbs the accretion disc of the primary SMBH, $m_1 = 1.8\times10^{10} M_\odot$ at regular intervals, causing increased emission in the jet, see Kidger et al. [1992]; Sillanpaa et al. [1988]; Valtonen et al. [2008, 2012]. Other observational signatures of SMBHB systems are outlined in e.g. Roedig et al. [2014].

The following calculations show that GWs emitted by SMBHBs during their coalescence history span a frequency range that extends from the nHz to μHz

regime, accessible via Pulsar Timing Array experiments.

Consider a pair of non-spinning, or Schwarzschild SMBHs. The maximum frequency of the GWs emitted by the binary is emitted at the innermost stable circular orbit (ISCO), at $f_{\rm max}$:

$$f_{\rm max} = \frac{1}{\pi 6^{3/2} M} \sim 4.4 \times 10^{-6} \left(\frac{M}{10^9\ M_\odot}\right)^{-1}\ {\rm Hz}, \tag{1.83}$$

A frequency of 10^{-6} Hz is $\sim$1/week– the high-frequency limit of PTAs. Assuming that a SMBHB is 10^6 yr from coalescence ($t_c = 0$), one can scale the GW frequency of the binary using Eq (1.72):

$$f_{\rm GW}(t) = 7.1 \times 10^{-8} \left(\frac{\mathcal{M}}{4.4 \times 10^8\ M_\odot}\right)^{-5/8} \left(\frac{t}{10^6\ {\rm yr}}\right)^{-3/8}\ {\rm Hz}\,. \tag{1.84}$$

Therefore, PTAs can access GWs generated by SMBHBs starting from 10^6 yrs before coalesce to ISCO, or equivalently, in the frequency range

$$7.1 \times 10^{-8} \left(\frac{\mathcal{M}}{4.4 \times 10^8\ M_\odot}\right)^{-5/8} \left(\frac{t}{10^6\ {\rm yr}}\right)^{-3/8} {\rm Hz} \leq f \leq 4.4 \times 10^{-6} \left(\frac{M}{10^9\ M_\odot}\right)^{-1} {\rm Hz}\,. \tag{1.85}$$

These binaries are at orbital separations r of

$$r(t) = 9.6 \times 10^{-3} \left(\frac{\mu}{2.5 \times 10^8\ M_\odot}\right)^{1/4} \left(\frac{M}{10^9\ M_\odot}\right)^{1/2} \left(\frac{t}{10^6\ {\rm yr}}\right)^{1/4} {\rm pc}\,, \tag{1.86}$$

cf. Eq (1.73), and have a GW strain magnitude, Eq (1.62) of

$$h \sim 5 \times 10^{-16} \left(\frac{\mathcal{M}}{10^9\ M_\odot}\right)^{5/3} \left(\frac{D_L}{1\ {\rm Gpc}}\right)^{-1} \left(\frac{f_{\rm GW}}{10^{-8}\ {\rm Hz}}\right)^{2/3} \tag{1.87}$$

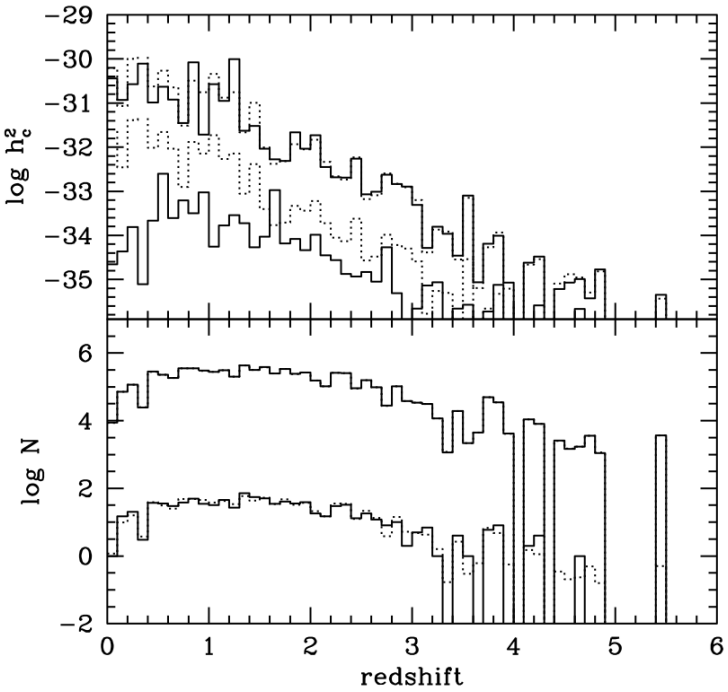

Figure 1.4: Contribution of different redshift intervals to the build-up of the GW signal at two different frequencies, $f = 8 \times 10^{-9}$ Hz and 10^{-7} Hz, computed using Monte Carlo sampling (solid lines) and a semi-analytical approach (dotted lines). In each panel, the upper histograms refer to $f = 8 \times 10^{-9}$ Hz and the lower histograms refer to $f = 10^{-7}$ Hz. Figure and caption reproduced from Sesana et al. [2008]'s Fig 4.

where $\mathcal{M}$ is the redshifted value of the chirp mass, $\mathcal{M} = \mathcal{M}(1 + z)$ at redshift z corresponding to the luminosity D_L distance of 1 Gpc.

Pulsar Timing Arrays can access GW in the nHz-μHz frequency band, and therefore it is clear that SMBHBs are are excellent GW source candidates.

1.4 The Stochastic Gravitational Wave Background from SMBHBs

The cosmic population of SMBHBs is expected to form a diffusive GW background, which may soon be detected by PTAs. To show that the background is truly stochastic, one can do a simple order of magnitude estimate for the number of sources N in a frequency interval $\Delta f = 1/T_{\rm obs}$, where $T_{\rm obs}$ is the total observation time of a PTA, typically 10 yrs. We wish to estimate

$$\Delta N = \frac{dN}{df}\Delta f = \frac{dN}{dt}\left(\frac{df}{dt}\right)^{-1}\Delta f\,, \tag{1.88}$$

and letting $f = f_{\rm GW}$, $\dot{f}_{\rm GW} \propto \mathcal{M}_c^{5/3} f_{\rm GW}^{11/3}$ by Eq (1.71). Therefore

$$\Delta N \propto \mathcal{M}_c^{-5/3} f_{\rm GW}^{-11/3} \Delta f \frac{dN}{dt}. \tag{1.89}$$

To roughly estimate dN/dt, one needs to estimate the number of galaxies in the Universe, $N_{\rm gal} \sim 10^{11}$, cf. Beckwith et al. [2006], the number of major mergers each galaxy undergoes, $N_{\rm merger}$ (order of a few, see e.g. Conselice et al. [2003]) and the age of the Universe, which is taken to be a Hubble time, H_0^{-1}. Using these ingredients, one may write down an order of magnitude estimate of dN/dt:

$$\frac{dN}{dt} \sim \frac{N_{\rm gal} \times N_{\rm merger}}{H_0} \tag{1.90}$$

$$\sim \frac{10^{11}\ \text{galaxies} \times 1\ \text{merger/galaxy}}{10^{10}\ \text{yr}} \tag{1.91}$$

$$\sim 10\ \text{mergers/yr}. \tag{1.92}$$

We can now write down an order of magnitude estimate of the number of sources ΔN in a frequency interval Δf:

$$\Delta N \sim 3.7 \times 10^{12} \left(\frac{\mathcal{M}_c}{10^9\ M_\odot}\right)^{-5/3} \left(\frac{f_{\rm GW}}{10^{-8}\ \rm Hz}\right)^{-11/3} \left(\frac{T_{\rm obs}}{10\ \rm yr}\right)^{-1} \left(\frac{dN/dt}{10\ \rm merg/yr}\right). \tag{1.93}$$

It is clear that $\Delta N \gg 1$. One may therefore safely assume that a stochastic GW background exists.

1.4.1 The characteristic strain

In stochastic GW background searches, the amplitude of the GW background is usually given in terms of a characteristic strain, $h_c = A(f_{\rm GW}/1yr^{-1})^\alpha$, where $\alpha = -2/3$ for SMBHBs. In this section, the reason for the $\alpha = -2/3$ scaling relation will be made clear via arguments presented in Phinney [2001]. In other words, Phinney's theorem implies that the energy density in GWs per log frequency interval is equal to the product of the comoving number density of event remnants and the redshifted energy that each event produced, per log frequency interval.

Let f_r be the GW frequency in the source's rest frame such that $f_r = f_{\rm GW}(1+z)$, for some redshift z and frequency $f_{\rm GW}$ observed at the Earth. The total energy emitted in GWs between frequencies f_r and $f_r + df_r$ is

$$\frac{dE_{gw}}{df_r} df_r. \tag{1.94}$$

Next, let $N(z)dz$ be the number of events per unit of comoving volume occurring between redshift z and $z+dz$. Define $\Omega_{gw}(f)$ to be the present day GW energy density per logarithmic frequency interval f, divided by the critical energy density

$\rho_c = 3H_0^2/(8\pi)$ needed to close the Universe, i.e.

$$\Omega_{gw}(f) \equiv \frac{1}{\rho_c}\frac{d\rho_{gw}(f)}{d\ln f}, \tag{1.95}$$

where ρ_{gw} is the GW energy density. The total present day energy in GWs is therefore:

$$\varepsilon_{gw} \equiv \int_0^\infty \rho_c \Omega_{gw}(f) d\ln f \equiv \int_0^\infty \frac{\pi}{4} f^2 h_c^2(f)\frac{df}{f}, \tag{1.96}$$

where h_c is the characteristic amplitude of the GW spectrum over a logarithmic frequency interval. Note that h_c is related to the 1-sided ($0 < f < \infty$) spectral density $S_{h,1}$ of the GW background by $h_c^2(f) = fS_{h,1}$. The present day energy density ε_{gw} must be equal to the sum of the energy densities radiated at each redshift, divided by a factor of $(1+z)$ to account for gravitational redshifting since the time of emission. We can therefore write the ε_{gw} as:

$$\varepsilon_{gw} = \int_0^\infty \int_0^\infty N(z)\frac{1}{1+z}\frac{dE}{df_r} f_r \frac{df_r}{f_r} dz. \tag{1.97}$$

Since $f_r = f(1+z)$, one can write $df_r/f_r = df/f$ and simplify:

$$\varepsilon_{gw} = \int_0^\infty \int_0^\infty N(z)\frac{1}{1+z} f_r \frac{dE}{df_r}\frac{df}{f} dz. \tag{1.98}$$

Equating Eqs (1.96) and (1.98) one can write down Phinney [2001]'s main theorem:

$$\rho_c \Omega_{gw}(f) = \frac{\pi}{4} f^2 h_c^2(f) = \int_0^\infty N(z)\frac{1}{1+z}\left(f_r \frac{dE_{gw}}{df_r}\right) dz. \tag{1.99}$$

This is the main result, which implies that the energy density in GWs per log frequency interval is equal to the product of the comoving number density of event

remnants and the redshifted energy that each event produced, per log frequency interval. For the purposes of PTAs, we are interested in how this result can help us to estimate the magnitude of the characteristic strain of the stochastic GW background, $h_c(f)$, generated by the incoherent superposition of SMBHBs.

In the following paragraphs, the amplitude A of the characteristic strain is estimated at a reference frequency of $1/\mathrm{yr}^{-1}$: $h_c(f) = A(f/1\ \mathrm{yr}^{-1})^{-2/3}$.

In the Newtonian limit, let us consider a circular binary with chirp mass $\mathcal{M}$, Eq (1.8). Such a binary, which merges due to GW emission in less than a Hubble time, has

$$\begin{aligned} \frac{dE_{gw}}{df_r} &= \frac{dE}{dt}\left(\frac{df_r}{dt}\right)^{-1} \\ &= \frac{\pi}{3}\frac{\mathcal{M}^{5/3}}{(\pi f_r)^{1/3}}\,, \end{aligned} \tag{1.100}$$

using Eqs (1.65) and (1.71), and assuming that the binary's separation is small enough that it merges within a Hubble time. Substituting Eq (1.100) into Eq (1.98) gives the scaling relations for Ω_{gw} and the characteristic strain h_c. Firstly,

$$\Omega_{gw}(f) = \frac{1}{\rho_c}\int_0^\infty N(z)\frac{1}{1+z}\left[f_r\frac{\pi}{3}\frac{\mathcal{M}^{5/3}}{(\pi f_r)^{1/3}}\right]dz\,, \tag{1.101}$$

$$= \frac{8\pi^{5/3}}{9H_0^2}f^{2/3}\mathcal{M}^{5/3}\int_0^\infty N(z)\frac{1}{(1+z)^{1/3}}dz\,. \tag{1.102}$$

Let $N_0 = \int_0^\infty N(z)dz$ be the present-day comoving number density of merged remnants and

$$\left\langle (1+z)^{1/3}\right\rangle = \frac{1}{N_0}\int_{z_{\min}}^{z_{\max}}\frac{N(z)}{(1+z)^{1/3}}dz\,. \tag{1.103}$$

Eq (1.102) can therefore be rewritten as

$$\Omega_{gw}(f) = \frac{8\pi^{5/3}}{9H_0^2} f^{2/3} \mathcal{M}^{5/3} N_0 \left\langle (1+z)^{1/3} \right\rangle . \tag{1.104}$$

Similarly, from Eq (1.99) one can derive an expression for the characteristic strain $h_c(f)$:

$$h_c^2(f) = \frac{4}{\pi} \frac{1}{f^2} N_0 \left\langle (1+z)^{1/3} \right\rangle \frac{\pi}{3} f \frac{\mathcal{M}^{5/3}}{(\pi f)^{1/3}} \tag{1.105}$$

$$= \frac{4}{3} \pi^{-1/3} f^{-4/3} \mathcal{M}^{5/3} N_0 \left\langle (1+z)^{1/3} \right\rangle , \tag{1.106}$$

and therefore $h_c \propto f^{-2/3}$. To estimate the amplitude of the characteristic strain, we require estimates of the black hole chirp mass $\mathcal{M}$, the comoving number density of merged remnants N_0 and $\left\langle (1+z)^{1/3} \right\rangle$. Phinney [2001] shows that in a flat Universe, one can expect $\left\langle (1+z)^{1/3} \right\rangle = 0.74$, and that this estimate is not very sensitive to the cosmology chosen. According to simulations carried out in Rajagopal and Romani [1995], $N_0 = 10^{-4}$ Mpc^{-3}. The characteristic strain can therefore be written as a function of frequency using the aforementioned typical values for N_0, $\left\langle (1+z)^{1/3} \right\rangle$. For a SMBHB with $m_1 = m_2 = 10^9 M_\odot$, and find that the strain scales as

$$h_c(f) \sim 2 \times 10^{-16} (f/1\mathrm{yr}^{-1})^{-2/3} . \tag{1.107}$$

Indeed, when setting a limit on the stochastic GW background, one identifies the value of the amplitude A of the GW background reported at a reference frequency at $1/\mathrm{yr}^{-1}$: $h_c(f) = A(f/1\mathrm{yr}^{-1})^{-2/3}$, see Fig 1.5. The best current limit on the amplitude A of the characteristic strain of the stochastic isotropic GW background from SMBHBs is from Shannon et al. [2013], who report a value

of $A < 2.4 \times 10^{-15}$, at 95% confidence. Other more speculative stochastic GW background sources, such as cosmic strings and relic GWs, have different values of α. For cosmic strings $\alpha = -7/6$ and for relic GWs $-1 \leq \alpha \leq -0.8$, see Grishchuk [1975]; Maggiore [2000]. Limits on the amplitude of these GW background are found in e.g. Jenet et al. [2006]; Sanidas et al. [2012]; van Haasteren et al. [2011].

1.5 Pulsar Timing Arrays as Gravitational Wave Detectors

The detection of GWs is one of the key scientific goals of Pulsar Timing Arrays (PTAs). A PTA uses a network of radio telescopes to regularly monitor stable millisecond pulsars, constituting a galactic-scale GW detector, cf. Ferdman et al. [2010]; Hobbs et al. [2010]; Jenet et al. [2009]; Verbiest et al. [2010]. Gravitational radiation affects the propagation of radio pulses between a pulsar and a telescope at the Earth. The difference between the expected and actual time-of-arrival (TOA) of the pulses – the so-called timing residuals – carries information about the GWs, cf. Detweiler [1979]; Estabrook and Wahlquist [1975]; Sazhin [1978], which can be extracted by correlating the residuals from different pulsar pairs.

1.5.1 Neutron Stars and Pulsars

Neutron stars were first theorized by Baade and Zwicky [1934a,b], almost immediately after the discovery of the neutron by Chadwick [1932]. Detailed calculations of their structure were performed soon thereafter, see e.g. Oppenheimer and Volkoff [1939], however, neutron stars were not actually discovered until 1967,

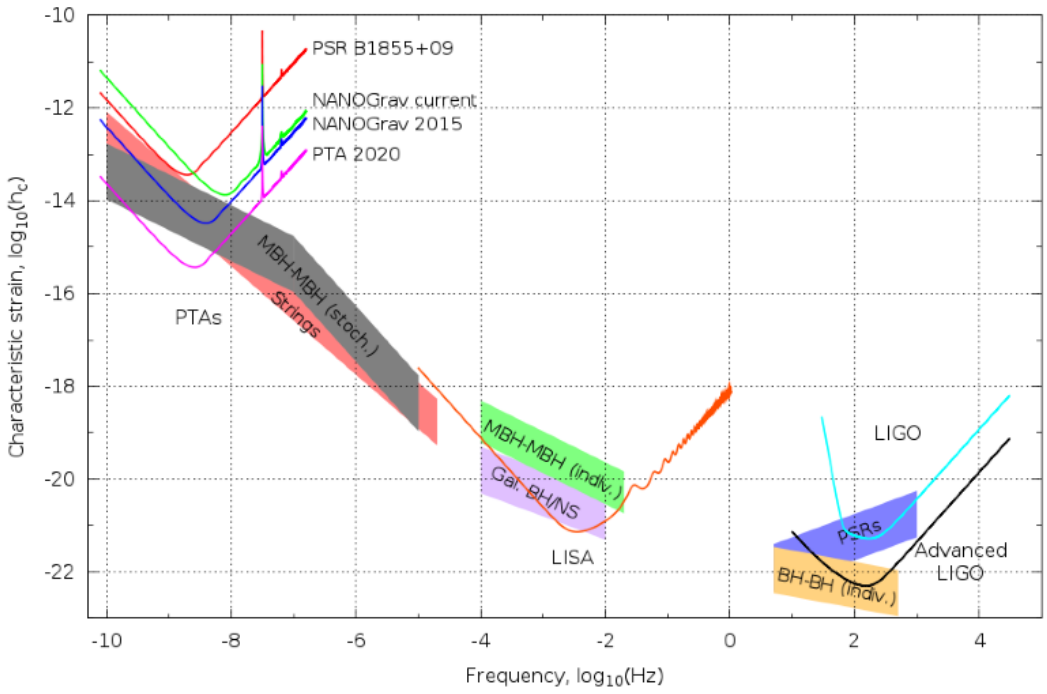

Figure 1.5: The GW strain spectrum from PTAs in the nHz band to ground-based laser interferometers in the kHz band. Note the lack of sensitivity in the PTA band to frequencies of 1/yr– this is due to solar system ephemeris errors. Pulsar TOA fitting processes remove low-frequency information, making PTAs less sensitive to the lower frequency limit of the PTA band. Image reproduced from Demorest et al. [2009].

when S. J. Bell[1], under the supervision of A. Hewish, discovered the first evidence for pulsars, reported in Hewish et al. [1968]. This would earn Hewish and Ryle the Nobel Prize for Physics in 1974, see Nobelprize.org [1974] for details.

Pulsars are neutron stars with their spin axis misaligned with their magnetic field axis, Fig 1.6. They have been used to provide the most stringent tests of General Relativity and alternative theories of gravity (e.g. Kramer et al. [2006]; Lyne et al. [2004b] and references therein) and have provided stringent evidence that GW exist– e.g. Taylor and Weisberg [1982]; Kramer and Wex [2009]. Pulsars

[1]now Dame (Susan) Jocelyn Bell Burnell, DBE, FRS, FRAS

can be characterized by their period P and spin-down rate, or period derivative, $\dot{P}$. According to Lorimer and Kramer [2012] and references therein, the general pulsar population has a typical period and spin-down rate of $P \sim 0.5$ s and $\dot{P} \sim 10^{-15}$ ss^{-1}. With these two quantities one can define the characteristic age of a pulsar, $\tau = P/(2\dot{P})$, which for the above typical values yields a characteristic age of $\sim 10^7$ yr, and a typical magnetic field strength $B \propto \sqrt{P\dot{P}} \sim 10^{12}$ G.

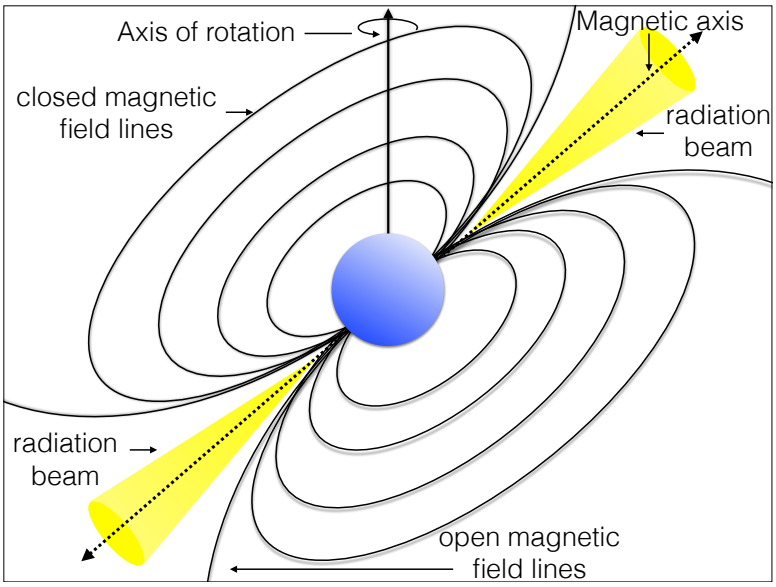

Figure 1.6: A rotating neutron star with its spin axis misaligned with its magnetic field axis, called a pulsar. Electromagnetic radiation centred on the magnetic field axis is produced above the surface of the pulsar. Due to the misalignment of the magnetic and rotational axes, pulsars are often referred to as cosmic lighthouses, since the received light appears to pulse as the beam crosses our line of sight.

Of particular interest to this body of work are millisecond pulsars (MSPs)– pulsars with $P \sim 3$ ms and $\dot{P} \sim 10^{-20}$ ss^{-1}, first discovered by Backer et al. [1982]. MSPs are "old pulsars" with weaker magnetic fields, here $\tau \sim 10^9$ yr and $B \sim 10^8$ G, which were spun-up by mass transfer up by a companion, such as a white dwarf or a main sequence star. In fact, 80% of all MSPs are found in

binary systems. Weaker magnetic fields cause less glitches, and therefore MSPs tend to be the most stable timers of all pulsars.

Each radio pulse received form a pulsar has its own profile. In order to get a typical signal, one needs to integrate over a certain time which may vary from pulsar to pulsar. The integration process is a coherent addition of many pulses which becomes very stable over time with small TOA errors. The Hulse-Taylor pulsar PSR 1916+13, for example, can be profiled for 5 mins and the resulting TOA error is 20μs or less.

Stable TOAs, and hence small timing residuals, are important for detecting GWs, since the strain PTA are sensitive to goes as the timing residual Δt over the observation time $T_{\rm obs}$,

$$h \sim \frac{\Delta t}{T_{\rm obs}} \,. \tag{1.108}$$

The characteristic strain of the GW background from SMBHBs has been estimated to be $h_c \sim 10^{-15}$, therefore to detect the stochastic background, one would require pulsars with residuals of the order

$$\Delta t \sim 3.2 \times 10^{-7} \left(\frac{h_c}{10^{-15}}\right) \left(\frac{T_{\rm obs}}{10 \text{ yr}}\right) \text{ s} \,, \tag{1.109}$$

or roughly 300 ns.

The MSP TOAs are typically transformed to the solar system barycentre (SSB), described in detail in Sec 1.5.2, as to be in an inertial reference frame with the pulsar. To accurately model a TOA, one needs to take into account various time delays in the radio pulse: the Roemer delay, Shapiro delay, Einstein

delay, the interaction with the interstellar medium (ISM), and even the rotation of the Earth on its axis induces daily modulations of $R_\oplus/c \sim 21$ ms. These effects are now briefly described– more details can be found in e.g. Maggiore [2007].

The Roemer delay of a pulse, denoted $\Delta_{R,\odot}$, is caused by the position of the Earth in the Solar System: if the Earth is in the direction of the pulsar, the pulse arrives early by a factor of t_0. If the Earth is on the opposite side of its orbit, then the pulse signal arrives later by a factor of t_0 with respect to the Sun.

The Einstein delay $\Delta_{E,\odot}$ accounts for the time dilation from the moving pulsar and the gravitational redshift caused by solar system objects, such as the sun and the planets. This delay could also arise due to the presence of a binary companion, since most MSPs are in binary systems.

The Shapiro delay $\Delta_{S,\odot}$ is the extra time required by the pulses to travel through the curved space-time containing massive objects such as the sun, planets and/or the MSP's companion, see e.g. NRAO [2014]. For example, a pulse grazing the surface of the sun would have a Shapiro delay of $\Delta_{S,\odot} \approx 120\mu$s, three orders of magnitude larger than the residual required, cf. Eq (1.109).

The final time delay to be considered here is due to the ISM. The ISM is primarily composed of gases and dust, thus having an effective refractive index which changes the frequency of the radio pulses coming from the pulsar. A radio pulse with frequency ν travels with a group velocity v_g:

$$v_g \simeq c\left(1 - \frac{n_e e^2}{2\pi m_e \nu^2}\right), \tag{1.110}$$

where n_e is the electron number density, m_e is the electron mass and e is the electron charge, e.g. Maggiore [2007]; NRAO [2014]. Therefore, the travel time

over a distance L would be

$$\int_0^L \frac{dl}{v_g} \simeq \frac{L}{c} + \left(\frac{e^2}{2\pi m_e c}\right) \int_0^L n_e dl. \tag{1.111}$$

From Eq (1.111) a quantity called the Dispersion Measure (DM) is defined, cf. e.g. Lorimer and Kramer [2012], where DM $\equiv \int_0^L n_e dl$. As the DM is not known a priori, it becomes one of the dimensions of the parameter space in which we perform data analysis of the signal, cf. e.g. van Haasteren et al. [2011]. This is the final correction missing from the general formula to find the time of arrival of a pulse at the SSB, t_{SSB}. By defining

$$t_{SSB} = \tau_{obs} - \frac{\mathrm{D}}{\nu^2} + \Delta_{E,\odot} + \Delta_{R,\odot} - \Delta_{S,\odot}, \tag{1.112}$$

where $\mathrm{D} = e^2/(2\pi m_e c)\mathrm{DM}$, we have established a coordinate time at which the signal recorded by our laboratory clock on Earth at τ_{obs} would have arrived if the absence of the gravitational potential of the solar system and the interaction with the ISM. Now the time delay depends only on the properties of the source. Indeed, most pulsar suffer from "timing noise", described in e.g. Perrodin et al. [2013], which limits the accuracy of their root-mean-square timing residuals.

The 300 ns accuracy, see Eq (1.109), is currently achievable in only a few MSPs, such as J0437−4715– see e.g. Lorimer [2008]; Verbiest et al. [2008], which is the best known timer.

1.5.2 PTA response to Gravitational Waves

GWs perturb the null geodesics of the radio waves travelling from the pulsar to the Earth, so changes in the TOAs could signal the presence of a GW. Let us consider a source emitting gravitational radiation in the PTA regime and consider a GW metric perturbation $h_{\mu\nu}(t)$ in the transverse and traceless (TT) gauge, see Sec 1.1.3 for details. Recall that $i, j = x, y, z$ are the spatial indices.

Information about the source is encoded in 2 independent polarization amplitudes: $h_+(t)$ and $h_\times(t)$. We write

$$h_{ij}(t, \hat{\Omega}) = e^+_{ij}(\hat{\Omega}) h_+(t, \hat{\Omega}) + e^\times_{ij}(\hat{\Omega})\, h_\times(t, \hat{\Omega})\,, \tag{1.113a}$$

$$h_{ij}(f, \hat{\Omega}) = e^+_{ij}(\hat{\Omega}) h_+(f, \hat{\Omega}) + e^\times_{ij}(\hat{\Omega})\, h_\times(f, \hat{\Omega}). \tag{1.113b}$$

The polarization tensors $e^A_{ij}(\hat{\Omega})$ are uniquely defined once one specifies the wave principal axes described by the unit vectors $\hat{m}$ and $\hat{n}$:

$$e^+_{ij}(\hat{\Omega}) = \hat{m}_i \hat{m}_j - \hat{n}_i \hat{n}_j\,, \tag{1.114a}$$

$$e^\times_{ij}(\hat{\Omega}) = \hat{m}_i \hat{n}_j + \hat{n}_i \hat{m}_j\,. \tag{1.114b}$$

Following the steps outlined in Anholm et al. [2009]; Detweiler [1979] but giving more detail, we will now derive the 2-pulse response function of a PTA to a GW. Starting with a metric perturbation in the $\hat{\Omega} = \hat{z}$ direction described by $h_{\mu\nu}(t, \hat{\Omega} = \hat{z})$, which will be referred to as $h_{\mu\nu}(t - z)$ from here on, we can look

at the background described by

$$g_{\mu\nu} = \eta_{\mu\nu} + h_{\mu\nu}(t-z) \tag{1.115}$$

$$= \begin{pmatrix} -1 & 0 & 0 & 0 \\ 0 & 1 & 0 & 0 \\ 0 & 0 & 1 & 0 \\ 0 & 0 & 0 & 1 \end{pmatrix} + \begin{pmatrix} 0 & 0 & 0 & 0 \\ 0 & h_+ & h_\times & 0 \\ 0 & h_\times & -h_+ & 0 \\ 0 & 0 & 0 & 0 \end{pmatrix}. \tag{1.116}$$

We then consider a null vector, s^μ, in Minkowski space-time, then in perturbed space-time so that $s^\mu \to \sigma^\mu$ according to

$$\sigma^\mu = s^\mu - \frac{1}{2}\eta^{\mu\nu}h_{\mu\nu}s^\upsilon, \tag{1.117}$$

which is obtained from the linearized equations of motion in a TT gauge. The null vector in Minkowksi space-time that points from the pulsar to the solar system barycentre is

$$s^\mu = \nu(1, -\alpha, -\beta, -\gamma), \tag{1.118}$$

where α, β, γ are the direction cosines of x, y, z, respectively. The corresponding perturbed vector, σ^μ, is calculated from Eq (1.117). The first 2 components are calculated explicitly as an example. Using Eq (1.117) one can find:

$$\sigma^t = s^t - \frac{1}{2}\eta^{t\nu}h_{\nu\upsilon}s^\upsilon, \tag{1.119}$$

but from Eq (1.115) it is clear that only η^{tt} gives a non-zero value, so we write

$$\sigma^t = s^t - \frac{1}{2}\eta^{tt}h_{t\upsilon}s^\upsilon = 1, \tag{1.120}$$

since the first row of the $h_{\mu\nu}$ matrix is all zero. Therefore $\sigma^t = \nu$. It is less trivial to calculate σ^x:

$$\begin{aligned}
\sigma^x &= s^x - \frac{1}{2}\eta^{x\nu}h_{\nu\upsilon}s^\upsilon && (1.121)\\
&= -\alpha - \frac{1}{2}(\eta^{xt}h_{t\upsilon}s^\upsilon + \eta^{xx}h_{x\upsilon}s^\upsilon + \dots) && (1.122)\\
&= -\alpha - \frac{1}{2}(0 - \alpha h_+ - \beta h_\times) && (1.123)\\
&= -\alpha\left(1 - \frac{1}{2}h_+\right) + \frac{\beta}{2}h_\times. && (1.124)
\end{aligned}$$

The other components are calculated similarly and the final vector is

$$\sigma^\mu = \nu \begin{pmatrix} 1 \\ -\alpha\left(1 - \frac{1}{2}h_+\right) + \frac{\beta}{2}h_\times \\ -\alpha\left(1 + \frac{1}{2}h_+\right) + \frac{\alpha}{2}h_\times \\ -\gamma \end{pmatrix}. \quad (1.125)$$

Radio pulses from the pulsars follow geodesics through space-time. The geodesic equation, cf. e.g. Maggiore [2007], with affine parameter λ tells us that

$$\frac{d\sigma^t}{d\lambda} = -\Gamma^t_{\mu\nu}\sigma^\mu\sigma^\nu, \quad (1.126)$$

where

$$\Gamma^t_{\mu\nu} = -\frac{1}{2}g^{t\upsilon}\left(\frac{\partial g_{\nu\upsilon}}{\partial x^\mu} + \frac{\partial g_{\mu\upsilon}}{\partial x^\nu} - \frac{\partial g_{\mu\nu}}{\partial x^\upsilon}\right). \quad (1.127)$$

Letting the indices vary, the only non-vanishing term is

$$-\frac{1}{2}g^{tt}\left(-\frac{\partial g_{\mu\nu}}{\partial x^t}\right) = \frac{1}{2}\dot{g}_{\mu\nu}, \quad (1.128)$$

and so

$$\Gamma^t_{\mu\nu} = \frac{1}{2}\begin{pmatrix} 0 & 0 & 0 & 0 \\ 0 & \dot{h}_+ & \dot{h}_\times & 0 \\ 0 & \dot{h}_\times & -\dot{h}_+ & 0 \\ 0 & 0 & 0 & 0 \end{pmatrix}. \tag{1.129}$$

The geodesics can then be written in terms of the spatial indices only, i, j:

$$\frac{d\sigma^t}{d\lambda} = -\frac{1}{2}\dot{g}_{ij}\sigma^i\sigma^j \tag{1.130}$$

$$= -\frac{1}{2}\left[\dot{g}_{xx}\sigma^x\sigma^x + 2\dot{g}_{xy}\sigma^x\sigma^y + \dot{g}_{yy}\sigma^y\sigma^y\right] \tag{1.131}$$

$$= -\frac{1}{2}\left[\dot{g}_{xx}(\sigma^x)^2 + \dot{g}_{yy}(\sigma^y)^2\right] - \dot{g}_{xy}\sigma^x\sigma^y, \tag{1.132}$$

and g_{xx}, g_{xy}, g_{yy} and their derivatives can be computed from Eq (1.115), yielding

$$-\frac{\dot{h}_+}{2}\left[(\sigma^x)^2 - (\sigma^y)^2\right] - \frac{1}{2}\dot{h}_\times\sigma^x\sigma^y. \tag{1.133}$$

Using Eq (1.125) we can substitute the values of σ^i :

$$(\sigma^x)^2 - (\sigma^y)^2 = \left[-\alpha\left(1 - \frac{1}{2}h_+\right)^2 + \frac{1}{2}\beta h_\times\right]^2 - (\sigma^y)^2, \tag{1.134}$$

and after some algebra and to leading order in h:

$$(\sigma^x)^2 - (\sigma^y)^2 = \nu^2(\alpha^2 - \beta^2) + \mathcal{O}(h) \quad \text{and} \quad \sigma^x\sigma^y = \nu^2\alpha\beta + \mathcal{O}(h). \tag{1.135}$$

Since $\sigma^t = \nu$ from Eq (1.125), the following is obtained by Eqs (1.126), (1.133):

$$\frac{d\nu}{d\lambda} = -\frac{1}{2}\dot{h}_+\nu^2(\alpha^2 - \beta^2) - \dot{h}_\times\nu^2\alpha\beta. \tag{1.136}$$

Recall that $h_A = h_A(t-z)$, where $A = +, \times$ and $\nu = dt/d\lambda$, $\partial h_A/\partial z = -\partial h_A/\partial t$ and $dz/d\lambda = -\nu\gamma$. Now write the time derivatives as derivatives with respect to λ:

$$\frac{dh}{d\lambda} = \frac{\partial h_A}{\partial t}\frac{dt}{d\lambda} + \frac{\partial h_A}{\partial z}\frac{dz}{d\lambda}. \tag{1.137}$$

Making the above substitutions gives us an expression for dh_A/dt:

$$\frac{dh_A}{d\lambda} = \left(\frac{\partial h_A}{\partial t}\right)\nu + \frac{\partial h_A}{\partial t}(-\nu\gamma) \tag{1.138}$$

$$\dot{h}_A = \frac{dh_A}{d\lambda}\frac{1}{\nu(1+\gamma)}. \tag{1.139}$$

Substituting Eq(1.139) back into Eq(1.136) and simplifying:

$$-\frac{1}{\nu}\frac{d\nu}{d\lambda} = \frac{dh_+}{d\lambda}\frac{(\alpha^2-\beta^2)}{1+\gamma} + \frac{dh_\times}{d\lambda}\frac{\alpha\beta}{1+\gamma}. \tag{1.140}$$

Let us define $\Delta h_A = h_A^p - h_A^e$. This can be thought of as the difference between the metric perturbation at the pulsar, called the "pulsar term" with space-time coordinates $(t_p, \vec{x}_p)$, and the receiver has space-time coordinates $(t, \vec{x})$. Integrating the above equation and expanding to first order in Δh_A:

$$\frac{\nu(t)}{\nu_0} \simeq 1 - \frac{1}{2}\frac{(\alpha^2-\beta^2)}{1+\gamma}\Delta h_+ - \frac{\alpha\beta}{1+\gamma}\Delta h_\times. \tag{1.141}$$

Therefore, for an observer at the SSB, the frequency is shifted according to the 2-pulse function

$$z(t,\hat{\Omega}) \equiv \frac{\nu(t)-\nu_0}{\nu_0} = \frac{1}{2}\frac{(\alpha^2-\beta^2)}{1+\gamma}\Delta h_+ + \frac{\alpha\beta}{1+\gamma}\Delta h_\times, \tag{1.142}$$

where $\nu(t)$ is the received frequency at the SSB.

1.5.3 Timing Residuals from a Stochastic GW Background

We will now briefly examine what happens when we combine the contributions from GWs in N different directions, $\hat{\Omega}_n$. As before, we consider a metric perturbation, $h_{\mu\nu}$ in a TT gauge which is the sum of $h^n_{\mu\nu}$ metric perturbations. Explicitly we can write

$$h_{\mu\nu} = \sum_n^N h^n_{\mu\nu}(t - \hat{\Omega}_n \cdot \vec{x}), \tag{1.143}$$

where t and $\vec{x}$ form x^μ: a 4-vector in a Minkowski background. As before, let us define a null vector in Minkowski space, $s^\mu = dx^\mu/d\lambda = \nu(1, -\alpha, -\beta, -\gamma)$ which we will now call $\nu(1, -\hat{p})$. The null geodesic perturbed by $h_{\mu\nu}$ is described by $\sigma^\mu = s^\mu + \delta s^\mu$. We are again interested in describing the geodesics defined in Eq (1.127), which result in $\Gamma^t_{\mu\nu} = \frac{1}{2}\dot{g}_{\mu\nu} = \frac{1}{2}\dot{h}_{\mu\nu}$. Therefore

$$\begin{aligned}
\frac{d\sigma^t}{d\lambda} &= -\frac{1}{2}\dot{h}_{\mu\nu}\sigma^\mu\sigma^\mu && (1.144)\\
&= -\frac{1}{2}\dot{h}_{\mu\nu}(s^\mu + \delta s^\mu)(s^\nu + \delta s^\nu) && (1.145)\\
&= -\frac{1}{2}\dot{h}_{\mu\nu}s^\mu s^\nu, && (1.146)
\end{aligned}$$

and since $s^\mu = \nu(1, -\hat{p})$ we can simplify the above expression to

$$\frac{d\sigma^t}{d\lambda} = -\frac{1}{2}\dot{h}_{ij}\nu^2\hat{p}^i\hat{p}^j\,, \tag{1.147}$$

where i, j are spatial indices. We now wish to write the right-hand side of Eq(1.147) in terms of $d\lambda$, which can be done by using Eq (1.137):

$$\begin{aligned}\frac{dh^n_{\mu\nu}(t-\hat{\Omega}_n\cdot\vec{x})}{d\lambda} &= \frac{\partial h^n_{\mu\nu}(t-\hat{\Omega}_n\cdot\vec{x})}{\partial t}\frac{dt}{d\lambda}+\frac{\partial h^n_{\mu\nu}(t-\hat{\Omega}_n\cdot\vec{x})}{\partial(\hat{\Omega}_n\cdot\vec{x})}\frac{d(\hat{\Omega}_n\cdot\vec{x})}{d\lambda}\\ &= \frac{\partial h^n_{\mu\nu}(t-\hat{\Omega}_n\cdot\vec{x})}{\partial t}\nu-\frac{\partial h^n_{\mu\nu}(t-\hat{\Omega}_n\cdot\vec{x})}{\partial t}\frac{d\vec{x}}{d\lambda}\hat{\Omega}_n\\ &= \frac{\partial h^n_{\mu\nu}(t-\hat{\Omega}_n\cdot\vec{x})}{\partial t}\left(\nu-\hat{\Omega}_n\frac{d\vec{x}}{d\lambda}\right). \end{aligned} \tag{1.148}$$

Recall however that $d\vec{x}/d\lambda = \nu\cdot(-\hat{p})$, and therefore the full expression can then be written as

$$\frac{dh^n_{\mu\nu}(t-\hat{\Omega}_n\cdot\vec{x})}{d\lambda} = \frac{\partial h^n_{ij}(t-\hat{\Omega}_n\cdot\vec{x})\nu(1+\hat{\Omega}_n\cdot\hat{p})}{\partial t}. \tag{1.149}$$

Substituting Eq (1.149) into Eq (1.147) gives an expression with derivatives in terms of λ, and for simplicity, we write $h^n_{ij}(t-\hat{\Omega}_n\cdot\vec{x}) = h^n_{ij}(t,\hat{\Omega}_n)$:

$$\frac{d\sigma^t}{d\lambda} = -\frac{1}{2}\left[\frac{dh^n_{ij}(t,\hat{\Omega}_n)}{d\lambda}\frac{1}{\nu(1+\hat{\Omega}_n\cdot\hat{p})}\right]\nu^2\hat{p}^i\hat{p}^j \tag{1.150}$$

$$\frac{1}{\nu}\frac{d\nu}{d\lambda} = -\frac{1}{2}\frac{dh^n_{ij}(t,\hat{\Omega}_n)}{d\lambda}\frac{\hat{p}^i\hat{p}^j}{1+\hat{\Omega}_n\cdot\hat{p}}, \tag{1.151}$$

which can be readily integrated to yield

$$z(t,\hat{\Omega}) \equiv \frac{\nu(t)-\nu_0}{\nu_0} = \sum_n^N \frac{1}{2}\frac{\hat{p}^i\hat{p}^j}{1+\hat{\Omega}_n\cdot\hat{p}}\Delta h^n_{ij}(t,\hat{\Omega}_n) \tag{1.152}$$

where

$$\Delta h_{ij}(t,\hat{\Omega}) \equiv h_{ij}(t,\hat{\Omega}) - h_{ij}(t_{\rm p},\hat{\Omega}) \tag{1.153}$$

is the difference between the metric perturbation at the Earth $h_{ij}(t,\hat{\Omega})$, the so-called *Earth term*, with coordinates $(t,\vec{x})$, and at the pulsar $h_{ij}(t_{\rm p},\hat{\Omega})$, the so-called *pulsar term*, with coordinates $(t_{\rm p},\vec{x}_p)$.[1] The fractional frequency shift over the entire sky (for a stochastic GW background) is obtained by integrating Eq (1.152) is:

$$z(t) = \int d\hat{\Omega} z(t,\hat{\Omega}). \tag{1.154}$$

and the observable quantity in PTAs in the timing residual, obtained from integrating the fractional frequency shift:

$$r(t) = \int^t dt' z(t'). \tag{1.155}$$

The timing residuals are then cross-correlated to search for stochastic GW background signals. This is procedure is outlined in the following section.

1.6 The Overlap Reduction Function

Let us consider a plane wave expansion for the metric perturbation $h_{ij}(t,\vec{x})$ produced by a stochastic background:

$$h_{ij}(t,\vec{x}) = \sum_A \int_{-\infty}^{\infty} df \int_{S^2} d\hat{\Omega}\; h_A(f,\hat{\Omega})\; e^{i2\pi f(t-\hat{\Omega}\cdot\vec{x})}\; e^A_{ij}(\hat{\Omega})\;, \tag{1.156}$$

[1] Note that the equivalent expression in Anholm et al. [2009], Eq. (9), has a sign error, as acknowledged by the authors, see the discussion of Eq (29) in e.g. Book and Flanagan [2011].

where f is the frequency of the GWs, the index $A = +, \times$ labels the two independent polarizations, the spatial indices are $i, j = 1, 2, 3$, the integral is on the two-sphere S^2, and our sign convention for the Fourier transform $\tilde{g}(f)$ of a generic function $g(t)$ follows the GW literature convention

$$\tilde{g}(f) = \int_{-\infty}^{+\infty} dt\, g(t)\, e^{-i2\pi ft}\,. \tag{1.157}$$

The unit vector $\hat{\Omega}$ identifies the propagation direction of a single gravitational wave plane, that can be decomposed over the GW polarization tensors $e_{ij}^{A}(\hat{\Omega})$ and the two independent polarization amplitudes, see Eqs (1.113a), (1.113b), (1.114a), (1.114b). For a stationary, Gaussian and unpolarized background the polarization amplitudes satisfy the following statistical properties:

$$\langle h_A^*(f, \hat{\Omega}) h_{A'}(f', \hat{\Omega}') \rangle = \delta^2(\hat{\Omega}, \hat{\Omega}') \delta_{AA'} \delta(f - f') H(f) P(\hat{\Omega})\,, \tag{1.158}$$

where $\langle\, \cdot \,\rangle$ is the expectation value and $\delta^2(\hat{\Omega}, \hat{\Omega}') = \delta(\cos\theta - \cos\theta')\delta(\phi - \phi')$ is the covariant Dirac delta function on the two-sphere, cf. Finn et al. [2009]. This condition implies that the radiation from different directions are statistically independent. Moreover, we have factorized the power spectrum such that $P(f, \hat{\Omega}) = H(f)P(\hat{\Omega})$, where the function $H(f)$ describes the spectral content of the radiation, and $P(\hat{\Omega})$ describes the angular distribution of the GW energy density on the sky. For now we assume that this is isotropic.

The search for a stochastic GW background contribution in PTA data relies on looking for correlations induced by GWs in the residuals from different pulsars. These correlations in turn depend on the spectrum $H(f)$ of the radiation,

cf. Eqs (1.158), and the antenna beam pattern convolved with the angular distribution $P(\hat{\Omega})$ of the GW energy density in the sky, which is described below. For now, we consider $P(\hat{\Omega}) = 1$, the isotropic case, however a more general treatment is given in Chapter 2.

The cross-correlated timing residuals enter into the likelihood function through the evaluation of the overlap reduction function (ORF)– a dimensionless function which quantifies the response of the pulsar pairs to the stochastic GW background. The ORF is in turn a function of the frequency of the GW background, the distance to each pulsar, and the angular separation of each pulsar pair and is usually normalized such that pulsar pairs with zero angular separation have a maximal detector response of 1 for an isotropic distribution of GW energy density.

To write down the ORF, we consider a frame in which

$$t_p = t_e - L = t - L \qquad \vec{x}_p = L\hat{p}\,, \tag{1.159a}$$

$$t_e = t \qquad \vec{x}_e = 0\,, \tag{1.159b}$$

where the indices "e" and "p" refer to the Earth and the pulsar and L is the distance to the pulsar. In this frame we can therefore write Eq (1.153) using Eq (1.113b)

$$\Delta h_{ij}(t,\hat{\Omega}) = \sum_A \int_{-\infty}^{\infty} df e^A_{ij}(\hat{\Omega})\; h_A(f,\hat{\Omega})\, e^{i2\pi ft} \left[1 - e^{-i2\pi fL(1+\hat{\Omega}\cdot\hat{p})}\right]\,. \tag{1.160}$$

The fractional frequency shift produced by a stochastic background is simply given by integrating Eq. (1.152) over all directions. Using Eqs (1.160) and (1.154),

we obtain:

$$\begin{aligned} z(t) &= \int d\hat{\Omega}\, z(t,\hat{\Omega}) \\ &= \sum_A \int_{-\infty}^{\infty} df \int_{S^2} d\hat{\Omega} F^A(\hat{\Omega}) h_A(f,\hat{\Omega}) e^{i2\pi f t} \left[1 - e^{-i2\pi f L(1+\hat{\Omega}\cdot\hat{p})}\right] \end{aligned} \quad (1.161)$$

where $F^A(\hat{\Omega})$ are the antenna beam patterns for each polarization A, defined as

$$F^A(\hat{\Omega}) = \left[\frac{1}{2}\frac{\hat{p}^i\hat{p}^j}{1+\hat{\Omega}\cdot\hat{p}}\, e^A_{ij}(\hat{\Omega})\right] . \quad (1.162)$$

Regardless of whether the analysis is carried out in a frequentist framework, and therefore one considers a detection statistic, see e.g. Anholm et al. [2009], or one builds a Bayesian analysis, e.g. van Haasteren et al. [2009], the key physical quantity that is exploited is the correlation of the timing residuals for every pair of pulsars timed by a PTA.

The expected value of the correlation between a residual $r(t)$, see Eq (1.155), from a pulsar, say a, at time t_j, with that from a different pulsar, say b, at time t_k depends on terms of the form:

$$\begin{aligned} \langle r_a^*(t_j) r_b(t_k)\rangle &= \left\langle \int^{t_j} dt' \int^{t_k} dt'' z_a^*(t') z_b(t'') \right\rangle \\ &= \left\langle \int^{t_j} dt' \int^{t_k} dt'' \int_{-\infty}^{+\infty} df' \int_{-\infty}^{+\infty} df'' \tilde{z}_a^*(f') \tilde{z}_b(f'')\, e^{-i2\pi(f't' - f''t'')} \right\rangle \\ &= \int^{t_j} dt' \int^{t_k} dt'' \int_{-\infty}^{+\infty} df e^{-i2\pi f(t'-t'')} H(f)\, {}^{(ab)}\Gamma(f). \end{aligned} \quad (1.163)$$

In analogy with Allen and Romano [1999], we define the quantity in the previous equation that depends on the relative location of the pulsars in the PTA, and the

angular distribution of the GW energy density as the *overlap reduction function*:

$$^{(ab)}\Gamma(f) \equiv \int d\hat{\Omega}\kappa_{ab}(f,\hat{\Omega}) \left[\sum_A F_a^A(\hat{\Omega})F_b^A(\hat{\Omega})\right], \tag{1.164}$$

where

$$\kappa_{ab}(f,\hat{\Omega}) \equiv \left[1 - e^{i2\pi f L_a(1+\hat{\Omega}\cdot\hat{p}_a)}\right]\left[1 - e^{-i2\pi f L_b(1+\hat{\Omega}\cdot\hat{p}_b)}\right]. \tag{1.165}$$

In Eq (1.163), the frequency spectrum of the background, whether from SMBHBs or other sources or processes in the early Universe, is described by the function $H(f)$, and $^{(ab)}\Gamma(f)$ contains information about the angular distribution of GW background power. Under the assumption that the background is isotropic, $^{(ab)}\Gamma(f)$ is a known function that simply depends on the location of the pulsars timed by the array.

In this case, the overlap reduction function (ORF) (1.164) becomes:

$$^{(ab)}\Gamma(f) = \int d\hat{\Omega}\,\kappa_{ab}(f,\hat{\Omega}) \sum_A F_a^A(\hat{\Omega})F_b^A(\hat{\Omega}), \tag{1.166}$$

which is the result derived by Hellings and Downs [1983] and is known (up to a normalization constant) as the Hellings and Downs curve, which will be calculated explicitly in Sec 1.7. Eq (1.166) can be further simplified if one assumes that many radiation wavelengths separate the pulsars from the Earth and from each other, i.e. that $fL \gg 1$. If this is the case, the contribution from κ_{ab} quickly converges to zero, such that Eq (1.166) becomes and Earth-term-only expression, except for the auto-correlation, when pulsar a = pulsar b. In this instance, the GWs add coherently at the pulsar, and $\kappa_{ab} \sim 2$. Therefore in general $\kappa_{ab} \approx 1 + \delta_{ab}$.

This concept is further explored in Sec 2.3, and Chapter 3 explores where this assumption breaks down.

1.7 The Hellings and Downs Curve

For a pair of pulsars a and b, the we define a reference frame by first placing pulsar a on the z-axis and pulsar b in the $x-z$ plane. One can explicitly write geometry as follows:

$$\hat{p}_a = (0, 0, 1), \tag{1.167a}$$

$$\hat{p}_b = (\sin\zeta, 0, \cos\zeta), \tag{1.167b}$$

$$\hat{\Omega} = (\sin\theta\cos\phi, \sin\theta\sin\phi, \cos\theta), \tag{1.167c}$$

$$\hat{m} = (\sin\phi, -\cos\phi, 0), \tag{1.167d}$$

$$\hat{n} = (\cos\theta\cos\phi, \cos\theta\sin\phi, -\sin\theta), \tag{1.167e}$$

where ζ is the angular separation of the two pulsars, $\cos\zeta = \hat{p}_a \cdot \hat{p}_b$, see Fig 1.7. In this frame $F_a^\times = 0$, and Eq. (1.164) reduces to

$${}^{(ab)}\Gamma_l^m = (1 + \delta_{ab}) \int_{S^2} d\hat{\Omega}\, F_a^+(\hat{\Omega}) F_b^+(\hat{\Omega}). \tag{1.168}$$

It is now straightforward to compute the antenna beam patterns, F_a^A and F_b^A:

$$F_a^{\times} = 0, \tag{1.169a}$$

$$F_a^{+} = -\frac{1}{2}(1-\cos\theta), \tag{1.169b}$$

$$F_b^{\times} = \frac{(\sin\phi\ \sin\zeta)(\cos\theta\sin\zeta\cos\phi - \sin\theta\cos\zeta)}{1+\cos\theta\cos\zeta+\sin\theta\sin\zeta\cos\phi}, \tag{1.169c}$$

$$F_b^{+} = \frac{1}{2}\frac{(\sin\phi\sin\zeta)^2 - (\sin\zeta\cos\theta\cos\phi - \sin\theta\cos\zeta)^2}{1+\cos\theta\cos\zeta+\sin\theta\sin\zeta\cos\phi}. \tag{1.169d}$$

Substituting Eq. (1.169) into Eq. (1.168), the overlap reduction functions become:

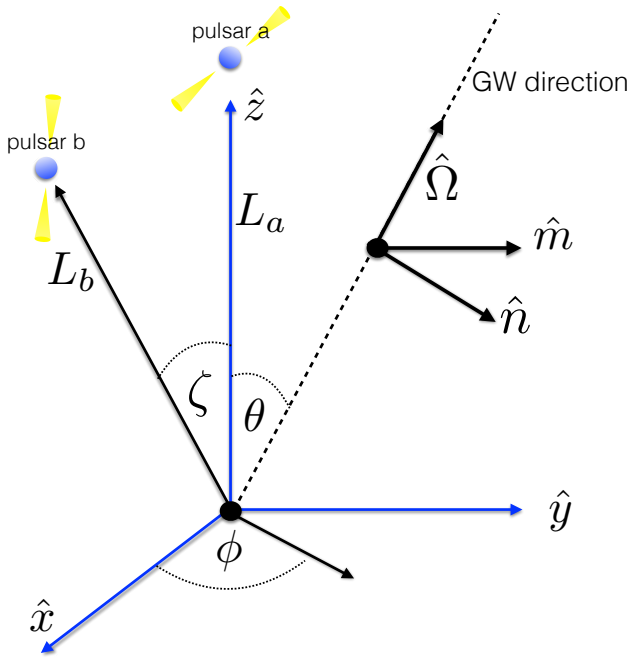

Figure 1.7: The "computational" reference frame: pulsar a is on the z-axis at a distance L_a from the origin, pulsar b is in the x-z plane at a distance L_b from the origin making an angle ζ with pulsar a, $\hat{\Omega}$ is the direction of GW propagation and $\hat{m}\times\hat{n}=\hat{\Omega}$. The polar and azimuthal angles are given by θ and ϕ, respectively.

$$
{}^{(ab)}\Gamma = -\frac{1}{4}(1+\delta_{ab})
$$
$$
\times\int_0^{\pi} d\theta \sin\theta \int_0^{2\pi} d\phi \frac{(1-\cos\theta)[(\sin\phi\sin\zeta)^2 - (\sin\zeta\cos\theta\cos\phi - \sin\theta\cos\zeta)^2]}{1+\sin\zeta\sin\theta\cos\phi+\cos\zeta\cos\theta}. \tag{1.170}
$$

One can write Eq (1.170) as the sum of two integrals:

$$
{}^{(ab)}\Gamma = \frac{1}{4}(Q+R)(1+\delta_{ab})\,, \tag{1.171}
$$

where

$$
Q = N\int_0^{\pi} d\theta \sin\theta(1-\cos\theta)\int_0^{2\pi} d\phi(1-\cos\zeta\cos\theta-\sin\zeta\sin\theta\cos\phi) \tag{1.172}
$$

where $N = 1/\sqrt{4\pi}$ and

$$
R = -2N\sin^2\zeta\int_0^{\pi} d\theta\sin\theta(1-\cos\theta)I\,, \tag{1.173}
$$

where

$$
I \equiv \int_0^{2\pi} d\phi \frac{\sin^2\phi}{1+\cos\zeta\cos\theta+\sin\zeta\sin\theta\cos\phi}\,. \tag{1.174}
$$

Evaluating Eqs (1.173) and (1.172), one obtains

$$
\begin{aligned}
Q &= \frac{1}{\sqrt{4\pi}}\int_0^{\pi} d\theta\sin\theta(1-\cos\theta)\int_0^{2\pi} d\phi(1-\cos\zeta\cos\theta-\sin\zeta\sin\theta\cos\phi),\\
&= \frac{2\pi}{\sqrt{4\pi}}\int_0^{\pi} d\theta\sin\theta(1-\cos\theta)(1-\cos\theta\cos\zeta),\\
&= \sqrt{4\pi}\left(1+\frac{\cos\zeta}{3}\right).
\end{aligned} \tag{1.175}
$$

When solving for R, note that the "I" integral, Eq (1.174), is evaluated via contour integration in Anholm et al. [2009]. In this work, a symbolic program was used to evaluate it[1]. Integrating Eq (1.174), one obtains

$$I = 2\pi \frac{1 + \cos\zeta\cos\theta - |\cos\zeta + \cos\theta|}{\sin^2\zeta \sin^2\theta} \tag{1.176}$$

$$I = 2\pi \begin{cases} \left(\frac{1-\cos\zeta}{\sin^2\zeta}\right)\left(\frac{1-\cos\theta}{\sin^2\theta}\right), & 0 < \theta < \pi - \zeta \\ \left(\frac{1+\cos\zeta}{\sin^2\zeta}\right)\left(\frac{1+\cos\theta}{\sin^2\theta}\right), & \pi - \zeta < \theta < \pi \end{cases} \tag{1.177}$$

The final form of Eq (1.173) is therefore

$$\begin{aligned} R &= -\sqrt{4\pi}\left[(1-\cos\zeta)\int_0^{\pi-\zeta} d\theta \frac{(1-\cos\theta)^2}{\sin\theta} - (1+\cos\zeta)\int_{\pi-\zeta}^{\pi} d\theta \sin\theta\right], \\ &= \sqrt{4\pi}(1-\cos\zeta) 4 \ln\left(\sin\frac{\zeta}{2}\right). \end{aligned} \tag{1.178}$$

Using Eq (1.171), one may write the isotropic solution to Eq (1.170):

$${}^{(ab)}\Gamma = \frac{\sqrt{\pi}}{2}\left[1 + \frac{\cos\zeta}{3} + 4(1-\cos\zeta)\ln\left(\sin\frac{\zeta}{2}\right)\right](1+\delta_{ab}). \tag{1.179}$$

This equation is the Hellings and Downs curve up to a multiplicative factor $4\sqrt{\pi}/3$, which is used to normalize the curve such that it has a maximum value of 1.0 at $\zeta = 0$, *i.e.* pulsar a = pulsar b.

Note that for an isotropic stochastic GW background, the detector response for $\zeta = 0$ is twice that of $\zeta = \pi$, see Fig 1.8. Considering the response to an

[1]Note that there is a sign typo in Anholm et al. [2009]'s appendix in the equation above C9 (it does not have a number). Eq (1.176) has the correct sign. This was first reported in Mingarelli et al. [2013]

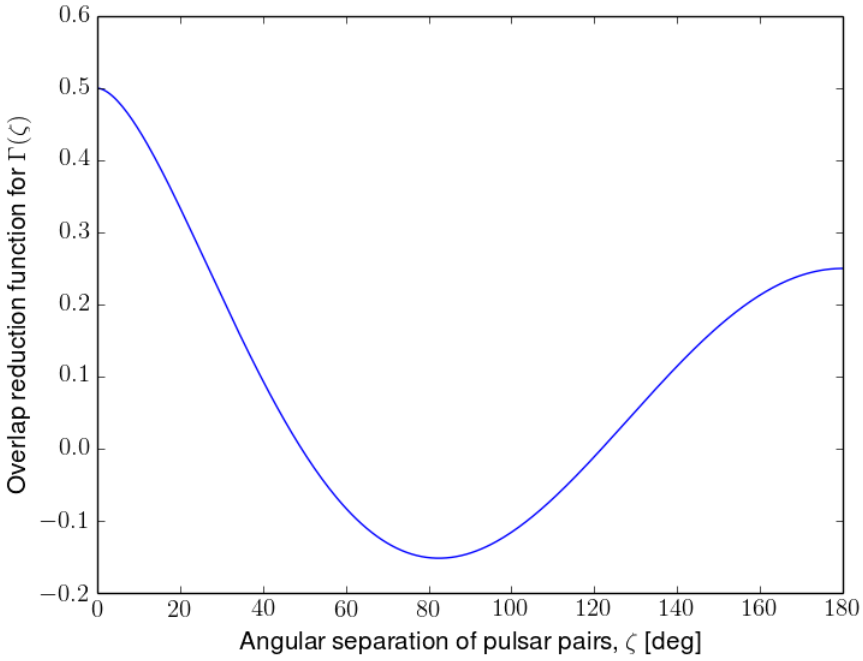

Figure 1.8: The overlap reduction function for an isotropic stochastic GW background, called the Hellings and Downs curve.

incoming GW at some angle θ may help one to understand this observation. If $\zeta = 0$, which is the case for coincident and co-aligned pulsars (i.e. $a = b$), the antenna beam pattern, Eq (1.169), is given by

$$F_a^+ F_b^+ = \frac{1}{2}(1-\cos\theta)\frac{1}{2}(1-\cos\theta) \tag{1.180}$$

$$= \frac{1}{4}(1-\cos\theta)^2. \tag{1.181}$$

Note that in this particular geometry, there is no ϕ dependence. Integrating this response over $d\hat{\Omega} = \sin\theta d\theta$ gives

$$\frac{1}{4}\int_0^\pi d\theta \sin\theta(1-\cos\theta)^2 = \frac{2}{3}. \tag{1.182}$$

When $\zeta = \pi$, the antenna beam pattern is given by

$$F_a^+ F_b^+ = \frac{1}{2}(1-\cos\theta)\frac{1}{2}[1-\cos(\pi-\theta)] \quad (1.183)$$

$$= \frac{1}{4}\sin^2\theta\,, \quad (1.184)$$

and integrating over θ yields

$$\frac{1}{4}\int_0^\pi d\theta \sin\theta(\sin^2\theta) = \frac{1}{3}. \quad (1.185)$$

It is therefore clear that particular geometries are more (or less) sensitive to stochastic background signals. Note that this is an Earth-term-only argument, and does not take into account the pulsar term which adds an additional factor of 2 to the ORF at $\zeta = 0$.

More generally, this dependence can be explained in terms of the alignment of the GW direction, $\hat{\Omega}$ and the position of the pulsar, $\hat{p}$, see Fig 1.7. The product $\hat{\Omega}\cdot\hat{p}$ enters into the ORF via the antenna beam patterns given in Eq (1.162), where $F^+_{a,b} \propto (1+\hat{\Omega}\cdot\hat{p})^{-1}$, and κ_{ab}, Eq (1.165). When $\hat{\Omega}$ is parallel or antiparallel to $\hat{p}$, $\hat{\Omega}\cdot\hat{p} = \pm 1$.

When $\hat{\Omega}\cdot\hat{p} = -1$, the photons emitted from the pulsar surf the GWs, and there is no redshift. This surfing effect can be seen mathematically when considering the metric perturbation including the pulsar term: since the signal at the Earth is the same as the signal at the pulsar, $\Delta h_{ij}(t,\hat{\Omega}) = 0$, cf. Eq (1.153). Note however that the ORF is integrated over the whole sky, and this is just one piece of the integration.

One may also be concerned with the case where $\hat{\Omega}\cdot\hat{p} = 1$, since there appears

to be a divergence in the antenna beam pattern caused by zero division. If however the complete antenna beam pattern is considered, then

$$F_a^+ = -\frac{1}{2}\frac{\sin^2\theta}{1+\cos\theta} = -\frac{1}{2}(1-\cos\theta)\,, \tag{1.186}$$

which is just Eq (1.169), where the numerator has been computed from $p^i p^j e_{ij}^+ = -\sin^2\theta$ for pulsar a on the z-axis. When $\hat{\Omega}\cdot\hat{p} = 1$, then $\theta = 0$ and $F_a^+ = 0$. Note as well that in this case the photons from the pulsar travel over the maximum number of radiation wavelengths, fL, resulting in a significant amount of "stretching and squashing", cf. Figs 1.2, 1.7. The additional phases introduced by the GW then largely cancel out, limiting the detector response.

1.8 Thesis Summary

Detecting a stochastic gravitational wave background, particularly radiation from individually unresolvable SMBHB systems, is one of the primary targets for Pulsar Timing Arrays. Increasingly more stringent upper limits are being set on these signals under the assumption that the background radiation is isotropic. However, some level of anisotropy may be present and the characterization of the gravitational wave energy density at different angular scales carries important information. In Chapter 2, we show that the standard analysis for isotropic backgrounds can be generalized in a conceptually straightforward way to the case of generic anisotropic background radiation by decomposing the angular distribution of the gravitational wave energy density on the sky into multipole moments. We introduce the concept of generalized overlap reduction functions which char-

acterize the effect of the anisotropy multipoles on the correlation of the timing residuals from the pulsars timed by a Pulsar Timing Array. In a search for a signal characterized by a generic anisotropy, the generalized overlap reduction functions play the role of the so-called Hellings and Downs curve used for isotropic radiation. We compute the generalized overlap reduction functions for a generic level of anisotropy and Pulsar Timing Array configuration. We also provide an order of magnitude estimate of the level of anisotropy that can be expected in the background generated by SMBHB systems.

Current stochastic background searches assume that pulsars in a PTA are separated from each other and the Earth by many GW wavelengths, and that all pulsars lie at the same distance L from the Earth. As more millisecond pulsars are discovered and added to PTAs, some may indeed be separated by less than a radiation wavelength, resulting in correlated GW phase changes between close pulsars in the array. In Chapter 3 we investigate how PTA overlap reduction functions (ORFs), up to quadrupole order, are affected by these additional correlated phase changes, and how these correlated phase changes are in turn affected by relaxing the assumption that all pulsars are equidistant from the Earth. We find that in the low frequency GW background limit of $f = 10^{-9}$ Hz, and for pulsars at varying distances from the Earth, that these additional correlations only affect the ORFs by a few percent for pulsar pairs at large angular separations, as expected. However when nearby (order of 100 pc) pulsars are separated by less than a radiation wavelength in the low frequency limit, the correlated phase changes can introduce variations of up to a factor of about three in the magnitude of the ORF. These correlated phase changes rapidly converge to zero, however this convergence is slower particularly for the quadrupole ($l = 2$) ORFs. We

write down a small angle approximation for the correlated phase changes which can easily be implemented in search pipelines, and for completeness, examine the behaviour of the ORFs for pulsars which lie at a radiation wavelength from the Earth.

In Chapter 4, we show that the detection of gravitational radiation from individually resolvable super-massive black hole binary systems can yield direct information about the masses and spins of the black holes, provided that the gravitational-wave induced timing fluctuations both at the pulsar and at the Earth are detected. This in turn provides a map of the non-linear dynamics of the gravitational field and a new avenue to tackle open problems in astrophysics connected to the formation and evolution of super-massive black holes. We discuss the potential, the challenges and the limitations of these observations.

Conclusions and work in progress are presented in Chapter 5.

Chapter 2

CHARACTERIZING GRAVITATIONAL WAVE STOCHASTIC BACKGROUND ANISOTROPY WITH PULSAR TIMING ARRAYS

This chapter is based on: C. M. F. Mingarelli, T. Sidery, I. Mandel, A. Vecchio, "Characterizing stochastic gravitational wave background anisotropy with pulsar timing arrays", Physical Review D, Vol 88, 062005 (2013), cited as Mingarelli et al. [2013]. I wrote the draft of this paper, derived all of the generalized overlap reduction functions, examined the behaviour of the pulsar term, wrote the codes and made all of the figures.

2.1 Introduction

The detection of gravitational waves (GWs) is one of the key scientific goals of Pulsar Timing Arrays (PTAs). A PTA uses a network of radio telescopes to regularly monitor stable millisecond pulsars, constituting a galactic-scale GW detector Ferdman et al. [2010]; Hobbs et al. [2010]; Jenet et al. [2009]; Verbiest et al. [2010]. Gravitational radiation affects the propagation of radio pulses between a pulsar and a telescope at the Earth. The difference between the expected and actual time-of-arrival (TOA) of the pulses – the so-called timing residuals – carries information about the GWs Detweiler [1979]; Estabrook and Wahlquist [1975]; Sazhin [1978], which can be extracted by correlating the residuals from different pulsar pairs. This type of GW detector is sensitive to radiation in the $10^{-9} - 10^{-7}$ Hz frequency band, a portion of the spectrum in which a promising class of sources are super-massive black hole binary (SMBHB) systems with masses in the range of $\sim 10^7 - 10^9 M_\odot$ during their slow, adiabatic in-spiral phase Jaffe and Backer [2003]; Rajagopal and Romani [1995]; Sesana [2013]; Sesana et al. [2008, 2009]; Wen et al. [2011]; Wyithe and Loeb [2003]. Other forms of radiation could be observable by PTAs, such as cosmic strings Kuroyanagi et al. [2013]; Pshirkov and Tuntsov [2010]; Sanidas et al. [2012] and/or a background produced by other speculative processes in the early universe, see *e.g.* Zhao [2011].

A PTA can be thought of as an all-sky monitor that is sensitive to radiation from the whole cosmic population of SMBHBs radiating in the relevant frequency band. The overwhelming majority of sources are individually unresolvable, but the incoherent superposition of the very weak radiation from the many binaries

in the population gives rise to a stochastic background[1] whose detection is within reach of current or planned PTAs Sesana [2013]; Sesana et al. [2008]; Siemens et al. [2013]. In addition, some of the binaries may be sufficiently luminous to stand out above the diffuse background level and could be individually observed Sesana and Vecchio [2010]; Yardley et al. [2010]. The search for GWs from a SMBHB background Demorest et al. [2013]; Hellings and Downs [1983]; Jenet et al. [2006]; van Haasteren et al. [2011] and from individual resolvable sources Babak and Sesana [2012]; Ellis et al. [2012a,b]; Jenet et al. [2004]; Lee et al. [2011]; Yardley et al. [2010] has recently catalysed the PTA GW search effort, and it is plausible that in the next 5 to 10 years GWs could indeed be detected. If not, stringent constraints can be placed on aspects of the assembly history of SMBHBs Koushiappas and Zentner [2006]; Malbon et al. [2007]; Volonteri et al. [2003]; Yoo et al. [2007].

In all the searches carried out so far, it has been assumed that the stochastic background, regardless of its origin, is isotropic Demorest et al. [2013]; Hellings and Downs [1983]; Jenet et al. [2006]; van Haasteren et al. [2011]. This is well justified if the background is produced by some physical processes in the early universe or is largely dominated by high-redshift sources. Under the assumption of isotropy, the correlated output from the data from any two pulsars in the array depends only on the angular separation of the pulsars and is known as the Hellings and Downs curve Hellings and Downs [1983]. However, a PTA also carries information about the angular distribution of the GW power on the sky. It is therefore important to address how this information is encoded in the data, and the implications for analysis approaches. In fact, if evidence for a signal is found

[1]It would be more appropriate to call this radiation a *foreground*, but to be consistent with the established terminology we will keep referring to it as a *background*.

in the data, testing the assumption of isotropy could be one of the methods to confirm its cosmological origin. If, on the other hand, one expects some deviations from isotropy, which may be the case for the SMBHB background created by a finite population, e.g. Cornish and Sesana [2013]; Ravi et al. [2012], it is useful to be able to extract constraints on the underlying physical population.

In this paper we show how the correlated output from pulsar pairs in a PTA is related to the anisotropy of the signal, *i.e.* the angular distribution of GW power on the sky, and how one can extract this information by measuring the multipole moments that characterise the anisotropy level, following an analogous approach to those applied to the case of ground-based Allen and Ottewill [1997] and space-based Cornish [2002] laser interferometric observations. By doing this, we generalize the Hellings and Downs curve to an arbitrary angular distribution on the sky. We also provide an estimate for the expected level of anisotropy for the background produced by an arbitrary population of sources, and in particular, the population of SMBHB systems.

The paper is organized as follows. In Section 2.2, we estimate the expected level of anisotropy in a background produced by a population of SMBHB systems. We show that at low frequencies, where the PTA sensitivity is optimal and the number of sources that contribute to the background is very large, the expected level of anisotropy is small, and likely undetectable. However towards the high-frequency end of the sensitivity window, where the actual number of sources decreases sharply, the anisotropy level could be significant, increasing at smaller angular scales. In Section 2.3 we show that the present analysis approaches for isotropic backgrounds can be generalized in a conceptually straightforward way to the case of anisotropic signals by decomposing the angular distribution of the

GW power on the sky into multipole moments. We introduce the concept of *generalized overlap reduction functions*, which replace the Hellings and Downs curve. Each one of these characterizes the effect of a given anisotropy multipole on the correlation of the timing residuals from a pulsar pair. In Section 2.4 we derive expressions for the generalized overlap reduction functions for an arbitrary stochastic background angular distribution on the sky and PTA configuration. This is essential for future analyses of PTA data which include anisotropy as part of the model. Section 2.5 contains our conclusions and suggestions for future work.

2.2 Approximate level of anisotropy in the stochastic GW background

Until now, it has been assumed that the stochastic GW background is isotropic. We now relax this assumption: each direction on the sky need not contribute to the stochastic GW background in the same way, and the function $P(\hat{\Omega})$ describes this angular dependence (the "hot" and "cold" spots). As in Allen and Ottewill [1997], we decompose the angular distribution function on the basis of the spherical harmonic functions,

$$P(\hat{\Omega}) \equiv \sum_{lm} c_l^m Y_l^m(\hat{\Omega}) \,, \tag{2.1}$$

where the sum is over $0 \leq l < +\infty$, and $|m| \leq l$. The coefficients c_l^m are the multipole moments of the radiation which characterise the angular distribution of the background. We adopt the convention that the monopole moment is normalized

as

$$c_0^0 = \sqrt{4\pi}\,. \tag{2.2}$$

The angular distribution of the radiation is encoded in the values of the radiation multipole moments c_l^m, which become unknown parameters in the analysis. In Section 2.4 we will show how the c_l^m's enter the likelihood function of PTA timing residuals, and how an arbitrary angular distribution affects the correlation of radiation at any two pulsars timed by an array. This provides a way of measuring the multipole moments. In the remainder of this Section we provide an estimate of the expected level of anisotropy in a background generated by the population of SMBHB systems.

In order to gain some insight into this problem, let us consider an idealized situation, constructed as follows. Let us assume that the universe is populated by identical sources with number density n. If we want to estimate the level of anisotropy, we need to estimate the expected value of the energy density in GWs coming from sources in a solid angle $d\Omega$ centred on a direction $\hat{\Omega}$ and compare it to the energy density produced by sources in a cone centred on a different direction $\hat{\Omega}'$. For this example we consider a Euclidean, static universe (or equivalently sufficiently nearby sources, such that we do not take into account effects of expansion and redshift).

In a conical volume $dV = D^2 dD d\Omega$ within the solid angle $d\Omega$ and at distance between D and $D + dD$, the expected number of sources which contribute to the background is:

$$dN = nD^2 dD d\Omega\,. \tag{2.3}$$

The actual number of sources is then governed by Poisson statistics, with mean

$\mu = dN$ and variance $\sigma^2 = dN$. If the volume dV is sufficiently small that $dN \ll 1$, then the probability of finding one source is

$$P(1) = dNe^{-dN} \approx dN. \tag{2.4}$$

Since the probability of having more than one source within this volume is negligible, the probability of finding no sources is simply $1 - P(1) = 1 - dN$.

The expected total number of sources, μ_N, present in the whole volume within a solid angle $d\Omega$ between the minimum and maximum distance, D_m and D_M, respectively (to be discussed later), is given by the sum of the contributions from each slice in the cone. Similarly, the variance σ_N^2 is the sum of the variances from each conical slice. We therefore obtain

$$\mu_N = \sigma_N^2 = \int_{D_m}^{D_M} nD^2 dD d\Omega \,, \tag{2.5a}$$

$$= \left(n\frac{4\pi}{3}D_M^3\right)\left(\frac{d\Omega}{4\pi}\right)\left[1 - \left(\frac{D_m}{D_M}\right)^3\right] . \tag{2.5b}$$

We now want to compute the expected contribution to the GW energy density per frequency interval and its variance. The GW energy density of each source scales as $1/D^2$. If we assume that all the sources are identical – the generalization to a distribution of masses is straightforward, but is not needed to explain the key points – we can write (with slight abuse of notation) the contribution to the energy density per source simply as

$$\frac{d\rho_{\rm gw}}{dN} = \frac{A}{D^2} \,, \tag{2.6}$$

where A is an appropriate constant factor, equal for all sources.

The expected GW energy density from sources in a small conical volume dV at distance D, again chosen so that it has a vanishingly small probability of having more than one source, $dN \ll 1$, see Eqs. (2.3) and (2.4), is

$$d\mu_{\rm gw}(D) \approx P(1)\frac{d\rho_{\rm gw}}{dN} \approx dN\frac{A}{D^2} = nAdDd\Omega\,, \tag{2.7}$$

The variance of the energy density from sources in this conical volume is

$$d\sigma^2_{\rm gw}(D) \approx P(1)\left(\frac{d\rho_{\rm gw}}{dN}\right)^2 - \left(d\mu_{\rm gw}(D)\right)^2 \approx \frac{nA^2}{D^2}dDd\Omega, \tag{2.8}$$

where the last equality relies on the consistent application of the condition $dN \ll 1$ (which can always be satisfied by choosing a sufficiently small shell thickness dD).

We can now compute the expected contribution to the GW energy density $\mu_{\rm gw}$ and its variance $\sigma^2_{\rm gw}$ from all sources in a solid angle $d\Omega$. The mean energy density and variance are given by the sum of contributions from all slices of thickness dD; using Eqs. (2.7) and (2.8), this yields:

$$\begin{aligned}
\mu_{\rm gw} &= \int_{D_m}^{D_M} \frac{d\mu_{\rm gw}(D)}{dD}\, dD\,, && \text{(2.9a)}\\
&= nAd\Omega \int_{D_m}^{D_M} dD\,, && \text{(2.9b)}\\
&= nAD_M\left[1 - \frac{D_m}{D_M}\right] d\Omega\,, && \text{(2.9c)}
\end{aligned}$$

and, using the fact that the variance of a sum is the sum of variances,

$$\sigma^2_{\rm gw} = \int_{D_m}^{D_M} \frac{d\sigma^2_{\rm gw}(D)}{dD}\, dD\,, \tag{2.10a}$$

$$= nA^2 d\Omega \int_{D_m}^{D_M} \frac{dD}{D^2}\,, \tag{2.10b}$$

$$= nA^2 \left[\frac{D_M - D_m}{D_M D_m}\right] d\Omega\,. \tag{2.10c}$$

We define the level of anisotropy as the ratio of the standard deviation in the GW power emanating from a given solid angle to the expected power from that angle:

$$\frac{\sigma_{\rm gw}}{\mu_{\rm gw}} = (nd\Omega)^{-1/2} \left[(D_M - D_m) D_M D_m\right]^{-1/2}$$

$$= \left(nD_M^3 d\Omega\right)^{-1/2} \left[\left(1 - \frac{D_m}{D_M}\right) \frac{D_m}{D_M}\right]^{-1/2}. \tag{2.11}$$

We can now return to the choice of the minimal and maximal distance, D_m and D_M. The maximal distance at which sources can be located is set by cosmology and the history of SMBH formation. Meanwhile, the minimal distance of interest to us, D_m, corresponds to the maximal distance at which individual binaries can be resolved. Individually resolvable binaries can be subtracted from the data, and are treated separately from the stochastic background. An individual source can be efficiently searched for with matched filtering techniques, see e.g. Babak and Sesana [2012]; Ellis et al. [2012a,b]; Petiteau et al. [2013]. Therefore, we expect the power necessary to detect a single SMBH binary to be significantly less than the power necessary to measure a stochastic background. Thus, in order for a stochastic background to be detectable *after all individual sources*

that are presumed to be detectable up to distance D_m are removed, the total power in the background must be significantly greater than the power in the weakest individually resolvable source:

$$4\pi n A D_M \left[1 - \frac{D_m}{D_M}\right] \gg \frac{A}{D_m^2}. \tag{2.12}$$

Another way to interpret the preceding condition is to consider the idealized situation when the stochastic background provides the dominant noise source: optimal matched filtering would make it possible to individually resolve and subtract coalescing SMBH binaries with signal power far below the noise (background) levels.

We can recast the condition on the detectability of a stochastic background, Eq. (2.12), as

$$\left(n D_M^3\right) \left(\frac{D_m}{D_M}\right)^2 \left[1 - \left(\frac{D_m}{D_M}\right)\right] \gg 1\,. \tag{2.13}$$

If we define $y \equiv D_m/D_M$, where $0 \leq y \leq 1$, this condition yields

$$\left(n D_M^3\right)\, y^2\,(1-y) \gg 1\,, \tag{2.14}$$

where nD_M^3 is the total number of sources in the universe, modulo a factor of order unity. We can now rewrite the level of anisotropy (2.11) in the following form:

$$\frac{\sigma_{\rm gw}}{\mu_{\rm gw}} = \left\{\left(\frac{1}{d\Omega}\right)\left[\frac{y}{(nD_M^3)\,(1-y)y^2}\right]\right\}^{1/2} \tag{2.15a}$$

$$= \left[\left(\frac{4\pi}{d\Omega}\right)\frac{\alpha(y)}{N_0}\right]^{1/2}, \tag{2.15b}$$

where $N_0 = (4\pi/3)nD_M^3(1-y^3)$ is the total number of sources that contribute to the background and $\alpha(y) \equiv (y^2+y+1)/(3y)$. Note that by virtue of condition (2.14), the second term in Eq.(2.15a) is always smaller than unity whenever the stochastic background is detectable, and is actually $\ll 1$. The level of anisotropy scales as $N_0^{-1/2}$, and increases by going to small angular scales $d\Omega$. However, there is an observational limit on the angular resolution of PTAs which will prevent very small angular scales from being probed. Furthermore, at smaller angular scales, the signal will be progressively dominated by a smaller number of, possibly individually unresolvable, sources. The number of sources in a cone of solid angle $d\Omega$ is

$$\mu_N = \frac{nD_M^3 d\Omega}{3}\left[1-\left(\frac{D_m}{D_M}\right)^3\right], \tag{2.16a}$$

$$= \frac{d\Omega}{3}\left(nD_M^3\right)(1-y^3), \tag{2.16b}$$

$$= \left(\frac{d\Omega}{4\pi}\right)N_0. \tag{2.16c}$$

When this quantity is larger but not *much* larger than unity, we expect to be in the middle ground between searches for individual sources and standard stochastic-background searches. If this occurs on resolvable angular scales where anisotropy is significant (cf. Eq. (2.15a) and Eq. (2.18) below), it will be interesting to check the efficiency of current search pipelines in this regime.

Using the results from *e.g.* Sesana et al. [2008] we can provide an order-of-magnitude estimate of the expected level of anisotropy that characterizes the SMBHB background. From Figure 4 of Sesana et al. [2008], reproduced in Fig 1.4 we can see that the total number of sources that contribute in a frequency

interval of width $T_{\rm obs}$, where $T_{\rm obs}$ is the observation time, can be approximated as:

$$N_0 \approx 5 \times 10^5 \left(\frac{f}{10^{-8}\,\mathrm{Hz}}\right)^{-11/3} \left(\frac{5\,\mathrm{yr}}{T_{\rm obs}}\right) , \tag{2.17}$$

where we used the fact that, during a SMBHB inspiral, the time the binary spends in a given frequency band scales as $dt/df \propto f^{-11/3}$, Eq (1.71). Substituting Eq. (2.17) into Eq. (2.15b) and converting between the average angular scale $d\Omega$ and the multipole moment index l using $d\Omega = 4\pi/2l$, we obtain:

$$\begin{aligned} \frac{\sigma_{\rm gw}(f)}{\mu_{\rm gw}(f)} &\approx 3 \times 10^{-3} \left(\frac{f}{10^{-8}\,\mathrm{Hz}}\right)^{11/6} \left(\frac{5\,\mathrm{yr}}{T_{\rm obs}}\right)^{-1/2} \left(\frac{l}{2}\right)^{1/2} \alpha^{1/2} , \\ &\approx 0.2 \left(\frac{f}{10^{-7}\,\mathrm{Hz}}\right)^{11/6} \left(\frac{5\,\mathrm{yr}}{T_{\rm obs}}\right)^{-1/2} \left(\frac{l}{2}\right)^{1/2} \alpha^{1/2} . \end{aligned} \tag{2.18}$$

There will be few SMBHBs beyond redshift ~ 5, and individual sources are likely to be resolvable up to redshift ~ 1, so sources that contribute to the stochastic background are within redshift range $\approx$ 1–5, see *e.g.* Sesana et al. [2008] and Fig 1.4. Therefore, both y and α will be factors of order unity. We have confirmed this with a more careful calculation that takes cosmology and the redshifting of gravitational waves into account; however, we note that our simplified treatment relied on a constant density (rate) of coalescing SMBHBs in the Universe, and on a fixed amplitude at a given frequency for all sources, which corresponds to the assumption of a fixed source mass.

As expected, the level of anisotropy at low frequencies and large angular scales is small. However, it can become non-negligible, at the tens of percent level, at frequencies $\sim 10^{-7}$ Hz.

2.3 Anisotropic stochastic backgrounds

For an anisotropic background, whose angular power spectrum is unknown, $P(\hat{\Omega})$ is a function of the unknown angular power distribution on the sky. We can generalize the concept of the overlap reduction function, Eq (1.164), by decomposing $P(\hat{\Omega})$ on the basis of spherical harmonic functions according to Eq. (2.1). The weight of each of the components is given by an unknown coefficient c_l^m, which needs to be determined by the analysis. The overlap reduction function (1.164) therefore becomes

$$^{(ab)}\Gamma(f) = \sum_{lm} c_l^m \, {}^{(ab)}\Gamma_l^m(f) \tag{2.19}$$

where

$$^{(ab)}\Gamma_l^m(f) \equiv \int d\hat{\Omega} Y_l^m(\hat{\Omega}) \kappa_{ab}(f, \hat{\Omega}) \left[\sum_A F_a^A(\hat{\Omega}) F_b^A(\hat{\Omega}) \right] \tag{2.20}$$

are the *(complex-form) generalized overlap reduction functions*. Given an array of pulsars on the sky, the functions $^{(ab)}\Gamma_l^m$ are uniquely defined and known.

The generalization of *e.g.* the standard Bayesian analysis for an isotropic stochastic background such as the one reported in van Haasteren et al. [2009] to the case in which the assumption of isotropy is relaxed is, at least conceptually, straightforward. The model parameters that describe the stochastic background are not only those that enter the frequency spectrum $H(f)$ – for example the overall level and spectral index in the common case of a power-law parametrization of $H(f)$, appropriate for the background from SMBHBs – but also the coefficients that describe the angular distribution on the sky, that is, how much power is associated to each spherical harmonic decomposition of the overall signal. An initial implementation of this analysis is reported in Taylor and Gair [2013].

Before we compute the expressions for the generalized overlap reduction functions, it is important to consider the function $\kappa_{ab}(f,\hat{\Omega})$, defined in Eq. (1.165) and present in Eqs. (1.164) and (2.20), which introduces the frequency dependence of the overlap reduction functions. From a physical point of view $\kappa_{ab}(f,\hat{\Omega})$ encodes the fact that the correlation of the timing residuals carries information about both the Earth and pulsar terms for the two pulsars whose timing residuals are correlated. The relevant scale in the function $\kappa_{ab}(f,\hat{\Omega})$ is

$$2\pi f L(1+\hat{\Omega}\cdot\hat{p}) = 6.5\times 10^3 \left(\frac{f}{10^{-8}\,\mathrm{Hz}}\right)\left(\frac{L}{1\,\mathrm{kpc}}\right)(1+\hat{\Omega}\cdot\hat{p})\,, \tag{2.21}$$

which introduces rapid oscillations around unity, cf. Anholm et al. [2009], that depend on the distance and location to the pulsars. For all astrophysically relevant situations $fL \gg 1$, see Eq. (3.1), and when one computes the integral in Eq. (2.20) the frequency dependent contributions to the integral rapidly average out to zero as the angle between the pulsar pairs, ζ, increases. The generalized overlap reduction function Eq. (2.20) is therefore well approximated by

$${}^{(ab)}\Gamma_l^m \simeq (1+\delta_{ab})\int d\hat{\Omega}\, Y_l^m(\hat{\Omega})\left[\sum_A F_a^A(\hat{\Omega})F_b^A(\hat{\Omega})\right]\,, \tag{2.22}$$

where δ_{ab} is the Kronecker delta. We will provide some more details in Section 2.4.3. Here we note that the approximation (2.22) is equivalent to considering only the correlation of the Earth-term for two distinct pulsars. As we are considering many sources over the whole sky then the pulsar terms will only contribute to the correlation if the distance between two pulsars is of the order of one wavelength or less, and for the frequencies and pulsars being considered this

is only true for auto-correlation. The auto-correlation term carries contributions from the Earth and pulsar terms, and therefore the value of of the integral is multiplied by a factor of 2. Note also, that the generalized overlap reduction function (2.22) does not depend on frequency.

The decompositions (2.19), (2.20) and (2.22) are based on the usual complex-basis spherical harmonic functions $Y_l^m(\hat{\Omega})$, whose definitions are given in Section 2.4.2. One can alternatively consider a decomposition on a real basis $Y_{lm}(\hat{\Omega})$, that are defined in terms of their complex analogs by[1]:

$$Y_{lm} = \begin{cases} \frac{1}{\sqrt{2}}\left[Y_l^m + (-1)^m Y_l^{-m}\right] & m > 0 \\ Y_l^0 & m = 0 \\ \frac{1}{i\sqrt{2}}\left[Y_l^{-m} - (-1)^m Y_l^m\right] & m < 0 \end{cases} \tag{2.23}$$

Consequently, the real-form generalized overlap reduction functions are:

$${}^{(ab)}\Gamma_{lm} = \begin{cases} \frac{1}{\sqrt{2}}\left[{}^{(ab)}\Gamma_l^m + (-1)^m\, {}^{(ab)}\Gamma_l^{-m}\right] & m > 0 \\ {}^{(ab)}\Gamma_l^0 & m = 0 \\ \frac{1}{i\sqrt{2}}\left[{}^{(ab)}\Gamma_l^{-m} - (-1)^m\, {}^{(ab)}\Gamma_l^m\right] & m < 0 \end{cases} \tag{2.24}$$

In the next Section we compute the ${}^{(ab)}\Gamma_l^m$'s for a generic pulsar pair and discuss their properties.

[1]Here we adopt the convention that the real-form spherical harmonic functions and generalized overlap reduction functions are written with indices l and m in the subscript, whereas in the complex-from, m is raised as a superscript.

2.4 Generalised overlap reduction functions

In this Section we compute the generalized overlap-reduction functions, Eq. (2.22) for a generic pulsar pair and explore their properties. Anholm et al. [2009] considered the particular case of the overlap-reduction function between two pulsars for radiation described by dipole anisotropy. Here we go beyond, and consider an arbitrary angular distribution of the background. Our approach is based on decomposing the power of the GW background at different angular scales onto spherical harmonics, cf. Eq. (2.1) and for the specific case of a dipole distribution we show that our result is equivalent to the one presented in Anholm et al. [2009].

In the case of an isotropic background, pulsar pairs timed by a PTA map uniquely into the Hellings and Downs curve. That is to say, any pulsar pair is uniquely identified by an angular separation, which in turn corresponds to a value of the overlap reduction function. This is no longer the case for an anisotropic distribution. For a given distribution of the GW power on the sky, the generalized overlap reduction functions depend on the angular separation between two pulsars *and* their specific location in the sky with respect to the background radiation. Equivalently, if one considers two different pulsar pairs with the same angular separation but different sky locations, the overlap reduction function that describes the correlation between the two pulsars will be different. To illustrate this, we show a selection of the best pulsars currently being timed by the European Pulsar Timing Array (EPTA), see EPTA [2013][1], in Figure 2.1, where we plot the real-valued overlap reduction functions, using Eq (2.24), for

[1]These are J0613−0200; J1012+5307; J1022+1001; J1024−0719; J1600−3053; J1640+2224; J1643−1224; J1713+0747; J1730−2304; J1744−1134; J1853+1303; J1857+0943; J1909−3744; J1911+1347; J1918−0642; J1939+2134; J2145−0750 and J2317+1439.
These are the current EPTA "Priority 1" pulsars, however the prioritization is subject to change.

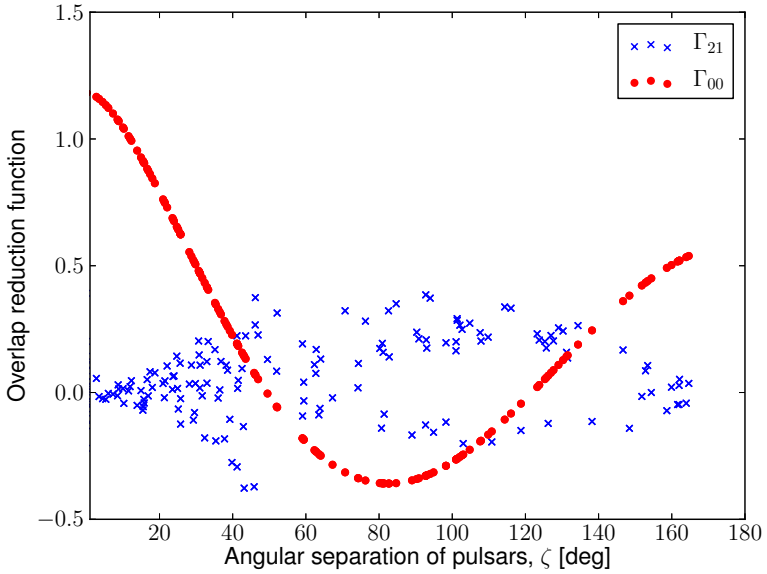

Figure 2.1: The real-value overlap reduction functions Γ_{00} and Γ_{21} for 18 EPTA pulsars in the cosmic rest-frame. Note that for illustrative purposes, we have not included the autocorrelation term ($\zeta = 0$).

the isotropic case and for $l = 2$ and $m = 1$. It can clearly be seen that the overlap reduction function no longer fits a single curve in the anisotropic case.

In our analysis we will closely follow the approach considered by Allen and Ottewill [1997], who considered the equivalent problem in the case of ground-based laser interferometers.

2.4.1 Choice of coordinate frames

We introduce a "cosmic rest-frame" where the angular dependency of the anisotropy is described, and a "computational frame", in which some of the key expressions take a particularly simple form, and provide some intuitive clues into the problem, cf. Eq (1.167). Given any two pulsars, say pulsars a and b, we define the

computational frame as the frame in which pulsar a is on the z-axis, pulsar b is in the $x-z$ plane, and their angular separation is denoted by ζ. This is the standard frame that is used in e.g. Anholm et al. [2009] to compute the Hellings and Downs curve for the isotropic case. Therefore, overlap reduction functions in the computational frame only depend on the pulsar pair's angular separation, ζ. We now outline a method where one can rotate from the cosmic rest-frame to the computational frame, and vice versa, by means of rotation matrices.

Let us consider a generic vector $\vec{v}$, and let v^u (unprimed) be the component in the cosmic rest-frame and $v^{u'}$ (primed) the component in the computational frame, which will be different for every pulsar pair. The components of the vector in the two different frames are related by:

$$\begin{aligned} v^{u'} &= R_z(\gamma)\, R_y(\beta)\, R_z(\alpha) v^u, \\ &= R(\alpha,\beta,\gamma)\, v^u, \end{aligned} \tag{2.25}$$

where $R(\alpha,\beta,\gamma)$ is the rotation matrix given by:

$$R(\alpha,\beta,\gamma) = \tag{2.26}$$
$$\begin{pmatrix} \cos\gamma & \sin\gamma & 0 \\ -\sin\gamma & \cos\gamma & 0 \\ 0 & 0 & 1 \end{pmatrix} \begin{pmatrix} \cos\beta & 0 & -\sin\beta \\ 0 & 1 & 0 \\ \sin\beta & 0 & \cos\beta \end{pmatrix} \begin{pmatrix} \cos\alpha & \sin\alpha & 0 \\ -\sin\alpha & \cos\alpha & 0 \\ 0 & 0 & 1 \end{pmatrix}.$$

Indeed, we must carry out three rotations to go from the cosmic rest-frame to the computational frame. If the pulsars P_a and P_b in the cosmic rest-frame have polar

coordinates (θ_a, ϕ_a) and (θ_b, ϕ_b), respectively, the three angles of the rotations are:

$$\alpha = \phi_a \,, \tag{2.27a}$$

$$\beta = \theta_a \,, \tag{2.27b}$$

$$\tan\gamma = \frac{\sin\theta_b \sin(\phi_b - \phi_a)}{\cos\theta_a \sin\theta_b \cos(\phi_a - \phi_b) - \sin\theta_a \cos\theta_b} \,. \tag{2.27c}$$

The condition on γ has two solutions within the range [0,2π] and we choose the one that gives a positive x' coordinate in the computational frame for P_b.

Having calculated the relevant angles we can apply these to the rotation of spherical harmonics, where we know from Eq. (4.260) in Arfken [1985]:

$$Y_l^m(\hat{\Omega}') = \sum_{k=-l}^{l} D^l_{km}(\alpha, \beta, \gamma) Y_l^k(\hat{\Omega}), \tag{2.28}$$

and

$$Y_l^m(\hat{\Omega}) = \sum_{k=-l}^{l} \left[D^l_{mk}(\alpha, \beta, \gamma)\right]^* Y_l^k(\hat{\Omega}'), \tag{2.29}$$

where equations (2.28) and (2.29) rotate from the computational frame into the cosmic rest-frame, and back to the computational frame, respectively. The matrix $D^l_{mk}(\alpha, \beta, \gamma)$ is given by Eq. (4.12) in Rose [1957]

$$D^l_{mk}(\alpha, \beta, \gamma) = e^{-im\alpha} d^l_{mk}(\beta) e^{-ik\gamma} \,, \tag{2.30}$$

and for $m \geq k$

$$
\begin{aligned}
d^l_{mk}(\beta) &= \left[\frac{(l-k)!(l+m)!}{(l+k)!(l-m)!}\right]^{1/2} \frac{(\cos\frac{\beta}{2})^{2l+k-m}(-\sin\frac{\beta}{2})^{m-k}}{(m-k)!} \\
&\times \; {}_2F_1\left(m-l,-k-l;m-k+1;-\tan^2\frac{\beta}{2}\right), \qquad (2.31)
\end{aligned}
$$

where ${}_2F_1$ is the hypergeometric Gaussian function. For $m < k$, d^l_{mk} can be derived from the unitary property, and yields

$$
d^l_{mk}(\beta) = d^l_{km}(-\beta) = (-1)^{m-k} d^l_{km}(\beta)\,, \qquad (2.32)
$$

as in Eq. (4.15) in Rose [1957]. We also note that the $d^l_{mk}(\beta)$'s are real. Since ${}^{(ab)}\Gamma^m_l$ in Eq. (2.20) is a function of Y^m_l, we can now write the generalized overlap reduction function in the cosmic rest-frame as

$$
{}^{(ab)}\Gamma^m_l(f) = \sum_{k=-l}^{l} [D^l_{mk}(\alpha,\beta,\gamma)]^* \Gamma'^k_l(f), \qquad (2.33)
$$

where ${}^{(ab)}\Gamma'^m_l(f)$ (primed) is the generalized overlap reduction function in the computational frame.

2.4.2 Generalized overlap reduction functions in the computational frame

In order to compute the generalized overlap reduction function in the cosmic rest-frame, Eq. (2.20) or (2.24), one needs to compute the relevant function in the computational frame then rotate it via Eq. (2.33) using the matrix (2.30). Here we compute the generalized overlap reduction functions in the computational

frame. For ease of notation, we drop the primes, but it understood that in this section all the analysis is done in the primed, computational frame.

The spherical harmonic function $Y_l^m(\theta,\phi)$ of order m and degree l, $0 \leq m \leq l$ is defined as

$$\begin{aligned} Y_l^m(\theta,\phi) &= \sqrt{\frac{(2l+1)}{4\pi}\frac{(l-m)!}{(l+m)!}}P_l^m(\cos\theta)e^{im\phi}, &(2.34)\\ &= N_l^m P_l^m(\cos\theta)e^{im\phi}, &(2.35)\end{aligned}$$

where $0 \leq \theta \leq \pi$ is the azimuthal angle and $0 \leq \phi \leq 2\pi$ is the polar angle and the $P_l^m(\cos\theta)$ are the associated Legendre polynomials

$$\begin{aligned} P_l^m(x) &= \frac{(-1)^m}{2^l l!}(1-x^2)^{m/2}\frac{d^{l+m}}{dx^{l+m}}(x^2-1)^l\,, &(2.36a)\\ P_l^{-m}(x) &= (-1)^m\frac{(l-m)!}{(l+m)!}P_l^m(x)\,, &(2.36b)\end{aligned}$$

and

$$N_l^m = \sqrt{\frac{(2l+1)}{4\pi}\frac{(l-m)!}{(l+m)!}}, \tag{2.37}$$

is the normalization. The Hellings and Downs curve – or equivalently the overlap reduction function for an isotropic background – can be derived (up to a normalization constant) setting $l = m = 0$, *i.e.* $Y_0^0 = 1/\sqrt{4\pi}$.

For each pair of pulsars, the computational frame is defined by the geometry given in Eq (1.167), and in this reference frame Eq. (2.22) reduces to

$${}^{(ab)}\Gamma_l^m = (1+\delta_{ab})\int_{S^2} d\hat{\Omega}\, Y_l^m(\hat{\Omega})F_a^+(\hat{\Omega})F_b^+(\hat{\Omega}). \tag{2.38}$$

With this choice of frame, the generalized overlap reduction functions can

be easily computed. It is worth pointing out that *in this frame* the Γ_l^m's are real $\forall l\,, m$, and therefore $\Gamma_l^{-m} = (-1)^m \Gamma_l^m$ since $Y_l^{-m} = (-1)^m \left(Y_l^m\right)^*$, where the star here denotes the complex conjugate. One then need only take into account the transformation properties of the associated Legendre polynomials defined in Eq. (2.36).

In Appendix A.1 we provide comprehensive details of the derivations, whereas here we will just show the main results. For the case $l = m = 0$, Eq. (2.38), we obtain the overlap reduction function for the case of an isotropic background, which was derived in Eq (1.179), up to a multiplicative factor $4\sqrt{\pi}/3$. In fact the Hellings and Downs curve is normalized in such a way that is unity when one considers the auto-correlation of the timing residuals form the same pulsar ($a = b$ and therefore $\zeta = 0$). Note that for the isotropic case the rotation from the computational frame into the cosmic frame has no effect.

More generally, it is rather straightforward to compute analytical expressions for the case of a dipole ($l = 1$) anisotropy. In this case the generalized overlap reduction functions in the computational frame read (cf. Appendix A.1.2):

$$ {}^{(ab)}\Gamma_1^{-1} = -\frac{1}{2}\sqrt{\frac{\pi}{6}} \sin\zeta \left\{1 + 3(1-\cos\zeta)\left[1 + \frac{4}{(1+\cos\zeta)} \ln\left(\sin\frac{\zeta}{2}\right)\right]\right\}(1+\delta_{ab}), \tag{2.39a} $$

$$ {}^{(ab)}\Gamma_1^{0} = -\frac{1}{2}\sqrt{\frac{\pi}{3}} \left\{(1+\cos\zeta) + 3(1-\cos\zeta)\left[(1+\cos\zeta) + 4\ln\left(\sin\frac{\zeta}{2}\right)\right]\right\}(1+\delta_{ab}), \tag{2.39b} $$

$$ {}^{(ab)}\Gamma_1^{1} = -{}^{(ab)}\Gamma_1^{-1}\,, \tag{2.39c} $$

and are shown in Figure 2.2(b). The generalized functions for $m = \pm 1$ satisfy $\Gamma_1^{-1} = -\Gamma_1^1$, since m is odd.

Eq. (2.39) are equivalent to the result obtained in Anholm et al. [2009], where the dipole overlap reduction function is derived for a dipole in the direction:

$$\hat{D} = (\sin\alpha_a \cos\eta, \sin\alpha_a \sin\eta, \cos\alpha_a)\,, \tag{2.40}$$

where

$$\hat{D}\cdot\hat{p}_a = \cos\alpha_a, \qquad \hat{D}\cdot\hat{p}_b = \cos\alpha_b, \tag{2.41}$$

and so

$$\hat{D}\cdot\hat{p}_b = \cos\alpha_a\cos\zeta + \sin\alpha_a\sin\zeta\cos\eta. \tag{2.42}$$

In this case the function that describes the angular distribution in the sky is $P(\hat{\Omega}) = \hat{D}\cdot\hat{\Omega}$, therefore :

$$P(\hat{\Omega}) \;=\; \cos\alpha_a\cos\theta + \sin\alpha_a\sin\theta\cos(\phi-\eta). \tag{2.43}$$

Following our approach we can decompose $P(\hat{\Omega})$ onto the basis of spherical harmonic functions and we obtain:

$$\begin{aligned} P(\hat{\Omega}) &= 2\sqrt{\frac{\pi}{3}}\cos\alpha_a Y_1^0(\hat{\Omega}) - \sqrt{\frac{2\pi}{3}}(\sin\alpha_a\cos\eta - i\sin\alpha_a\sin\eta)\,Y_1^1(\hat{\Omega}) \\ &+ \sqrt{\frac{2\pi}{3}}\,(\sin\alpha_a\cos\eta + i\sin\alpha_a\sin\eta)\,Y_1^{-1}(\hat{\Omega}) \\ &= 2\sqrt{\frac{\pi}{3}}\left\{\cos\alpha_a Y_{10}(\hat{\Omega}) - \sin\alpha_a\cos\eta Y_{11}(\hat{\Omega}) + \sin\alpha_a\sin\eta Y_{11}(\hat{\Omega})\right\} \end{aligned} \tag{2.44}$$

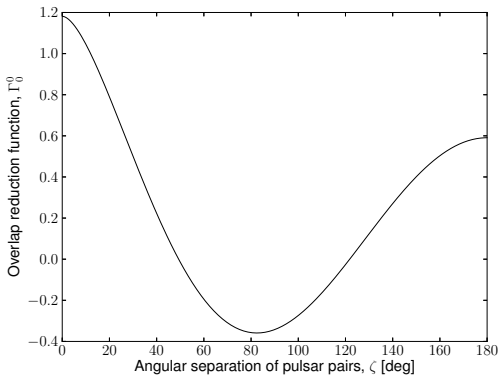

(a) Monopole ($l = 0$)

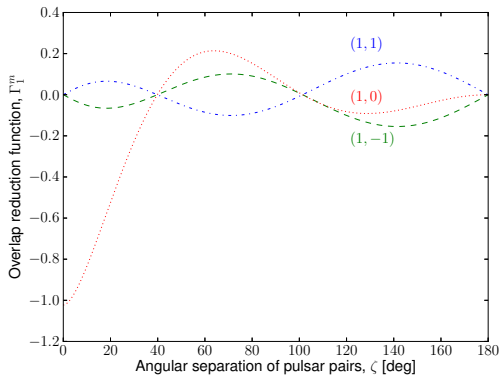

(b) Dipole ($l = 1$)

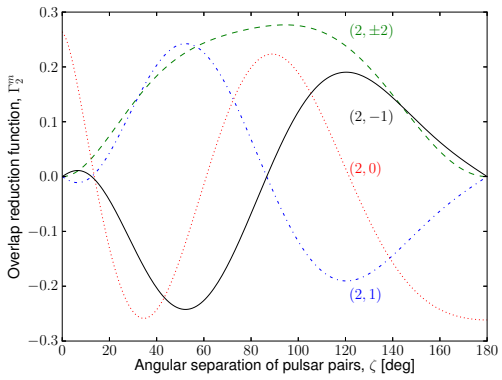

(c) Quadrupole ($l = 2$)

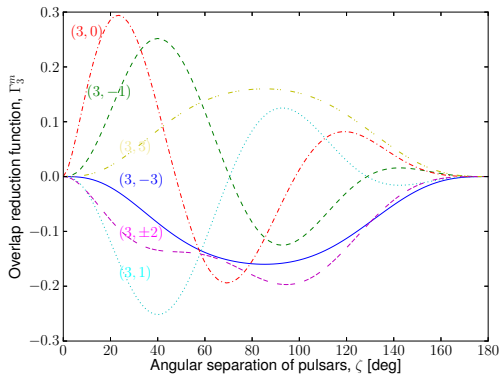

(d) Octupole ($l = 3$)

Figure 2.2: The Earth-term only, generalized overlap reduction functions Γ_l^m in the computational frame for $l = 0\,, 1\,, 2\,, 3$ as a function of the angular separation of pulsar pairs. In the computational frame, $\Gamma_l^{-m} = (-1)^m \Gamma_l^m$. For the $l = 0$ case, Γ_0^0 is the Hellings and Downs curve up to the multiplicative constant $4\sqrt{\pi}/3$.

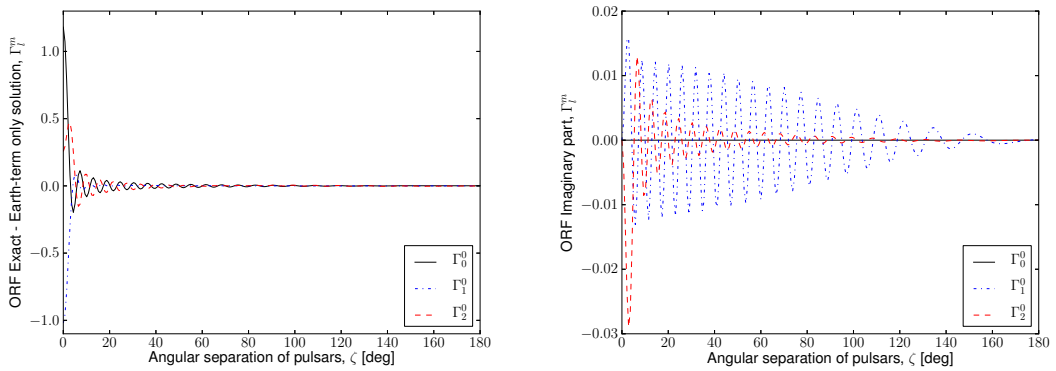

(a) Difference of real parts

(b) Imaginary part

Figure 2.3: Generalized overlap reduction functions (ORF) with the pulsar term. (a) The difference between the exact solution and the Earth term-only solution for $fL = 10$ in the computational frame. These oscillations are already quite small for $\zeta = 60°$ and rapidly converge to zero for larger values of ζ. (b) The value of the complex component of the pulsar term for $fL = 10$ in the computational frame. Recall that the Earth-term only solution is always real, but introducing the pulsar term gives rise to complex-valued overlap reduction functions, even in the computational frame. Notice that these oscillations induced by the pulsar term are at least an order of magnitude smaller than the real part but do not, however, converge as quickly as the real component. The Γ_0^0 function has no imaginary component.

The dipole overlap reduction function derived in Anholm et al. [2009] (see Eq. (C23) in Appendix 2), can therefore be written in terms of a linear combination of the generalized overlap reduction functions ${}^{ab}\Gamma_1^{-1}$, ${}^{ab}\Gamma_1^0$ and ${}^{ab}\Gamma_1^1$, or the analogous real expressions, and the actual values of the coefficients c_1^{-1}, c_1^0 and c_1^1 returned by the analysis provide the direction of the dipole moment that describes the radiation.

It is sufficiently straightforward to derive analytical expressions for the generalized overlap reduction function describing a quadrupole ($l = 2$) anisotropy (cf. Appendix A.1.3):

$$^{(ab)}\Gamma_2^{-2} = \Gamma_2^2,$$

$$^{(ab)}\Gamma_2^{-1} = -\Gamma_2^1,$$

$$^{(ab)}\Gamma_2^0 = \frac{1}{3}\sqrt{\frac{\pi}{5}}\left\{\cos\zeta + \frac{15}{4}(1-\cos\zeta)\left[(1+\cos\zeta)(\cos\zeta+3) + 8\ln\left(\sin\frac{\zeta}{2}\right)\right]\right\}(1+\delta_{ab}), \tag{2.45a}$$

$$^{(ab)}\Gamma_2^1 = \frac{1}{4}\sqrt{\frac{2\pi}{15}}\sin\zeta\left\{5\cos^2\zeta + 15\cos\zeta - 21 - 60\frac{(1-\cos\zeta)}{(1+\cos\zeta)}\ln\left(\sin\frac{\zeta}{2}\right)\right\}(1+\delta_{ab}), \tag{2.45b}$$

$$^{(ab)}\Gamma_2^2 = -\frac{1}{4}\sqrt{\frac{5\pi}{6}}\frac{(1-\cos\zeta)}{(1+\cos\zeta)}\left[(1+\cos\zeta)(\cos^2\zeta + 4\cos\zeta - 9) - 24(1-\cos\zeta)\ln\left(\sin\frac{\zeta}{2}\right)\right] \times (1+\delta_{ab}), \tag{2.45c}$$

which are shown in Figure 2.2(c). For higher order l the integrals become sufficiently complex that we have not tried to derive analytical expressions. It is however easy to derive numerically the results, and an example for $l = 3$ is shown in Figure 2.2(d).

2.4.3 The pulsar term for generalised overlap reduction functions

In our analysis we have approximated the generalized overlap reduction function, Eq. (2.20), as (2.22) because current PTA analysis operates in the regime in which $fL \gg 1$. In other words, we have only considered the Earth-term contribution of the background in correlating data from different pulsars. At any given frequency, $\kappa_{ab}(f, \hat{\Omega})$ introduces rapid oscillations that depend on the distance and location to

the pulsars and the frequency of the gravitational radiation. When one integrates over the whole sky, all the possible directions of propagation of the background, the oscillations average to 1. Physically, this is a consequence of the fact that PTAs operate in the short-wavelength regime, that is the gravitational wavelength is much smaller than the distance to the pulsars.

In Anholm et al. [2009] it was shown that Eq. (2.22) is an excellent approximation for $fL \gg 1$ for the isotropic (or monopole) case. The same is true for all the higher order moments l, and here we provide some examples. Let us consider $l = 0, 1, 2$ and the generalized overlap reduction functions which are non-zero at zero angular separation, that is Γ_0^0, Γ_1^0, and Γ_2^0. The functions which are zero at $\zeta = 0$ have a very weak pulsar term dependence and are therefore not considered here. We will also make the assumption that the distance to both pulsars is the same.

The Earth term is always real for overlap reduction functions calculated in the computational frame. By introducing the pulsar term, the overlap reduction functions are in general complex; in fact, only Γ_l^0 is real for all l. The pulsar term adds oscillations which are at most twice the value of the Earth term for $\zeta = 0$ and are quickly attenuated as ζ increases. These oscillations can be seen in Figure 2.3(a), which shows the difference between the exact solutions of Eq. (2.20) for Γ_l^0, where $l = 0, 1, 2$, and the Earth-term only solutions Eq. (2.20), where we approximate $\kappa_{ab} \sim 1$. Note that these oscillations have almost converged to zero at $\zeta = 60°$ for $fL = 10$. For larger values of fL, the pulsar term oscillations, such as the ones seen in Figure 2.3(a), become tighter and move to the left.

The imaginary part behaves in a similar oscillatory fashion. The oscillations in Figure 2.3(b) are at least an order of magnitude smaller than those of the real part,

and can be thought of as a small change in phase. These oscillations converge much more slowly and in the case of Γ_1^0 they go to zero only at considerable angular separations.

2.5 Conclusions

We have considered how an arbitrary level of anisotropy in the GW energy of a stochastic background affects the correlations of the data from pulsars in PTAs and the implications for analysis. In fact the characterization of the GW power at different angular scales carries important information about the signal.

We have considered the relevant case of the background from SMBHB systems. We have estimated that the level of anisotropy is small, as one would expect, and likely undetectable at present/near future sensitivity in the low-frequency region, where PTAs have optimal sensitivity. The level of anisotropy increases as one goes to higher frequencies, due to the fact that the effective number of sources which dominate the signal decreases. Anisotropy may therefore become important in a regime in which the sources are still individually unresolvable (with the exception of possibly a few), but the total number may not be sufficiently large to generate a smooth, diffuse background. This raises interesting questions regarding what is the optimal analysis strategy in this regime, which needs to be addressed. Sesana is currently carrying out a detailed study of the anisotropy level that can be expected from astrophysically realistic populations of SMBHBs.

We have then shown that the present analysis techniques to search for isotropic stochastic backgrounds can be generalized to arbitrary levels of anisotropy by decomposing the angular distribution of the GW power on the sky into multipole

moments. We have introduced the generalized overlap reduction functions Γ_l^m that describe the correlation from the timing residuals from two pulsars for every (l, m) anisotropy multipole. We have provided ready to use expressions for the Γ_l^m's that can be used in the analysis of the data of the PTAs currently in operation and that are an essential element of an analysis pipeline aimed at this type of signal. A Bayesian analysis approach based on the formalism that we have presented has been developed by Taylor and Gair [2013]. It is also important to note that some data analysis methods currently use "compression" algorithms to speed up the processing of the data, see van Haasteren [2013]. As a result of this, the high frequency sensitivity is compromised. This is the frequency band where anisotropy is more significant, and therefore future development of data analysis techniques will need to take this into account.

2. CHARACTERIZING GRAVITATIONAL WAVE STOCHASTIC BACKGROUND ANISOTROPY WITH PULSAR TIMING ARRAYS

Chapter 3

THE EFFECT OF SMALL PULSAR DISTANCE VARIATIONS IN STOCHASTIC GW BACKGROUND SEARCHES WITH PTAs

This chapter is currently being prepared for publication in Physical Review D as "C. M. F. Mingarelli and T. Sidery, The effect of small pulsar distance variations in stochastic gravitational wave background searches with Pulsar Timing Arrays". I calculated the magnitude of the overlap reduction functions presented here, the Taylor series expansion, wrote and executed all the numerical codes used to make Table 3.1 and all the figures except for the contour plots. I wrote the draft of this paper, and all the text included here.

3.1 Introduction

Einstein's theory of gravity has been challenged and tested for almost a century. Many aspects of the theory have been exhaustively tested but the gravitational wave (GW) prediction remains extremely challenging to verify directly, although indirect evidence supports their existence BICEP2 Collaboration et al. [2014]; Hulse and Taylor [1975]; Kramer and Wex [2009]; Kramer et al. [2006]; Taylor and Weisberg [1982]. To this end, Hellings and Downs [1983], who built on ideas proposed by Detweiler [1979]; Estabrook and Wahlquist [1975]; Sazhin [1978], put forward the idea of a Pulsar Timing Array (PTA). A PTA is a type of GW detector which uses one or more radio telescopes to regularly monitor a selection of ultra-stable millisecond pulsars: the propagation time of radio waves from each pulsar to the Earth is affected by the GW-induced space-time perturbations along its path. The difference between the expected and actual time-of-arrival of the radio pulses, called the timing residual, carries information about the GWs which can be extracted by correlating the residuals from pulsar pairs in the PTA. The signal received at the Earth is in fact a linear combination of the GW perturbation at the time when the GW transits at the pulsar, the so-called "pulsar term", and then when the GW passes the Earth, called the "Earth term".

The sensitivity of a PTA to gravitational radiation is set by the total observation time, normally 10 years, yielding a lower frequency bound of $1/10$ $\mathrm{yr}^{-1} \sim 10^{-9}$ Hz. The cadence of observation, typically a few months, gives an upper frequency bound of $\sim 10^{-7}$ Hz. A promising class of sources in this frequency band are supermassive black hole binary (SMBHB) systems with masses in the range of $\sim 10^7 - 10^9\ M_\odot$ during their slow, adiabatic inspiral phase, cf. Jaffe

and Backer [2003]; Rajagopal and Romani [1995]; Sesana [2012]; Sesana et al. [2008, 2009]; Wen et al. [2011]; Wyithe and Loeb [2003]. Other more speculative sources from the early Universe, including cosmic strings Kuroyanagi et al. [2013]; Pshirkov and Tuntsov [2010]; Sanidas et al. [2012] and relic GWs, see e.g. Zhao [2011], are also expected to be found in this frequency band. Searches of increasing sensitivity are currently ongoing in the European PTA (EPTA), e.g. Ferdman et al. [2010], the Parkes PTA, e.g.Verbiest et al. [2010], and the North American Nanohertz Gravitational Wave Observatory (NANOGrav), e.g. Jenet et al. [2009], which together form the International PTA (IPTA), e.g. Hobbs et al. [2010].

In stochastic GW background background searches, the cross-correlated timing residuals enter into the likelihood function through the evaluation of the overlap reduction function (ORF)– a dimensionless function which quantifies the response of the pulsar pairs to the stochastic GW background. The ORF is in turn a function of the frequency of the GW background, the distance to each pulsar, and the angular separation of each pulsar pair and is usually normalized such that pulsar pairs with zero angular separation have a maximal detector response of 1 for an isotropic distribution of GW energy density.

Current searches assume that many GW wavelengths, or radiation wavelengths, separate the pulsars from the Earth and from each other. The number of radiation wavelengths is calculated by taking the product of the GW background frequency f and the distance to the pulsar L. When this product is large, $fL \gg 1$, the pulsar term is only evaluated for the autocorrelation term. This is called the "short-wavelength approximation", and is used in all stochastic GW background searches to date. However, as PTAs become more densely populated

with millisecond pulsars, either by dedicated pulsar searches with current radio telescopes (e.g. Barr et al. [2013]; Keith et al. [2010]; Stovall et al. [2013]) or by future radio telescopes currently under development such as the Five Hundred Meter Aperture Spherical Radio Telescope (FAST, e.g. Nan [2008]) and/or the Square Kilometre Array (SKA, e.g. Lazio [2013]), pulsars in a PTA may no longer lie many radiation wavelengths apart. Moreover, Sesana's new models of the stochastic GW background – generated by the cosmic population of SMBHBs which include additional environmental effects, such as eccentricity at the moment of pairing– predict an ultra-low frequency GW background, $f < 3 \times 10^{-9}$, see Sesana [2013]. A low frequency GW background paired with nearby pulsars such as J0437−4715, which is only 160 pc away (see ATNF [2014]), yield a minimum fL value of order 10. Hence, in a low frequency GW background, J0437−4715 is 10 radiation wavelengths away from the Earth.

In this paper we investigate the importance of the additional correlated phase terms arising from the GW transiting at the pulsar– modelled by the pulsar term– by systematically exploring how the angular separation and distance variations of pulsars in a PTA affect the ORF in stochastic GW background searches. The correlated phase changes introduce imaginary components into the ORFs. Therefore, we investigate the magnitude of each ORF instead of separately examining the real and imaginary parts. For the purposes of this study, we restrict ourselves to the isotropic, dipole and quadrupole ORFs, derived in Mingarelli et al. [2013]. Pulsars from the IPTA mock data challenge are used throughout to give concrete examples of how and when additional phase terms should be included in the ORFs.

An overview of stochastic GW backgrounds is given in Sec 1.4 and an in-

troduction to the PTA ORF can be found in Sec 1.7. In Sec 3.2 we illustrate how relaxing the assumption that all the pulsars in a PTA are at the same distance from the Earth affects the magnitude of the ORFs. We also calculate the strong pulsar term region around a pulsar, where substantial contributions from the pulsar term may be present. In Sec 3.3, we approximate the pulsar term for pulsar pairs separated by a sufficiently small angle as to have significant pulsar term contributions. We show that this approximation captures the most important behaviour of the pulsar term. For completeness, we further investigate the behaviour of the pulsar term when a pulsar is within one radiation wavelength from the Earth in Sec 3.4. Moreover, we give an exact solution to a piece of the ORF which includes the pulsar term, in an effort to accurately compute the autocorrelation term. Conclusions are presented in Sec 3.5.

3.2 Correlated phase changes from small variations in pulsar distances

Consider the behaviour of the function $\kappa_{ab}(f, \hat{\Omega})$, defined in Eq. (1.165) and present in Eq. (1.164), which introduces the frequency and distance-dependence of the ORFs. When correlating the timing residuals from pulsars in a PTA, one can think of $\kappa_{ab}(f, \hat{\Omega})$ as the term which encodes the information about both the pulsar terms. Assuming $L_a = L_b = L$, the typical scale of $\kappa_{ab}(f, \hat{\Omega})$ for the current pulsar population and PTA sensitivity is:

$$fL(1 + \hat{\Omega} \cdot \hat{p}) = 10^3 \left(\frac{f}{10^{-8}\,\mathrm{Hz}} \right) \left(\frac{L}{1\,\mathrm{kpc}} \right) (1 + \hat{\Omega} \cdot \hat{p}). \tag{3.1}$$

Large values of fL introduce rapid oscillations to the ORF that depend on the distance and location of the pulsars, as well as the frequency of the GW background. Inspecting Eq (1.165), one can see that the pulsar term oscillations are produced by the nested cosines (which give rise to Bessel Functions) that appear when one expands the square brackets of Eq (1.165). For most astrophysically relevant situations to date $fL \gg 1$, therefore, when one computes the integral in Eq. (1.164) the frequency dependent contributions to the integral rapidly average out to zero as the angle between the pulsar pairs increases, details in Anholm et al. [2009]; Mingarelli et al. [2013]. In the $fL \gg 1$ case, the ORF Eq. (1.164) is therefore well approximated by Eq (2.22). Note that the approximation (2.22) is equivalent to considering the pulsar term for the autocorrelation only (i.e. when $a = b$), and is otherwise an Earth term only expression.

3.2.1 Low frequency GW backgrounds

Oscillations introduced to the ORF by the pulsar term are very tight, and very small for pulsars at ~ 1 kpc in GW backgrounds of $f \sim 10^{-8}$ Hz, cf. Eq (3.1) or Anholm et al. [2009]; Mingarelli et al. [2013]; Taylor and Gair [2013]. However, nearby pulsars such as J0437−4715, J1856−3754 and J2144−3933 lie at 160 pc from the Earth, see ATNF [2014]. Nearby pulsars in a low frequency GW background, generated for example by eccentric SMBHBs, detailed in Sesana [2013], would lie at ~ 10 radiation wavelengths from the Earth:

$$fL(1 + \hat{\Omega} \cdot \hat{p}) = 10 \left(\frac{f}{10^{-9}\,\mathrm{Hz}} \right) \left(\frac{L}{100\,\mathrm{pc}} \right) (1 + \hat{\Omega} \cdot \hat{p}). \tag{3.2}$$

We now explore how relaxing the assumption that all pulsars in a PTA are

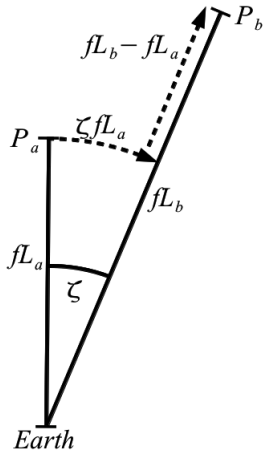

Figure 3.1: Geometry of pulsar pairs in the "strong pulsar term regime". Here P_x, where $x = a, b$, is pulsar x, L_x is the distance to pulsar x from Earth and ζ is the angular separation of the pulsar pairs. The dimensionless product fL_x is the number of radiation wavelengths from the Earth to pulsar x. The geometry indicates two possible movements: pulsar b is moved radially by ζfL_a radiation wavelengths from a, or pulsar b is moved further away from a by an amount $fL_b - fL_a$, along the z-axis.

at the same distance from the Earth[1], i.e. $L_a = L_b$, affects the ORFs for nearby pulsars in the current low frequency limit of PTAs. Since we have a concrete lower bound of $fL = 10$, we fix the dimensionless product $fL_a = 10$ and vary fL_b from 10 to 14. Larger values of fL_b were computed, up to $fL_b = 20$ for all the ORFs, however the oscillations converged to zero increasingly rapidly as fL increased. Therefore these curves were omitted from Figs 3.2 and 3.3. The analysis was also carried out for fL_b fixed varying fL_a with analogous results, and is therefore not reported here.

We first study the magnitude of the isotropic ORF ${}^{(ab)}\Gamma_0^0(fL, \zeta)$, which in the short wavelength approximation and with normalization $\beta = 3/(4\sqrt{\pi})$ is the Hellings and Downs [1983] curve. The normalization ensures that the Hellings

[1]For data analysis purposes, pulsar TOAs are shifted to the solar system barycentre. We refer to distances from the Earth for simplicity and clarity.

and Downs curve is identically equal to 1 for zero angular separation (the auto-correlation term). Since this normalization is applied to the isotropic ORF, it is also applied to the dipole and quadrupole ORFs for consistency. The analysis continues with the study of the dipole, $l = 1$, $m = 0, 1$ and quadrupole $l = 2$, $m = 0, 1, 2$ ORFs for completeness, though as indicated in Eq (2.18), we expect the stochastic GW background to be largely isotropic at low frequencies.

The $-m$ values of the ORFs are not explicitly shown, since in our reference frame, described in Eq (1.167),

$$^{(ab)}\Gamma_l^m(fL, \zeta) = (-1)^{m\,(ab)}\Gamma_l^m(fL, \zeta)\,. \tag{3.3}$$

One may be surprised that all the ORFs are evaluated, since previous studies by Mingarelli et al. [2013] indicated that the $m = 0$ ORFs were the most sensitive to the pulsar term. That study, however, only considered pulsars at the same distance from the Earth. Small pulsar-to-pulsar distance variations will introduce correlated phase changes which are important for all the ORFs, as we show in Figs 3.2, 3.3.

We probe the strong pulsar term regime– where the pulsars are separated by less than a few radiation wavelengths – by continuously moving pulsar b towards or away from pulsar a along the z-axis. This change in distance is given by $fL_b - fL_a$, as shown in Fig 3.1. Pulsar b is also moved radially away from a by an angle ζ, and therefore b lies at ζfL_a radiation wavelengths from a in this geometry. The effect of these continuous movements on the magnitude of the ORFs is shown in the contour plots in Figs 3.2, 3.3. The overall shape of the ORFs in the strong pulsar term regime is a function of the geometry of the

pulsars and how they are aligned with the GW energy density, which is in turn described by the standard spherical harmonics Y_l^m. A detailed explanation of the features seen in the contours in Figs 3.2 and 3.3 is given in Appendix B and the most significant differences between the complete ORF, Eq (1.164), and the Earth-term-only ORF, Eq (2.22), are highlighted in Table 3.1.

3.2.2 The Hellings and Downs curve

Firstly, we explore the behaviour of the isotropic overlap reduction function when the pulsars are separated from each other by a few radiation wavelengths, either radially or in the z-direction, cf. Fig 3.1. The contour plot Fig 3.2(b) complements Fig 3.2(a) as it shows the continuous displacement of pulsar b from pulsar a. We find that for a fixed pulsar a with $fL_a = 10$, the largest value of the ORF is achieved for $\zeta = 0$ and $fL_b - fL_a = 0$, see Table 3.1, as expected. Moreover, we find that the strongest pulsar term effects occur when pulsar b located less than a radiation wavelength away from a, with the strongest correlations occurring when pulsar b is less than half a radiation wavelength from a. The magnitude of the oscillations drops dramatically when pulsar b is moved one radiation wavelength away from pulsar a. Moreover, the peak of the oscillations moves to the right as fL_b increases, and the period of the oscillations increases. This behaviour is present in all the ORFs, cf. Table 3.1 and Figs 3.2, 3.3. Indeed, it is clear that as fL_b increases, the ORF converges to the Earth-term only solution, the solid (blue) line in Fig 3.2(a).

Our analysis of the isotropic ORF therefore indicates that the pulsar term only adds a significant additional piece to the standard, Earth-term only ORF

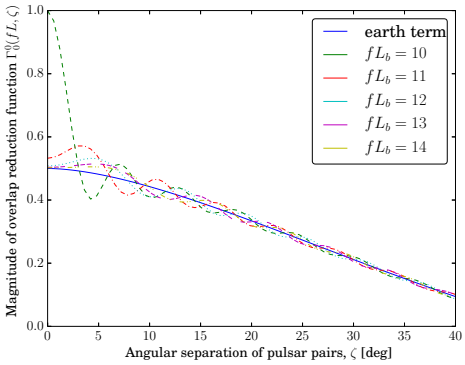

(a) Magnitude of the ${}^{(ab)}\Gamma^0_0(fL,\zeta)$ ORF

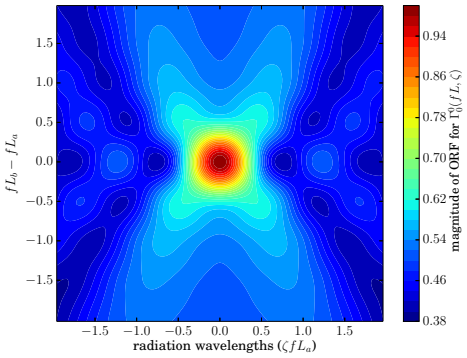

(b) Strong pulsar term regime of ${}^{(ab)}\Gamma^0_0(fL,\zeta)$.

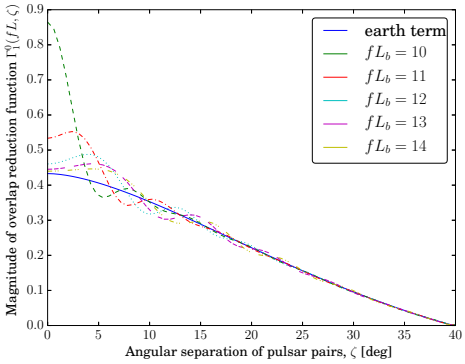

(c) Magnitude of dipole ${}^{(ab)}\Gamma^0_1(fL,\zeta)$ ORF

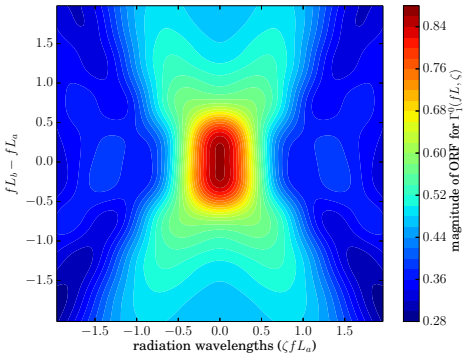

(d) Strong pulsar term regime of ${}^{(ab)}\Gamma^0_1(fL,\zeta)$

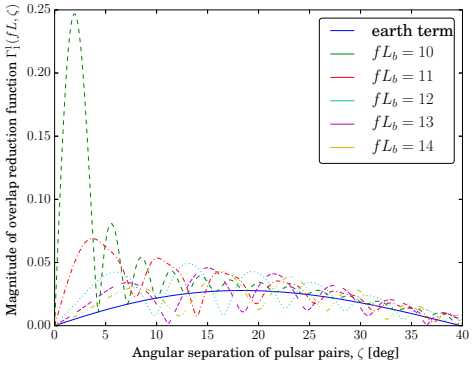

(e) Magnitude of the ${}^{(ab)}\Gamma^1_1(fL,\zeta)$ ORF

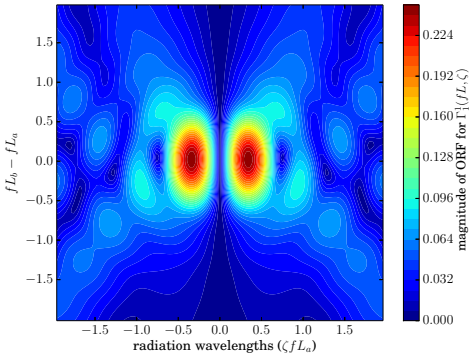

(f) Strong pulsar term regime of ${}^{(ab)}\Gamma^1_1(fL,\zeta)$

Figure 3.2: The effect of pulsar distance variations on the magnitude of the isotropic and dipole overlap reduction functions, with $fL_a = 10$ fixed. Panels on the left hand side are truncated at 40 degrees, as pulsar term oscillations rapidly converge to zero.

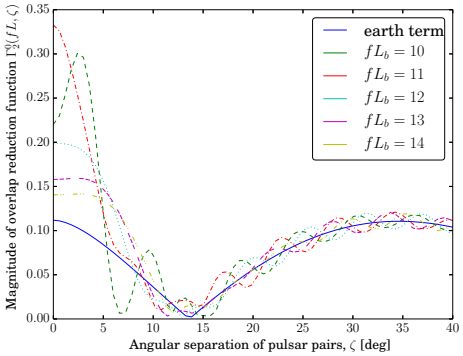

(a) Magnitude of the ${}^{(ab)}\Gamma_2^0(fL,\zeta)$ ORF

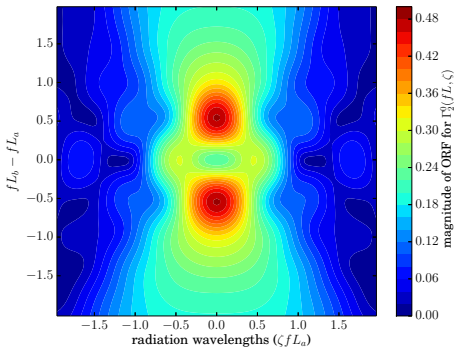

(b) Strong pulsar term regime of ${}^{(ab)}\Gamma_2^0(fL,\zeta)$

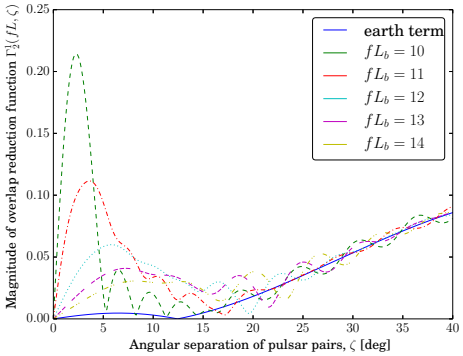

(c) Magnitude of the ${}^{(ab)}\Gamma_2^1(fL,\zeta)$ ORF

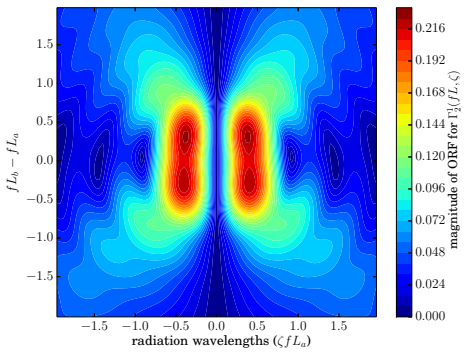

(d) Strong pulsar term regime of ${}^{(ab)}\Gamma_2^1(fL,\zeta)$

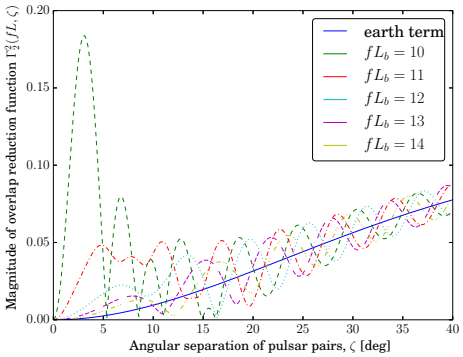

(e) Magnitude of the ${}^{(ab)}\Gamma_2^2(fL,\zeta)$ ORF

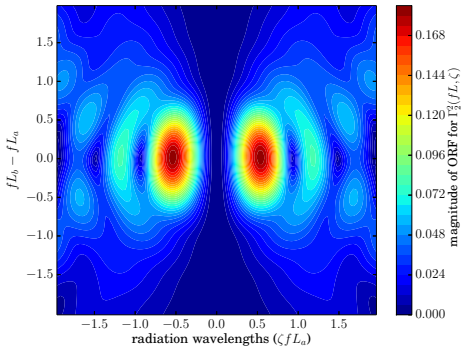

(f) Strong pulsar term regime of ${}^{(ab)}\Gamma_2^2(fL,\zeta)$

Figure 3.3: The effect of pulsar distance variations on the magnitude of the quadrupole overlap reduction functions, with $fL_a = 10$ fixed. Panels on the left hand side are truncated at 40 degrees since error bars on each point are expected to be of the order of $10-20\%$. Moreover it is clear that the pulsar term oscillations rapidly converge to zero. Note that the maximum value of some ORFs is achieved for small, but non-zero, angular separations between pulsar pairs.

for pulsars within 10 radiation wavelengths from the Earth, separated by no more than half a GW wavelength. This corresponds to a strong pulsar-term induced ORF response when $\zeta \leq 3^\circ$ in agreement with Fig 3.2(a), with $fL_b = 10$.

3.2.3 The dipole overlap reduction function

In Mingarelli et al. [2013], we claimed that out of the dipole ORFs, ${}^{(ab)}\Gamma_1^0$ is the most sensitive to the pulsar term, since it is the only dipole ORF with a non-zero value at zero angular separation. This claim was based on the assumption that the pulsars were equidistant from the Earth. Relaxing this assumption and including the pulsar term, we find that *all* of the dipole ORFs show strong pulsar term behaviour, when separated by less than a radiation wavelength. This behaviour is clearly shown in Figs 3.2(c), 3.2(d), 3.2(e), 3.2(f).

For the $\Gamma_1^0(fL, \zeta)$ ORF, the largest contribution from the pulsar term arises from the scenario where $fL_a = fL_b = 10$, seen in both Fig 3.2(c), 3.2(d). In Fig 3.2(c), one can see that by moving pulsar b one radiation wavelength to $fL_b = 11$, the dashed-dot (red) curve, the additional contribution of the pulsar term is negligible. As fL_b increases by one for each subsequent curve, it is clear that the pulsar term contribution converges to zero. Therefore the ORF becomes essentially an Earth-term only expression as the pulsars are separated by many radiation wavelengths. We then study the strong pulsar term regime of $\Gamma_1^0(fL, \zeta)$, Fig 3.2(d), using the geometry detailed in Fig 3.1 to draw a circle of influence around pulsar a. Here we find that the strong pulsar term region is extended in the $fL_b - fL_a$ direction, indicating that the pulsar term is important when pulsar b is up to one radiation wavelength away (in the z direction) from pulsar a. This

strong pulsar term range is twice that of the isotropic ORF in the z-direction, but in terms of radial radiation wavelengths, $\zeta f L_a$, the sensitivity is very similar to that of the isotropic ORF. The shape is due to a combination of geometric effects and the transverse nature of GWs, described in Appendix B.

For the $\Gamma_1^1(fL, \zeta)$ ORF, the largest contribution from the pulsar term arises from the scenario where $fL_a = fL_b$, as shown in Fig 3.2(f), but the maximum is achieved at a non-zero angular separation of $\zeta = 1.9°$. Note that the fractional difference between the full ORF and the Earth-term-only ORF at $\zeta = 1.9°$ is 49! This ORF also differs from the previous ones in that the relatively large oscillatory behaviour is present up to $\zeta \lesssim 20°$. Moving pulsar b one radiation wavelength to $fL_b = 11$– the dashed-dot (red) curve in Fig 3.2(e)– the additional contribution of the pulsar term is still remarkable, with its peak at $\zeta_{\max} = 3.5°$, and a fractional difference between the full and Earth-term only ORF of 7.

The strong pulsar term region is extended in the $fL_b - fL_a$ direction, as it was for $\Gamma_1^0(fL, \zeta)$, with the exception of having no response at $\zeta = 0$, see Fig 3.2(f). The peak is centered on $\zeta f L_a \sim 0.5$ and extends to $\zeta f L_a \sim 1$, which translates into important pulsars term features for pulsars separated by $0° < \zeta \lesssim 6°$, in agreement with Fig 3.2(e) and Table 3.1. The oscillations are slower to converge for this ORF, and therefore one may wish to include these additional correlated phase changes in stochastic GW background searches, up to $\zeta \sim 15°$ when $fL_b \sim 10 - 12$, see Fig 3.2(e).

ORF	fL_b	$\zeta_{\max}$	Full ORF	ET ORF	Frac Diff
Γ_0^0	10	0.0°	1.0	5.0×10^{-1}	1
	11	0.8°	5.7×10^{-1}	4.8×10^{-1}	0.2
	12	1.1°	5.2×10^{-1}	4.8×10^{-1}	0.1
Γ_1^0	10	0.0°	8.6×10^{-1}	4.3×10^{-3}	1
	11	0.5°	5.5×10^{-1}	4.2×10^{-3}	0.3
	12	1.1°	4.8×10^{-1}	4.1×10^{-1}	0.2
Γ_1^1	10	1.9°	2.5×10^{-1}	4.9×10^{-3}	49
	11	3.5°	6.9×10^{-2}	9.0×10^{-3}	7
	12	5.5°	4.2×10^{-2}	1.4×10^{-2}	2
Γ_2^0	10	2.4°	3.0×10^{-1}	1.0×10^{-1}	2
	11	0.0°	3.3×10^{-1}	1.1×10^{-1}	2
	12	2.4°	1.9×10^{-1}	1.0×10^{-1}	0.9
Γ_2^1	10	2.3°	2.1×10^{-1}	2.5×10^{-3}	84
	11	3.6°	1.1×10^{-2}	3.6×10^{-3}	30
	12	5.6°	6.0×10^{-2}	4.6×10^{-3}	12
Γ_2^2	10	3.1°	1.8×10^{-1}	9.7×10^{-4}	188
	11	4.7°	4.8×10^{-2}	2.2×10^{-3}	21
	12	13.2°	4.2×10^{-2}	1.6×10^{-2}	2

Table 3.1: Here we list the largest fractional difference of the magnitude of the full (F) and Earth-term-only ORFs (ET), see Figs 3.2, 3.3, and report the angle at which this maximum value was achieved, $\zeta_{\max}$. The value of fL_a is fixed at 10. The largest value of the full ORF was calculated as follows: we subtract the ET solution from the full ORF, and find the maximum value of the remaining pulsar term contribution, and the angle where this maximum was achieved. We then evaluate the full and ET ORFs at $\zeta_{\max}$ and calculate the fractional difference as $|\mathrm{F} - \mathrm{ET}|/\mathrm{ET}$. This is rounded to the nearest integer, unless it is less than one.

3.2.4 The quadrupole overlap reduction function

Here we examine how varying the distances to pulsars in a PTA affects the behaviour of the $l = 2$, $m = 0, 1, 2$ quadrupole ORFs ${}^{(ab)}\Gamma_2^m(fL, \zeta)$. The key figures for this analysis are given in Fig 3.3. As before, we fix $fL_a = 10$ and vary fL_b from 10 to 14. The values of fL_b up to 20, however as before, these additional curves converged to zero very quickly, providing little insight. The roles of fL_b and fL_a were switched and the analysis carried out again, yielding nearly identical results.

Starting with the ${}^{(ab)}\Gamma_2^0(fL, \zeta)$ ORF, Fig 3.3(a), the two main curves of interest are the $fL_b = 10$ and $fL_b = 11$ curves. This ORF displays a feature which was previously seen in the $\Gamma_1^1(fL, \zeta)$– the maximum value of the ORF for equidistant pulsars occurs when $\zeta \neq 0$. Although the ORF is twice the Earth-term for $fL_a = fL_b = 10$ at $\zeta = 0$, as expected, the maximum value of the ORF is at 2.4°, where it is triple the value of the Earth term, with a fractional difference of 2. It is also interesting to note that by moving pulsar b a radiation wavelength away from pulsar a, corresponding to $fL_b = 11$, the autocorrelation term is also three times larger than the Earth term, see Table 3.1. Moreover, for $fL_b = 11$, the autocorrelation term is *larger* than the $fL_a = fL_b = 10$ case.

The full $m = 1$ and $m = 2$ quadrupole ORFs also feature a remarkable departure from the Earth-term only expression for pulsars separated by less than a radiation wavelength, and converge more slowly to the Earth-term-only ORF (solid blue line), Figs 3.3(c), 3.3(d), 3.3(e), 3.3(f). The largest fractional difference between the full and Earth-term ORFs occurs in the ${}^{(ab)}\Gamma_2^0(fL, \zeta)$ ORF for $fL_a = fL_b = 10$ at $\zeta = 3.1°$: here the maximum fractional difference is 188!

It is clear that in general the largest value for the ORFs is achieved when the pulsars are equidistant. However, pulsars up to 2 radiation wavelengths away (denoted below as $\lambda_{\text{number}} = 2$), which in terms of physical distance scales as

$$L_b = 17 \left[\left(\frac{\lambda_{\text{number}}}{2} \right) \left(\frac{f}{10^{-9}\ \text{Hz}} \right)^{-1} + \left(\frac{L_a}{100\ \text{pc}} \right) \right] \text{pc}, \tag{3.4}$$

could contribute additional correlated phase terms to the ORF which may need to be modelled.

3.3 Small angle approximation

In Sec 3.2 we showed that the pulsar term is important to include in the evaluation of most of the ORFs if the pulsars are separated by less than a radiation wavelength, see Table 3.1 for details. Motivated by the possibility of having pulsars separated by such a small angle, we give a small angle approximation of the pulsar term for the ORFs, up to $\mathcal{O}(\zeta^2)$ which closely follows the true behaviour of the complete isotropic ORF. Since the pulsar term, Eq (1.165), is not a function of angular distribution of the GW energy density, this approximation can be used for all PTA ORFs, however it is advised to extend the approximation to $\mathcal{O}(\zeta^3)$ for $l \geq 1$. We show how this approximation compares to the full isotropic ORF for $fL_{a=b} = 10, 51.2, 100$, see Figure 3.4.

Without loss of generality, we work in the "computational frame", described in Eq (1.167). This is indeed a convenient choice of geometry, as in this reference frame $F_a^{\times} = 0$. For anisotropic ORFs, one will need to rotate the the pulsars back into the cosmic rest frame from this "computational frame" using Wigner

D matrices given in Allen and Ottewill [1997]; Mingarelli et al. [2013].

For the isotropic case, $Y_0^0 = 1/\sqrt{4\pi}$ and therefore Eq. (1.164) reduces to

$$ {}^{(ab)}\Gamma_0^0 = \frac{1}{\sqrt{4\pi}} \int_{S^2} d\hat{\Omega} \left[1 - e^{i2\pi f L_a (1+\hat{\Omega}\cdot\hat{p}_a)}\right] \left[1 - e^{-i2\pi f L_b (1+\hat{\Omega}\cdot\hat{p}_b)}\right] F_a^+(\hat{\Omega}) F_b^+(\hat{\Omega}). \tag{3.5} $$

We define

$$ M = 2\pi f L_a (1 + \cos\theta), \tag{3.6} $$

$$ N = 2\pi f L_b (1 + \cos\theta\cos\zeta + \sin\theta\sin\zeta\cos\phi)\,, \tag{3.7} $$

in order to write $\kappa_{ab}(f, \hat{\Omega})$ in terms of sine and cosine functions, separating the function into real and imaginary components:

$$ \kappa_{ab}(f, \hat{\Omega}) = (1 - e^{iM})(1 - e^{-iN}), \tag{3.8} $$

$$ = \cos(M - N) - \cos M - \cos N + 1 $$

$$ + i[\sin(M - N) - \sin M + \sin N]. \tag{3.9} $$

The contour plots in Figs 3.2, 3.3 indicate that an approximation which allows fL_a and fL_b to vary is best for anisotropic ORFs, hence, we first present a Taylor series expansion of $\kappa_{ab}(f, \hat{\Omega})$ for small ζ for any fL_a and fL_b, and then set $L_a = L_b = L$ as a special case.

For small ζ, one can write down an approximation of the $\kappa_{ab}(f, \hat{\Omega})$ as:

$$\begin{aligned}
&\kappa_{ab}(f,\hat{\Omega})_{\rm real} \approx 1 - \cos M - \cos N + \cos(M-N) \\
&+\zeta 2\pi f L_b \sin\theta\cos\phi\,[\sin N + \sin(M-N)] \\
&+\zeta^2 \pi f L_b \left\{2\pi f L_b \sin^2\theta\cos^2\phi\,[\cos N - \cos(M-N)]\right. \\
&\left. -\cos\theta\,[\sin(N) + \sin(M-N)]\right\}\,,
\end{aligned} \tag{3.10}$$

and

$$\begin{aligned}
&\kappa_{ab}(f,\hat{\Omega})_{\rm imag} \approx -\sin M + \sin N + \sin(M-N) \\
&+\zeta 2\pi f L_b \sin\theta\cos\phi\,[\cos N - \cos(M-N)] \\
&+\zeta^2 \left\{-2\pi^2 f^2 L_b^2 \sin^2\theta\cos^2\phi\,[\sin N + \sin(M-N)]\right. \\
&\left. -\pi f L_b \cos\theta\,[\cos N - \cos(M-N)]\right\}\,.
\end{aligned} \tag{3.11}$$

When $L_a = L_b = L$ we find this reduces to

$$\begin{aligned}
&\kappa_{ab}(f,\hat{\Omega}) \approx 2 - 2\cos N + 2\zeta\pi f L \sin N\cos\phi\sin\theta \\
&+\zeta^2\pi f L[-\cos\theta\sin N + 2\pi f L(\cos N - 1)\sin^2\theta\cos^2\phi] \\
&+i\zeta 2\pi f L\sin\theta\cos\phi(\cos N - 1) \\
&+i\zeta^2\pi f L[\cos\theta(1-\cos N) - 2\pi f L\sin N\sin^2\theta\cos^2\phi]\,.
\end{aligned} \tag{3.12}$$

Numerically, we find that Eq (3.12) is a good approximation for to Eq (1.165)

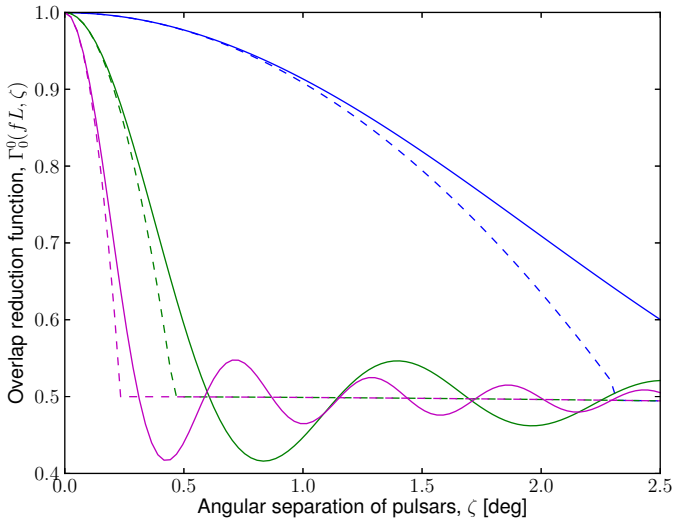

Figure 3.4: The small angle approximation of the isotropic ORF compared to the full ORF. Moving from right to left: the solid line is the full ORF and the dashed line is the approximation given by Eq (3.12) for $fL = 10$ (online blue), $fL = 51.2$ (green), and $fL = 100$ (magenta). Empirically, we find that the approximation holds for $\zeta \lesssim 2.3°(fL/10)$, Eq (3.13). Afterward the ORF reverts to the Earth-term only solution which, due to its slowly varying initial slope, appears to be flat over $0° \leq \zeta \leq 3°$.

for when evaluating the isotropic ORF for

$$\zeta \lesssim 2.3° \left(\frac{fL}{10}\right) , \tag{3.13}$$

as seen in Figure 3.4. When $\zeta = 0$, Eq (3.12) simplifies to $2 - 2\cos M$, where $M = N = 2\pi fL(1 + \cos\theta)$. One may safely ignore the $-2\cos M$ term since it is suppressed by a factor of at least $1/fL$. Sec 3.4 gives more details on this. As one may expect, the imaginary part of $\kappa_{ab}(f, \hat{\Omega})$ vanishes for the $L_a = L_b$ isotropic case but is otherwise non-vanishing. This fact is somewhat masked by the use of the magnitude of the ORFs, instead of the individual real and imaginary

components.

Using the pulsars found in the IPTA Mock Data Challenge 1, see IPTA [2012], we found that the smallest separation between pulsar pairs was $\zeta \sim 3.5°$ for pulsars J1853+1303 and J1857+0943. Although this angle is indeed small, and according to Table 3.1 puts the pulsars in the strong pulsar term regime for anisotropic ORFs, the distances to these pulsars found in the ATNF [2014] catalogue, are 1.6 kpc and 0.9 kpc, respectively. Therefore, their fL values in the low frequency limit are 168 and 90, respectively. The Earth-term only ORF is therefore still a reasonable approximation for pulsar pairs in the IPTA mock data challenge.

3.4 Correlated phase changes for pulsars within a radiation wavelength of Earth

The ATNF [2014] pulsar catalogue lists 107 pulsars which are less than 1 kpc away, 16 of which are closer than 300 pc, and three which are only 160 pc away. Our results suggest that one can ignore the pulsar term (except for the autocorrelation) if the distance between the pulsars $L_b - L_a$ in the z-direction is larger than a radiation wavelength, and/or $\zeta fL \geq 1$, cf. Figs 3.2, 3.3, depending on the ORF.

The last assumption we relax in this study is that many radiation wavelengths separate the Earth from the pulsars. Although current astrophysical constraints place a lower limit of $fL = 10$, this limit may decrease as more pulsars are found and added to PTAs. Therefore for completeness, we investigate the behaviour of the ORFs when $fL \sim 1$, i.e. when the Earth and the pulsar are separated by

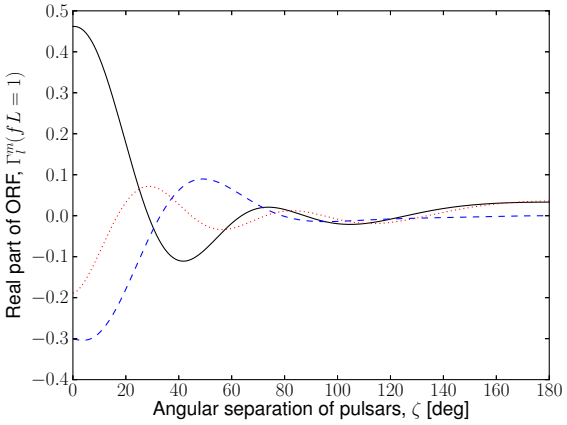

(a) Real part, Pulsar term - Earth term ORF

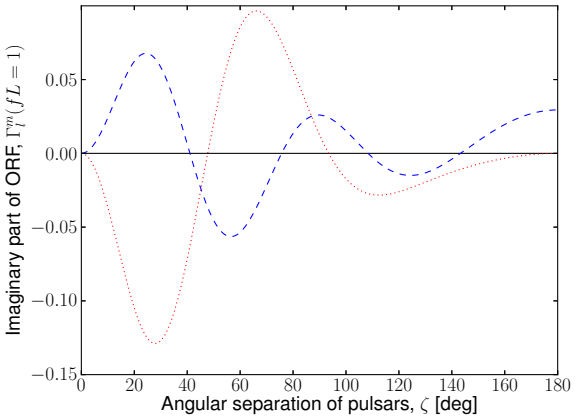

(b) Imaginary part of the ORFs

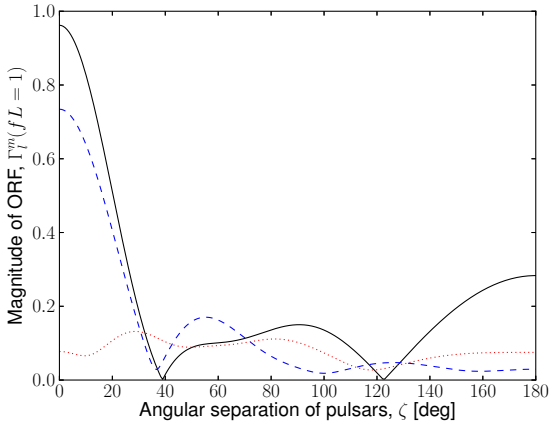

(c) Magnitude of the overlap reduction functions

Figure 3.5: In both panels ${}^{(ab)}\Gamma_0^0(fL,\zeta)$ is the solid curve, ${}^{(ab)}\Gamma_1^0(fL,\zeta)$ is the dashed curve (blue) and ${}^{(ab)}\Gamma_2^0(fL,\zeta)$ is the dotted curve (red). These functions are the most sensitive to the pulsar term, as they have non-zero values at $\zeta = 0$. (a) The behaviour of the pulsar term only for ${}^{(ab)}\Gamma_0^0(fL,\zeta)$, ${}^{(ab)}\Gamma_1^0(fL,\zeta)$ and ${}^{(ab)}\Gamma_2^0(fL,\zeta)$ when $L_a = L_b = L$ and $fL = 1$. This is found by subtracting the Earth term from the numerically integrated overlap reduction function. (b) The imaginary part only of ${}^{(ab)}\Gamma_0^0(fL,\zeta)$, ${}^{(ab)}\Gamma_1^0(fL,\zeta)$ and ${}^{(ab)}\Gamma_2^0(fL,\zeta)$ when $fL = 1$. As there is no imaginary part in the computational frame where the Earth term is calculated, we cannot display the difference as done is (a). Note that these imaginary values are only a factor a few smaller than their real counterparts, with the exception of ${}^{(ab)}\Gamma_0^0(fL,\zeta)$ where the imaginary part is zero. Moreover, they do not quickly converge to zero as in previous cases for $fL \geq 10$

only one radiation wavelength.

Previously, we assumed that the $-2\cos M$ contribution to the isotropic ORF integral was small as it would be suppressed by at least $1/fL$, see Sec 3.3. Here we investigate if this argument holds for $fL = 1$. We therefore calculate the exact expression for the product of $-2\cos M$, the antenna beam pattern and the fundamental harmonic as an example. Analogous calculations may be carried out for higher multipole moments.

Let $M = 2\pi fL(1+\cos\theta)$. We look to solve

$$^{ab}\Gamma_0^0(fL, \zeta = 0) = \beta \int_{S^2} d\hat{\Omega} \sum_A (2 - 2\cos M) Y_0^0 F_a^A F_b^A. \tag{3.14}$$

The product of the antenna beam pattern, $F_a^A F_b^A$, the harmonic Y_0^0 (or any harmonic) and the factor of 2 yields the usual doubling of PTA ORFs when $\zeta = 0$, normally modelled by a delta function $(1 + \delta_{ab})$. The $\beta = 3/(4\sqrt{\pi})$ is the normalization applied to all ORFs, which guarantees that the isotropic ORF yields a value of 1 for the autocorrelation term.

We now write down a solution for the product of $-2\cos M$,the antenna beam pattern and the spherical harmonic $Y_0^0 = 1/\sqrt{4\pi}$, integrated over the sky. We decompose the overlap reduction function into the sum of two components: $^{(ab)}\Gamma_l^m = 1/4\beta(Q_l^m + R_l^m)$, as in Anholm et al. [2009] and Mingarelli et al. [2013]. We carry out this computation in the reference frame described by Eq (1.167). Using Eq A29 with $l = 0$ from the Appendix of Mingarelli et al. [2013] completes the integration in ϕ, leaving the integration in θ:

$$Q_0^0 = -\frac{4\pi}{\sqrt{4\pi}} \int_0^\pi d\theta \sin\theta (1 - \cos\theta)^2 \cos[2\pi fL(1+\cos\theta)], \tag{3.15}$$

and write the solutions using spherical Bessel functions of the first kind, specifically $j_0(x) = \sin(x)/x$:

$$Q_0^0 = -\frac{4\sqrt{\pi}}{(2\pi fL)^3}\left[4\pi fL - \sin 4\pi fL\right], \tag{3.16}$$

$$= -\frac{8\sqrt{\pi}}{(2\pi fL)^2}\left[1 - j_0(4\pi fL)\right]. \tag{3.17}$$

To evaluate R_0^0 we make use of Eq A30 from the Appendix of Mingarelli et al. [2013] where the integral in ϕ is already solved:

$$\begin{aligned} R_0^0 &= 8\sqrt{\pi}(1-\cos\zeta)\int_0^{\pi-\zeta} d\theta \frac{(1-\cos\theta)^2\cos M}{\sin\theta} \\ &+ 8\sqrt{\pi}(1+\cos\zeta)\int_{\pi-\zeta}^{\pi} d\theta \sin\theta\cos M \qquad (3.18) \\ &= 0. \qquad (3.19) \end{aligned}$$

Since $\zeta = 0$ there is no contribution from the above equation, as the first piece is pre-multiplied by 0, and the second piece is integrated from $[\pi, \pi]$.

Therefore, the product of $-2\cos M$ with the antenna beam pattern and the fundamental harmonic, evaluated at $\zeta = 0$, is:

$$-2\beta\int_{S^2} d\hat{\Omega}\cos[2\pi fL(1+\cos\theta)]Y_0^0 F_a^A F_b^A = -\frac{3}{8\pi^2(fL)^2}\left[1 - j_0(4\pi fL)\right]. \tag{3.20}$$

The prefactor in Eq (3.20) scales as

$$3.8\times 10^{-2}\left(\frac{fL}{1}\right)^{-2}, \tag{3.21}$$

which suppresses the contribution from this function for any value of $fL \geq 1$. It is now clear that when $\zeta = 0$, it is adequate to approximate the pulsar term by multiplying the ORF by 2, and neglect the small oscillatory piece in Eq (3.20).

3.5 Conclusion

In this paper we have allowed the pulsar distances in a PTA to vary in the evaluation of the isotropic, dipole and quadrupole overlap reduction functions. For the first time, we have carried out an in-depth study of the behaviour of the pulsar term when pulsar pairs are separated by a few radiation wavelengths, see Figs 3.2, 3.3.

In Sec 3.2, we found that in a 10^{-9} Hz stochastic GW background, and for a pulsar 100 pc from the Earth, all of the ORFs evaluated return a maximum value for pulsars which are equidistant from the Earth. The stochastic GW background is expected to be largely isotropic at 10^{-9} Hz, however for completeness we calculate the fractional differences between the full and Earth-term-only ORFs, reported in Table 3.1, for ORFs up to $l = 2$. Interestingly, we find that the most significant fractional differences between the full and Earth-term only ORFs are found in the anisotropic ORFs. For example, for ${}^{(ab)}\Gamma_2^2(fL, \zeta)$, the maximum fractional difference between the full and Earth-term ORF is 188 (or $18,800\%$), for pulsars separated by 3.1°, which are located at 100 pc from the Earth.

More relevant to current stochastic GW background searches is the fractional difference between the magnitude of the full and Earth-term-only isotropic ORF, which can be as much as 100%, see Table 3.1, Figs 3.2(a), 3.2(b). Therefore, a Taylor expansion of the pulsar term was calculated in Sec 3.3, and this expression

can be readily input into GW data analysis pipelines. We find the approximation should be used for pulsar pairs separated by $\zeta \leq 2.3°(fL/10)$, Eq (3.13), and in this regime, the Taylor series expansion closely follows the form of the full ORF.

Looking to the future, we examined the behaviour of the isotropic, dipole and quadrupole ORFs when the pulsars are within a radiation wavelength of the Earth in Sec 3.4. We found there would be strong deviations from the usual delta-function like behaviour of the pulsar term, which is currently used in searches. Throughout this paper, pulsars from the IPTA mock data challenge were used to show that the short wavelength approximation used in current PTA searches still holds, although this may not always be true.

3. THE EFFECT OF SMALL PULSAR DISTANCE VARIATIONS IN STOCHASTIC GW BACKGROUND SEARCHES WITH PTAS

Chapter 4

OBSERVING THE DYNAMICS OF SUPERMASSIVE BLACK HOLE BINARIES WITH PULSAR TIMING ARRAYS

This chapter is based on

C. M. F Mingarelli, K. Grover, R. J. E. Smith, T. Sidery, A. Vecchio, "Observing the dynamical evolution of a super massive black hole binary using Pulsar Timing Arrays", Physical Review Letters, Volume 109, Issue 8 (2012), cited as Mingarelli et al. [2012]. Minor modifications here have been made to the paper: Fig 4.1 and Fig 4.2 have been added to clarify the geometry and the importance of the precession effects respectively, and equations which were previously inline are now in standard form. These changes are meant to improve the readability of the text, and were not possible in the published version due to word restrictions form the

Journal. Equations which were derived in the introduction are referenced and not repeated. I calculated the precession rate of the orbital angular momentum, the orbital evolution timescale and velocity of the binaries and wrote the draft of the paper.

4.1 Introduction

Gravitational waves (GWs) provide a new means for studying black holes and addressing open questions in astrophysics and fundamental physics: from their formation, evolution and demographics, to the assembly history of galactic structures and the dynamical behaviour of gravitational fields in the strong non-linear regime. Specifically, GW observations through a network of radio pulsars used as ultra-stable clocks – Pulsar Timing Arrays (PTAs), e.g. Detweiler [1979]; Estabrook and Wahlquist [1975]; Sazhin [1978] – represent the only *direct* observational avenue for the study of supermassive black hole binary (SMBHB) systems in the $\sim 10^8 - 10^9 M_\odot$ mass range, with orbital periods between ~ 1 month and a few years, see e.g. Sesana [2012]; Volonteri [2010] and references therein. Ongoing observations, cf. Ferdman et al. [2010]; Hobbs et al. [2010]; Jenet et al. [2009]; Verbiest et al. [2010] and future instruments, e.g. the Square Kilometre Array– SKA [2014]– are expected to yield the necessary timing precision to observe the diffuse GW background, cf. Liu et al. [2011]; Verbiest et al. [2009] .

This background is likely dominated by the incoherent superposition of radiation from the cosmic population of massive black holes, e.g. Demorest et al. [2013]; Hellings and Downs [1983]; Jaffe and Backer [2003]; Jenet et al. [2006]; Rajagopal and Romani [1995]; Sesana et al. [2004, 2008]; van Haasteren et al.

[2011]; Wyithe and Loeb [2003] and within it, we expect a handful of sources that are sufficiently close, massive and high-frequency to be individually resolvable, cf. Babak and Sesana [2012]; Ellis et al. [2012a,b]; Jenet et al. [2004]; Lee et al. [2011]; Sesana and Vecchio [2010]; Sesana et al. [2009]; Wen et al. [2011]; Yardley et al. [2010].

Massive black hole formation and evolution scenarios predict the existence of a large number of SMBHBs e.g. Koushiappas and Zentner [2006]; Malbon et al. [2007]; Volonteri et al. [2003]; Yoo et al. [2007]. Furthermore, SMBHs are expected to be (possibly rapidly) spinning, according to studies carried out by Hughes and Blandford [2003]; Merritt and Ekers [2002]. In fact the dynamics of such systems – which according to general relativity are entirely determined by the masses and spins of the black holes, e.g. Misner et al. [1973] – leave a direct imprint on the emitted gravitational waveforms. From these, one could measure SMBHB masses and their distribution, yielding new insights into the assembly of galaxies and the dynamical processes in galactic nuclei, e.g. Wen et al. [2011]. Moreover, measuring the magnitude and/or orientation of spins in SMBHBs would provide new information on the role of accretion processes, cf. Berti and Volonteri [2008]; Dotti et al. [2010]; Gammie et al. [2004]; Perego et al. [2009]; Volonteri et al. [2005]. Finally, detections of SMBHBs could allow us to probe general relativistic effects in the non-linear regime in an astrophysical context not directly accessible by other means, see Psaltis [2008]; Stairs [2003]; Will [2006] and references therein.

The observation of GWs with PTAs relies on the detection of the small deviation induced by gravitational radiation in the times of arrival (TOAs) of radio pulses from millisecond pulsars that function as ultra-stable reference clocks. This

deviation, called the residual, is the difference between the expected (without GW contribution) and actual TOAs once all the other physical effects are taken into account. The imprint of GWs on the timing residuals is the result of how the propagation of radio waves is affected by the GW-induced space-time perturbations along the travel path. It is a linear combination of the GW perturbation at the time when the radiation transits at a pulsar, the so-called "pulsar term", and then when it passes at the radio receiver, the "Earth term", cf. Detweiler [1979]; Estabrook and Wahlquist [1975]; Sazhin [1978]. The two terms reflect the state of a GW source at two *different* times of its evolution separated by

$$\tau \equiv (1 + \hat{\mathbf{\Omega}} \cdot \hat{\mathbf{p}})\, L_p \sim 3.3 \times 10^3\, (1 + \hat{\mathbf{\Omega}} \cdot \hat{\mathbf{p}}) \left(\frac{L_p}{1\,\mathrm{kpc}}\right)\ \mathrm{yr}, \tag{4.1}$$

where $\hat{\mathbf{\Omega}}$ and $\hat{\mathbf{p}}$ are the unit vectors that identify the GW propagation direction and the pulsar sky location at a distance L_p from the Earth, respectively, see *e.g.* Sesana and Vecchio [2010]. [We use geometrical units in which $G = c = 1$.] In a network (array) of pulsars all the perturbations at the Earth add coherently and therefore boost the signal-to-noise ratio (S/N) of the signal. Each pulsar term is at a slightly different frequency since the orbital period of the binary evolves over the time τ.

Measuring the key physics of SMBHBs is hampered by the short (typically $T = 10$ yr) observation time compared to the typical orbital evolution timescale (cf. Eqs (1.71) and (1.72))

$$\frac{f_{\mathrm{GW}}}{\dot{f}_{\mathrm{GW}}} = 1.6 \times 10^3 \left(\frac{\mathcal{M}}{10^9\, M_\odot}\right)^{-5/3} \left(\frac{f_{\mathrm{GW}}}{50\,\mathrm{nHz}}\right)^{-8/3}\ \mathrm{yr}\,, \tag{4.2}$$

of binaries that are still in the weak field adiabatic inspiral regime, with an orbital velocity v, cf Eq (1.13),

$$v = 0.12 \left(\frac{M}{10^9\, M_\odot}\right)^{1/3} \left(\frac{f_{\rm GW}}{50\,{\rm nHz}}\right)^{1/3} . \tag{4.3}$$

Here $M = m_1 + m_2$, $\mu = m_1 m_2/M$ and $\mathcal{M} = M^{2/5}\mu^{3/5}$ are the total, reduced and chirp mass, respectively, of a binary with component masses $m_{1,2}$, and $f_{\rm GW}$ is the GW emission frequency at the leading quadrupole order. The chirp mass determines the frequency evolution at the leading Newtonian order. In the post-Newtonian (pN) expansion of the binary evolution, e.g. Blanchet [2006] in terms of $v \ll 1$, the second mass parameter enters at p^{1}N order ($\mathcal{O}(v^2)$ correction); spins contribute at p$^{1.5}$N order and above ($\mathcal{O}(v^3)$) causing the orbital plane to precess through spin-orbit coupling, at leading order. These contributions are therefore seemingly out of observational reach.

The GW effect at the pulsar – the pulsar term – may be detectable in future surveys, and for selected pulsars their distance could be determined to sub-parsec precision, see e.g. Deller et al. [2008]; Lee et al. [2011]; Smits et al. [2011]. If this is indeed the case, it opens the opportunity to coherently connect the signal observed at the Earth and at pulsars, therefore providing snapshots of the binary evolution over $\sim 10^3$ yr. These observations would drastically change the ability to infer SMBHB dynamics, and study the relevant astrophysical process and fundamental physics.

In this *Letter* we show that for SMBHBs at the high end of the mass and frequency spectrum observable by PTAs, say $m_{1,2} = 10^9\, M_\odot$ and $f_{\rm GW} = 10^{-7}$ Hz, the observations of a source still in the weak-field regime become sensitive to

post-Newtonian contributions up to $\mathrm{p}^{1.5}\mathrm{N}$, including spin-orbit effects, if both the pulsar and Earth term can be detected. This in principle enables the measurement of the two mass parameters and a combination of the spin's magnitude and relative orientation. We also show that the Earth-term only can still be sensitive to spin-orbit coupling due to geometrical effects produced by precession. We discuss the key factors that enable these measurements, and future observational prospects and limitations.

4.2 Signals from SMBHBs

Consider a radio pulsar emitting radio pulses at frequency ν_0 in the source rest-frame. GWs modify the rate at which the radio signals are received at the Earth, see e.g. Detweiler [1979]; Estabrook and Wahlquist [1975]; Sazhin [1978], inducing a relative frequency shift $\delta\nu(t)/\nu_0 = h(t-\tau) - h(t)$, where $h(t)$ is the GW strain. The quantities that are actually produced at the end of the data reduction process of a PTA are the timing residuals, $\int dt'\, \delta\nu(t')/\nu_0$, although without loss of generality, we will base the discussion on $h(t)$. The perturbation induced by GWs is repeated twice, and carries information about the source at time t, the "Earth term", and at past time $t-\tau$ the "pulsar term".

We model the radiation from a SMBHB using the so-called restricted pN approximation, in which pN corrections are included only in the phase and the amplitude is retained at the leading Newtonian order, but we include the leading order modulation effects produced by spin-orbit coupling. The strain is given by

$$h(t) = -A_{\mathrm{gw}}(t) A_{\mathrm{p}}(t) \cos[\Phi(t) + \varphi_{\mathrm{p}}(t) + \varphi_{\mathrm{T}}(t)]\,, \tag{4.4}$$

where

$$A_{\rm gw}(t) = \frac{2}{D}[\pi f_{\rm GW}(t)]^{2/3}\mathcal{M}^{5/3} \tag{4.5}$$

is the Newtonian order GW amplitude, $\Phi(t)$ is the GW phase, see *e.g.* Eq. (232, 234) in Blanchet [2006] and Eq. (8.4) in Blanchet et al. [2006], and D is the distance to the GW source. $A_p(t)$ and $\varphi_p(t)$ are the time-dependent polarisation amplitude and phase and $\varphi_{\rm T}(t)$ is an additional phase term, analogous to Thomas precession, see Eq. (29) in Apostolatos et al. [1994].

The physical parameters leave different observational signatures in the GW strain $h(t)$ and are therefore found in the TOA residuals. At the leading Newtonian order, $\mathcal{M}$ drives the frequency and therefore the phase $\Phi(t)$ evolution, with the second independent mass parameter entering from the p^{1}N onwards. SMBHs are believed to be rapidly spinning, and the spins are responsible for three distinctive imprints in the waveform:

- they alter the phase evolution through spin-orbit coupling and spin-spin coupling at p$^{1.5}$N and p^{2}N order, respectively, cf. Kidder et al. [1993],
- they cause the orbital plane to precess due to (at lowest order) spin-orbit coupling and therefore induce amplitude and phase modulations in the waveform through $A_p(t)$ and $\varphi_p(t)$; and
- through orbital precession they introduce an additional secular contribution $\varphi_{\rm T}(t)$ to the waveform phase.

Astrophysically we expect PTAs to detect SMBHBs of comparable component masses, cf. Sesana and Vecchio [2010]. We therefore model the spin-orbit precession using the *simple precession approximation*, see e,g, Apostolatos et al. [1994],

which formally applies when $m_1 = m_2$, or when one of the two spins is negligible with respect to the other. Let $\mathbf{S}_{1,2}$ and $\mathbf{L}$ be the black holes' spins and the orbital angular momentum, respectively. Then both $\mathbf{S} = \mathbf{S}_1 + \mathbf{S}_2$ and $\mathbf{L}$ precess around the (essentially) constant direction of the total angular momentum, $\mathbf{J} = \mathbf{S} + \mathbf{L}$, at the same rate

$$\frac{d\alpha}{dt} = \pi^2 \left(2 + \frac{3m_2}{2m_1}\right) \frac{(|\mathbf{L} + \mathbf{S}|) f_{\rm GW}^2(t)}{M}\,, \tag{4.6}$$

as in Apostolatos et al. [1994], where α is the precession angle, while preserving the angle of the precession cone, λ_L, see Fig 4.1. This approximation is adequate to conceptually explore these effects, however in the case of real observations, one will need to consider the exact expressions, cf. Kidder [1995].

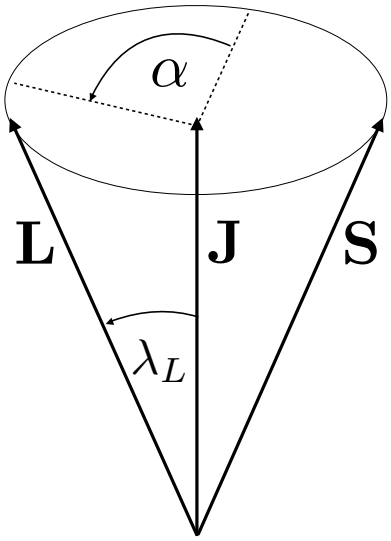

Figure 4.1: Precession geometry for a spinning binary: here λ_L is the angle of the precession cone, α is the precession angle, and the total spin $\mathbf{S} = \mathbf{S}_1 + \mathbf{S}_2$ and the orbital angular momentum $\mathbf{L}$ precess around the (essentially) constant direction of the total angular momentum, $\mathbf{J} = \mathbf{S} + \mathbf{L}$ at a rate $d\alpha/dt$, given by Eq (4.6).

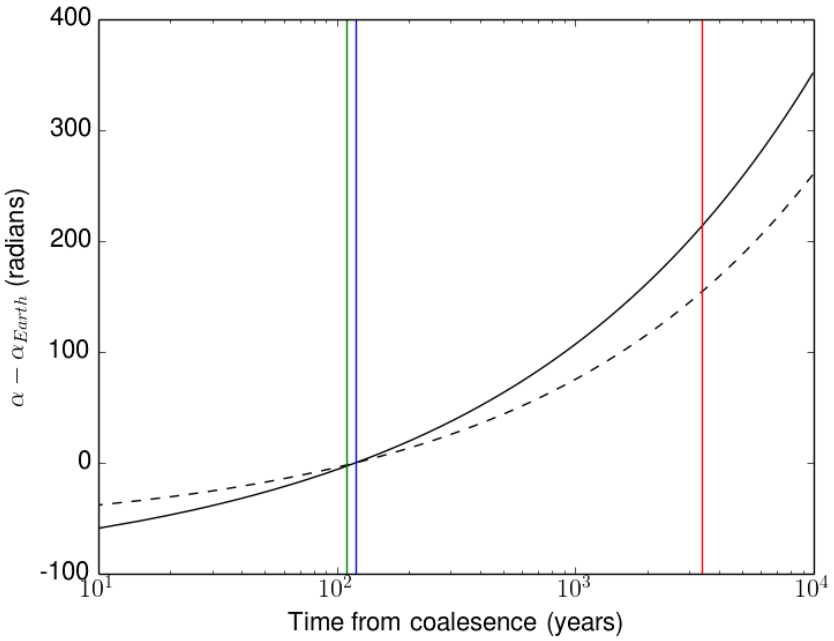

Figure 4.2: The precession angle $\alpha = 0$ at the Earth, as a reference. The red line highlights a distance of 1 kpc, the blue line is the beginning of the observation at the Earth and the green line is after a 10 year observation, hence is closer to coalescence. For the a dimensionless spin parameter $a = 0.98$ ($a = 0.10$), the solid (dashed) line is the change in α for a $10^9 M_\odot$ SMBHB . Over 10 years, $\Delta\alpha \sim -3$ rads (-2 rads), however, over 1 kpc, $\Delta\alpha =\sim 213$ rads (154 rads).

The detection and particularly the measurement of the aforementioned parameters relies on coherently matching the signal with a template that faithfully reproduces its amplitude and, importantly, its phase evolution. We therefore consider the contribution to the total number of wave cycles a proxy for the significance of a specific parameter. Individual terms that contribute ~ 1 GW cycle or more mean that the effect is in principle detectable, hence one can infer information about the associated parameter(s).

We show that information about the parameters can only be inferred for SMBHBs at the high end of the mass spectrum and PTA observational frequency

range. Having a sufficiently high-mass and high-frequency GW source is also essential to ensure sufficient frequency evolution over the time τ, so that the Earth and pulsar term are clearly separated in frequency space cf. Table 4.1. We therefore take fiducial source parameters of $m_1 = m_2 = 10^9\,M_\odot$, frequency at the Earth at the beginning of the observation $f_{\rm GW,E} = 10^{-7}$ Hz and an observational time $T = 10$ years to illustrate the main results. We provide scaling relations as a function of the relevant quantities, allowing the reader to rescale the results for different astrophysical and/or observational values.

4.3 Observations using the Earth-term only

We start by considering analyses that rely only on the Earth-term contribution to the residuals, as done in Lommen and Backer [2001]; Yardley et al. [2010]. The case of a coherent analysis based both on the Earth- and pulsar-term, introduced in Jenet et al. [2004], is discussed later in this Letter. Table 4.1 shows that, in general, the frequency change over 10 yr is small compared to the frequency bin width, $3.2(10\,{\rm yr}/T)$ nHz, e.g. Lee et al. [2011]; Sesana and Vecchio [2010]. The observed signal is effectively monochromatic, making the dynamics of the system impossible to infer. However, the presence of spins affects the waveform not only through the GW phase evolution, but also via the modulations of $A_{\rm p}(t)$ and $\varphi_{\rm p}(t)$ that are periodic over the precession period, *and* also introduces the secular contribution $\varphi_{\rm T}(t)$. For $m_{1,2} = 10^9\,M_\odot$ and $f_{mathrmGW,\ E} = 10^{-7}$ Hz the orbital angular momentum precesses by $\Delta\alpha = 2$ rad (for dimensionless spin parameter $a \equiv S/M^2 = 0.1$) and $\Delta\alpha = 3$ rad (for $a = 0.98$), as seen in Fig 4.2, and therefore the additional modulation effect on $A_{\rm p}(t)$ and $\varphi_{\rm p}(t)$ is small, and

likely undetectable. However, the overall change of $\varphi_{\rm T}(t)$ over 10 yrs could be appreciable: the average contribution for each precession cycle of this additional phase term is $\langle\Delta\varphi_{\rm T}\rangle = 4\pi$ or $4\pi\,(1-\cos\lambda_L)$, depending on whether $\hat{\mathbf{\Omega}}$ lies inside or outside the precession cone, respectively, cf. Apostolatos et al. [1994]. If $\hat{\mathbf{\Omega}}$ lies inside the precession cone, and given that the observation will cover between a third and a half of a full precession cycle, then $\langle\Delta\varphi_{\rm T}\rangle \sim \pi$, which could surely indicate the presence of spins. On the other hand, the precession cone will be small in general since

$$\left|\frac{S}{L}\right| \sim a\,v\,\frac{M}{\mu} \simeq 0.1\,a\,\frac{M}{\mu}\,\left(\frac{M}{10^9\,M_\odot}\right)^{1/3}\,\left(\frac{f_{\rm GW}}{100\,{\rm nHz}}\right)^{1/3}\,, \tag{4.7}$$

where $L = \mu M^{1/2} r^{1/2}$. Therefore the likelihood of $\hat{\mathbf{\Omega}}$ lying inside the precession cone is small, assuming an isotropic distribution and orientation of sources. In this case the Thomas precession contribution (per precession cycle) is suppressed by a factor

$$(1-\cos\lambda_L) \simeq \lambda_L^2/2 \sim 5\times10^{-3}\,a^2\,\left(\frac{M}{\mu}\right)^2\,\left(\frac{M}{10^9\,M_\odot}\right)^{2/3}\,\left(\frac{f_{\rm GW}}{100\,{\rm nHz}}\right)^{2/3}\,, \tag{4.8}$$

which will produce a negligible contribution $\Delta\varphi_{\rm T}(t) \ll 1$. However unlikely, spins may still introduce observable effects that need to be taken into account.

$m_1(M_\odot)$	$m_2(M_\odot)$	$f_{\mathrm{GW,E}}$(nHz)	$(v/c \times 10^{-2})$	time-span Δf_{GW} (nHz)	Total	Newtonian	p^{1}N	p$^{1.5}$N	spin-orbit/β	p^{2}N
10^9	10^9	100	14.6	10 yr	3.22	32.1	31.7	0.9	-0.7	0.06	0.04
			9.6	1 kpc	71.2	4305.1	4267.8	77.3	-45.8	3.6	2.2
		50	11.6	10 yr	0.24	15.8	15.7	0.3	-0.2	0.01	< 0.01
			9.4	1 kpc	23.1	3533.1	3504.8	53.5	-28.7	2.3	1.2
10^8	10^8	100	6.8	10 yr	0.07	31.6	31.4	0.2	-0.07	< 0.01	< 0.01
			6.4	1 kpc	15.8	9396.3	9355.7	58.3	-19.9	1.6	0.5
		50	5.4	10 yr	0.005	15.8	15.7	0.06	-0.02	< 0.01	< 0.01
			5.3	1 kpc	1.62	5061.4	5045.8	20.8	-5.8	0.5	0.1

Table 4.1: Frequency change Δf, total number of GW cycles and individual contributions from the leading order terms in the pN expansion over the two relevant time scales – a 10 yr observation at the Earth and the time delay $-L_p(1 + \hat{\mathbf{\Omega}} \cdot \hat{\mathbf{p}})$ between the Earth and pulsar term – for selected values of $m_{1,2}$ and $f_{\mathrm{GW,\,E}}$.

4.4 Measuring SMBHB evolution using the Earth and pulsar term

With more sensitive observations and the increasing possibility of precisely determining L_p see *e.g.* Smits et al. [2011], the prospect of also observing the contribution from the pulsar-term from one or more pulsars becomes more realistic. We show below that *if* at least one of the pulsar terms can be observed together with the Earth-term, this opens opportunities to study the dynamical evolution of SMBHBs and, in principle, to measure their masses and spins. This is a straightforward consequence of the fact that PTAs become sensitive to $\sim 10^3$ yr of SMBHB evolutionary history, in "snippets" of length $T \ll L_p$ that can be coherently concatenated.

The signal from each pulsar term will be at a S/N which is significantly smaller than the Earth-term by a factor $\sim \sqrt{N_p}$, where N_p is the number of pulsars that effectively contribute to the S/N of the array. For example, if the Earth-term yields an S/N of $\sim 36\sqrt{N_p/20}$, then each individual pulsar term would give an S/N ~ 8. The possibility of coherently connecting the Earth-term signal with each pulsar term becomes therefore a question of S/N, prior information about the pulsar-Earth baseline and how accurately the SMBHB location in the sky can be reconstructed, as part of a "global fit", *e.g.* Lee et al. [2011]. Assuming for simplicity that the uncertainties on L_p and $\hat{\mathbf{\Omega}}$ are uncorrelated, this requires that the distance to the pulsar and the location of the GW source are known with errors $\lesssim 0.01(100\,\mathrm{nHz}/f_{\mathrm{GW}})$ pc and $\lesssim 3(100\,\mathrm{nHz}/f_{\mathrm{GW}})(1\,\mathrm{kpc}/L_p)$ arcsec, respectively. These are very stringent constraints, see e.g. Babak and Sesana [2012]; Sesana and Vecchio [2010]; Smits et al. [2011], and a detailed analysis

is needed in order to assess the feasibility of reaching this precision. Clearly if an electromagnetic counterpart to the GW source were to be found, e.g. Sesana et al. [2012]; Tanaka et al. [2012], it would enable the identification of the source location in the sky, making the latter constraint unnecessary.

We can now consider the contribution from the different terms in the pN expansion to the total number of cycles in observations that cover the GW source evolution over the time τ that are encoded in the simultaneous analysis of the Earth *and* pulsar terms. The results are summarised in Table 4.1, for selected values of $m_{1,2}$, and $f_{\rm GW,E}$ and for a fiducial value $\tau = 1\,{\rm kpc}$. The wavecycle contributions from the spin-orbit parameter are normalized to β as per Eq (1.76). Contributions from the p^{2}N order spin-spin terms are negligible. The results clearly show that despite the fact that the source is in the weak field regime the extended Earth-pulsar baseline requires the p$^{1.5}$N, and in some rare cases the p^{2}N contribution, to accurately (*i.e.* within ~ 1 GW cycle) reproduce the full phase evolution.

For $m_{1,2} = 10^9\,M_\odot$ and $f_{\rm GW,E} = 10^{-7}$ Hz there is a total of 4305 GW cycles over a 1 kpc light travel time evolution, with the majority (4267) accounted for by the leading order Newtonian term, providing information about the chirp mass, and tens of cycles due to the p^{1}N and p$^{1.5}$N terms (77 and 45, respectively), that provide information about a second independent mass parameter. Spins contribute to phasing at p$^{1.5}$N with $\sim 3\beta$ cycles. Therefore their total contribution is smaller than the p$^{1.5}$N mass contribution by a factor between a few and ~ 10. The additional Thomas precession phase contribution may become comparable to the p^{1}N mass contribution in some cases. In fact, for $a = 0.1(0.98)$ the binary undergoes 24 (34) precession cycles. This corresponds to a total Thomas

precession phase contribution of 306 (426) rad if $\hat{\mathbf{\Omega}}$ lies outside the precession cone.

The modulations of $A_{\rm p}(t)$ and $\varphi_{\rm p}(t)$ are characterised by a small $\lambda_{\rm L}$, because for most of the inspiral $S \ll L$, and are likely to leave a smaller imprint on the waveform than those discussed so far. We can indeed estimate the importance of this effect for the most favourable parameter combinations. The value of $\varphi_{\rm p}(t)$ oscillates over time with an amplitude which depends on the time to coalescence, $\mathbf{S}$, $\mathbf{L}$, $\hat{\mathbf{\Omega}}$ and $\hat{\mathbf{p}}$. We choose the orientation of $\hat{\mathbf{S}}$ such that λ_L is maximised, and we vary $\hat{\mathbf{\Omega}}$ and $\hat{\mathbf{p}}$, each of which is drawn from a uniform distribution on the two-sphere.

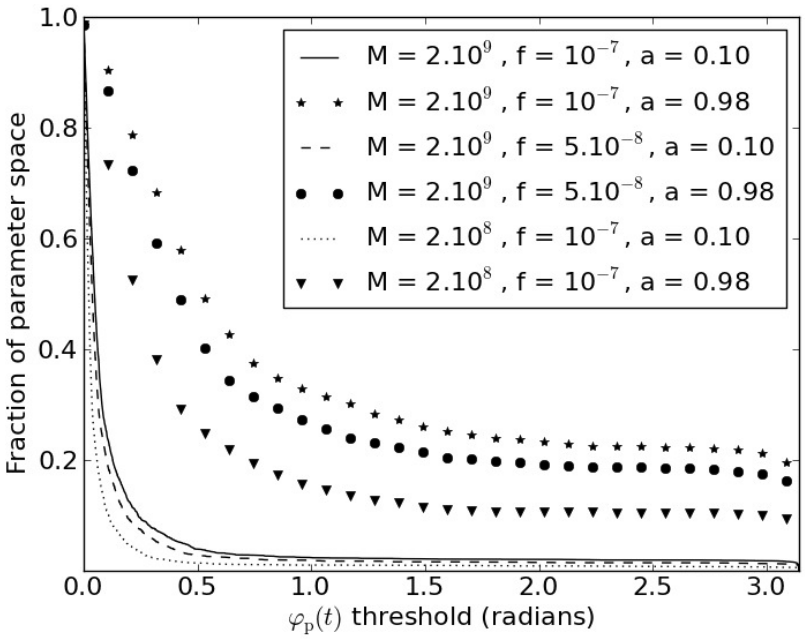

Figure 4.3: The fraction of parameter space in $\hat{\mathbf{\Omega}}$ and $\hat{\mathbf{p}}$ for which the maximum excursion of $\varphi_{\rm p}$ over the time $L_p(1+\hat{\mathbf{\Omega}}\cdot\hat{\mathbf{p}})$ for $L_p = 1\,{\rm kpc}$ exceeds a certain value, shown on the horizontal axis. Several values of $m_{1,2}$, a and $f_{\rm GW,E}$ are considered (see legend).

In Fig 4.3 we show that for rapidly spinning ($a = 0.98$) SMBHBs this effect

could introduce modulations larger than $\pi/2$ in $\varphi_{\rm p}(t)$ over 30% of the parameter space of possible $\hat{\mathbf{\Omega}}$ and $\hat{\mathbf{p}}$ geometries. The amplitude would correspondingly change over the same portion of the parameter space by at most 60% with respect to its unmodulated value. Since these effects are modulated, they will not be easily identifiable.

4.5 Conclusions

We have established that the coherent observation of both the Earth and pulsar term provides information about the dynamical evolution of a GW source. The question now is whether they can be unambigously identified. A rigorous analysis would require extensive simulations based on the actual analysis of synthetic data sets. We can however gain the key information with a much simpler order of magnitude calculation. The phase (or number of cycles) error scales as $\sim 1/(\mathrm{S/N})$. Assuming $\mathrm{S/N} \sim 40$ means that the total number of wave cycles over the Earth-pulsar baseline can be determined with an error $\sim 4300/40 \sim 100$ wave cycles. This is comparable to the $\mathrm{p}^1\mathrm{N}$ contribution to the GW phase and, in very favourable circumstances, to the Thomas precession phase contribution, and larger by a factor of a few or more than all the other contributions. It may therefore be possible to measure the chirp mass and, say, the symmetric mass ratio of a SMBHB, and possibly a combination of the spin parameters. Effects due to the $\mathrm{p}^{1.5}\mathrm{N}$ and higher phase terms are likely to remain unobservable, as well as amplitude and phase modulations. Correlations between the parameters, in particular masses and spins, will further degrade the measurements. The details will depend on the actual S/N of the observations, the GW source parameters,

and the accuracy with which the source location and the pulsar distance can be determined. We plan to explore these issues in detail in a future study.

4. OBSERVING THE DYNAMICS OF SUPERMASSIVE BLACK HOLE BINARIES WITH PULSAR TIMING ARRAYS

Chapter 5

CONCLUSIONS

5.1 Anisotropic stochastic GW background searches

Searches for the stochastic GW background are currently ongoing in NANOGrav, EPTA, PPTA and the IPTA. Within the EPTA, I am co-leading the search for an anisotropic stochastic GW background, based on the formalism introduced in Mingarelli et al. [2013] (equivalently Chapter 2). Indeed, in Mingarelli et al. [2013] we show that the stochastic GWB may have a fractional degree of anisotropy of around 20% at high frequencies, while Taylor and Gair [2013] show the effect of background-finiteness on the angular power-spectrum of the GWB. Expanding the standard search for an isotropic background to an anisotropic background allows one to place constraints on its degree of anisotropy, if any. In this project, we will search over anisotropy coefficients, the c_l^m's in Eq (2.19), within the power-law model of the strain-spectrum. At the lowest order, this will necessarily include

an upper limit on the monopole, which should be consistent with the isotropic working group (in prep). Furthermore, we will see how much the isotropic limit is affected by inclusion of different numbers of anisotropy coefficients in the search. We will then explore the current angular resolution of the EPTA which depends on the number of pulsars used. This will allow us to set a upper limit on the multipole moment, $l_{\rm max}$, we should use. We may find, on the other hand, that the upper limit on the amplitude converges once we reach a certain order, and there is no need to extend the analysis to $l_{\rm max}$.

Following this, our approach we will be to parametrize anisotropy-coefficients to be a function of frequency. We propose using the "hybrid time-frequency domain" technique introduced in Lentati et al. [2013] to follow the frequency-dependence (if any) of the background anisotropy. The motivation of this derives from the fact that the stochasticity of the strain-spectrum begins to break down at higher frequencies, as also shown in Sesana et al. [2008], such that the contribution to the signal becomes dominated by a handful of bright sources.

This analysis will then be carried out again the IPTA data set, currently in prep.

5.2 CMB-like stochastic GW background searches

Currently, I am working with Jon Gair, Steve Taylor and Joseph Romano on a project with the aim to describe how the formalism used to characterize the polarization of the cosmic microwave background (CMB), see e.g. Kamionkowski

et al. [1997], can be applied to the analysis of GW backgrounds. An arbitrary background can be decomposed into modes whose angular dependence on the sky is given by gradients and curls of spherical harmonics. We derive the pulsar timing overlap reduction function for individual modes and show how these can be used to recover the components of the background. An isotropic, uncorrelated background can be accurately recovered using only three components and therefore this search will be almost as sensitive as a direct search using the Hellings and Downs overlap reduction function, see e.g. Anholm et al. [2009]; Hellings and Downs [1983]; Mingarelli et al. [2013]. My contribution to this work is to provide a description of known anisotropic ORFs in this new representation of the GW backgrounds. Note that in this approach each individual mode on its own describes a background that is correlated between different points on the sky. A measurement of these components that is inconsistent with the expected values for an uncorrelated background would indicate new physics.

5.3 Future work

In June 2014, I will commence a new project in collaboration with researchers at Caltech and NASA's Jet Propulsion Laboratory. The aim of the project is to find the first ever direct evidence for GWs with PTAs by means of a new interdisciplinary collaboration in radio and infrared astronomy, data analysis and astrophysics. I will lead a team, coordinating my efforts with my mentors– Tom Prince, Joseph Lazio and Michael Kramer– and colleagues, which will search for candidate SMBHBs using galaxy catalogues. Having obtained the merger candidates, we will populate them with SMBHB candidates, according to an

appropriate BH mass distribution function. The result will be a realistic synthetic map, based on the spatial distribution and masses of the merger candidates, which can be used to predict the level of anisotropy in the local universe. I will apply the resulting anisotropy map to an extended GW search which implements the anisotropy formalism introduced in Chapter 2 or equivalently Mingarelli et al. [2013], using it to constrain the priors used to evaluate the likelihood function. We will then apply a novel extension of this formalism to the single source searches via a new hybridized method. In this approach, we search for GW hotspots– regions where we probabilistically believe one or more GW sources to be concentrated– using the anisotropic formulation, and then search within those hotspots for single sources using methods optimized for single source detection.

Appendix A

DERIVATION OF THE GENERALIZED OVERLAP REDUCTION FUNCTIONS

A.1 Derivation of the generalized overlap reduction function

In this Appendix we provide details for the derivation of the analytical expressions of the generalized overlap reduction functions in the computational frame, Eq (1.167), whose expressions are presented in Section 1.7. We begin by deriving identities and properties of integrals that will be used later in the derivations. Further comments on the isotropic solution are provided in Section A.1.1, the $l = 1$ (dipole) ORFs are derived in Section A.1.2, and the $l = 2$ ORFs are derived in Section A.1.3.

A. DERIVATION OF THE GENERALIZED OVERLAP REDUCTION FUNCTIONS

In the computational frame, the antenna beam patterns for pulsar a and b are given by Eqs (1.169). Substituting Eq. (1.169) into Eq. (2.38), the overlap reduction functions become:

$$
\begin{aligned}
{}^{(ab)}\Gamma_l^m = & -\frac{1}{4}(1+\delta_{ab})\int_0^{\pi} d\theta \sin\theta \\
& \times \int_0^{2\pi} d\phi Y_l^m \frac{(1-\cos\theta)\left[(\sin\phi\sin\zeta)^2 - (\sin\zeta\cos\theta\cos\phi - \sin\theta\cos\zeta)^2\right]}{1+\cos\theta\cos\zeta+\sin\theta\sin\zeta\cos\phi}
\end{aligned} \tag{A.1}
$$

One can write Eq (A.1) as the sum of two integrals:

$$
{}^{(ab)}\Gamma_l^m = \frac{1}{4}(Q_l^m + R_l^m)(1+\delta_{ab})\,, \tag{A.2}
$$

where

$$
\begin{aligned}
Q_l^m &= N_l^m \int_0^{\pi} d\theta \sin\theta(1-\cos\theta)P_l^m(\cos\theta) \\
&\times \int_0^{2\pi} d\phi(1-\cos\zeta\cos\theta-\sin\zeta\sin\theta\cos\phi)e^{im\phi}
\end{aligned} \tag{A.3}
$$

and

$$
R_l^m = -N_l^m 2\sin^2\zeta \int_0^{\pi} d\theta \sin\theta(1-\cos\theta)P_l^m(\cos\theta)I_m \tag{A.4}
$$

$$
I_m \equiv \int_0^{2\pi} d\phi \frac{e^{im\phi}\sin^2\phi}{1+\cos\zeta\cos\theta+\sin\zeta\sin\theta\cos\phi}\,, \tag{A.5}
$$

and the constant N_l^m is given by Eq. (2.37). The Q_l^m portion of the overlap

reduction function, Eq. (A.3), is only non-zero for $m = 0, \pm 1$:

$$Q_l^m \neq 0 \quad \text{iff } m = 0, \pm 1 \quad (\forall l)\,. \tag{A.6}$$

This can be shown via integration by parts of the integral in ϕ:

$$\begin{aligned}
&\int_0^{2\pi} d\phi(1-\cos\zeta\cos\theta-\sin\zeta\sin\theta\cos\phi)e^{im\phi} \\
&= -\int_0^{2\pi} d\phi \sin\zeta\sin\theta\cos\phi e^{im\phi} &\text{(A.7)}\\
&= -\sin\zeta\sin\theta\int_0^{2\pi} d\phi e^{im\phi}\cos\phi &\text{(A.8)}\\
&= \sin\zeta\sin\theta\frac{im}{m^2-1}(e^{2i\pi m}-1) = 0 \quad (|m| \geq 2)\,. &\text{(A.9)}
\end{aligned}$$

For $m = 0\,, \pm 1$, the integral in ϕ is handled as a special case:

$$\begin{aligned}
&\int_0^{2\pi} d\phi(1-\cos\zeta\cos\theta-\sin\zeta\sin\theta\cos\phi)e^{im\phi} \\
&= \begin{cases} 2\pi(1-\cos\zeta\cos\theta), & m = 0 \\ -\pi\sin\zeta\sin\theta, & m = \pm 1 \end{cases}
\end{aligned} \tag{A.10}$$

Note that the non-zero solutions given here are real-valued. We can now show that the generalised overlap reduction functions in the computational frame, given by Eq (A.1) are real $\forall\, l\,, m$.

We have just shown that the Q_l^m are real, therefore it remains to prove that R_l^m, Eq. (A.4), is also real $\forall\, l\,, m$. The complex component is introduced via the

ϕ dependence in Eq (A.5),

$$I_m \equiv \int_0^{2\pi} d\phi \frac{e^{im\phi}\sin^2\phi}{1+\cos\zeta\cos\theta+\sin\zeta\sin\theta\cos\phi}, \tag{A.11}$$

$$= \int_0^{2\pi} d\phi \frac{\cos m\phi\sin^2\phi}{1+\cos\zeta\cos\theta+\sin\zeta\sin\theta\cos\phi} + i\int_0^{2\pi} d\phi \frac{\sin m\phi\sin^2\phi}{1+\cos\zeta\cos\theta+\sin\zeta\sin\theta\cos\phi}\,. \tag{A.12}$$

The final integral which is a function of i can be written as an odd function over a symmetric interval for any value of m, hence it vanishes leaving only first, the real-valued, integral. Eq (A.5) can therefore be written as

$$I_m = \int_0^{2\pi} d\phi \frac{\cos m\phi\sin^2\phi}{1+\cos\zeta\cos\theta+\sin\zeta\sin\theta\cos\phi}, \tag{A.13}$$

which is real-valued $\forall\, l\,, m$ in the computational reference frame.

Lastly we introduce an identity which helps one to readily solve a common integral involving Legendre polynomials. Formally, we show that for any n-times differentiable function $g(x)$ and Legendre polynomial $P_n(x)$, the following equality holds:

$$\int_{-1}^{1} dx\, g(x)P_n(x) = \frac{(-1)^n}{2^n n!}\int_{-1}^{1} dx\,(x^2-1)^n g^{(n)}(x). \tag{A.14}$$

Using repeated applications of integration by parts, and using Rodrigues' formula for Legendre polynomials

$$P_n(x) = \frac{1}{2^n n!} D^n((x^2-1)^n)\,, \tag{A.15}$$

where D^n is the n^{th} derivative with respect to x, the left-hand side of Eq (A.14)

can be written as:

$$\int dx\ g(x)P_n(x) = g(x)\cdot\frac{1}{2^n n!}D^{n-1}[(x^2-1)^n] - g'(x)\cdot\frac{1}{2^n n!}D^{n-2}[(x^2-1)^n] + \cdots$$
$$+ (-1)^{n-1}g^{(n-1)}(x)\cdot\frac{1}{2^n n!}D^{(n-n)}[(x^2-1)^n] + \int dx(-1)^n g^n(x)\cdot\frac{1}{2^n n!}[(x^2-1)^n]. \tag{A.16}$$

We then evaluate Eq. (A.16) over $[-1,1]$ and note that in every boundary term, after the differentiations are performed, there is always a remaining term of the form $(x^2-1)^m$, for some m. Thus, this term vanishes at the end-points $[-1,1]$ leaving only the final integral term, thus proving Eq (A.14). We will make use of this identity regularly in the following sections describing dipole and quadrupole anisotropies.

A.1.1 Note on the isotropic solution

The derivation of the isotropic solution is given in Sec 1.7. However, it is useful to note that when one sets $m=0$ and solves the Q and R integrals, one does so for any higher harmonic with $m=0$. We can therefore write that for any $m=0$

$$Q_l^0 = 2\pi N_l^0 \int_0^\pi d\theta \sin\theta(1-\cos\theta)(1-\cos\zeta\cos\theta)P_l(\cos\theta), \tag{A.17}$$

$$R_l^0 = -4\pi N_l^0\beta\int_0^{\pi-\zeta} d\theta\frac{(1-\cos\theta)^2}{\sin\theta}P_l(\cos\theta) - 4\pi N_l^0\alpha\int_{\pi-\zeta}^{\pi} d\theta\sin\theta P_l(\cos\theta). \tag{A.18}$$

A.1.2 Dipole Anisotropy

The dipole anisotropy is described by the $l = 1$ and $m = 0, \pm 1$ spherical harmonic functions.We therefore have non-zero solutions for all Q_l^m and R_l^m. Here we derive the expressions for Γ_1^0 and $\Gamma_1^{\pm 1}$. Beginning with Γ_1^0, one may easily compute $N_1^0 = \sqrt{3/4\pi}$ and $P_1^0 = \cos\theta$. Since $m = 0$, the integral in ϕ is identical to that in the isotropic case for both Q_1^0 and R_1^0. We can also use (A.14) to easily solve the integral in θ, with $x = \cos\theta$ and $a' = \cos\zeta$:

$$\begin{aligned} Q_1^0 &= \sqrt{3\pi}\int_0^{\pi} d\theta \sin\theta(1-\cos\theta)(1-\cos\theta\cos\zeta)\cos\theta \\ &= \sqrt{3\pi}\int_{-1}^{+1} dx[a'x^2 - x(a'+1)+1]x \qquad \text{(A.19)} \\ &= -2\sqrt{\frac{\pi}{3}}\alpha. \qquad \text{(A.20)} \end{aligned}$$

To evaluate R_1^0, we substitute $l = 1$ into Eq. (A.18)

$$\begin{aligned} R_1^0 &= -4\pi\sqrt{\frac{3}{4\pi}}\left[\beta\int_0^{\pi-\zeta} d\theta \frac{(1-\cos\theta)^2}{\sin\theta}\cos\theta \right. \\ &\quad \left. +\alpha\int_{\pi-\zeta}^{\pi} d\theta \sin\theta\cos\theta\right], \\ &= -2\sqrt{3\pi}\beta\left[\alpha + 4\ln\left(\sin\frac{\zeta}{2}\right)\right], \qquad \text{(A.21)} \end{aligned}$$

so we can finally write

$$^{(ab)}\Gamma_1^0 = -\frac{1}{2}\sqrt{\frac{\pi}{3}}\left\{\alpha + 3\beta\left[\alpha + 4\ln\left(\sin\frac{\zeta}{2}\right)\right]\right\}(1+\delta_{ab}). \qquad \text{(A.22)}$$

To evaluate ${}^{(ab)}\Gamma_1^1$, we calculate $N_1^1 = \sqrt{3/8\pi}$ and $P_1^1(\cos\theta) = -\sin\theta$ so that we can easily write

$$\begin{aligned} Q_1^1 &= \sqrt{\frac{3}{8\pi}}\int_0^\pi d\theta(-\sin^2\theta)(1-\cos\theta)\int_0^{2\pi} d\phi e^{i\phi}(1-\cos\zeta\cos\theta-\sin\zeta\sin\theta\cos\phi) \\ &= \pi\sqrt{\frac{3}{8\pi}}\sin\zeta\int_0^\pi d\theta\sin^3\theta(1-\cos\theta) \\ &= \sqrt{\frac{2\pi}{3}}\sin\zeta. \end{aligned} \tag{A.23}$$

Note that the solution of the integration in ϕ is valid for any l:

$$Q_l^1 = -\pi N_l^1\sin\zeta\int_0^\pi d\theta\sin^2\theta(1-\cos\theta)P_l^1(\cos\theta). \tag{A.24}$$

We now turn our attention to R_1^1 and simplify the expression by substituting

$$q = 1+\cos\theta\cos\zeta,$$

$$r = \sin\theta\sin\zeta,$$

noting that $\sqrt{q^2-r^2} = |\cos\theta+\cos\zeta|$. It follows that

$$R_1^1 = -2\sqrt{\frac{3}{8\pi}}\sin^2\zeta\int_0^\pi d\theta\sin\theta(1-\cos\theta)(-\sin\theta)I_1, \tag{A.25}$$

$$I_1 \equiv \int_0^{2\pi} d\phi\frac{\cos\phi\sin^2\phi}{q+r\cos\phi}. \tag{A.26}$$

$$= -\frac{\pi\left(-2q^3-r^2|\cos\theta+\cos\zeta|+2qr^2+2q^2|\cos\theta+\cos\zeta|\right)}{r^3|\cos\theta+\cos\zeta|}. \tag{A.27}$$

As before, the value of Eq. (A.27) depends on where we are evaluating the integral in θ: $\cos\theta+\cos\zeta$ is positive for $0 \le \theta \le \pi-\zeta$ and negative for $\pi-\zeta \le \theta \le \pi$.

We now factor Eq (A.27) considering $(\cos\theta + \cos\zeta) > 0$:

$$I_1 = -\frac{\pi[q-(\cos\theta+\cos\zeta)]^2}{r^3}, \tag{A.28}$$

$$= -\frac{\pi}{\sin\theta\sin\zeta}\frac{(1-\cos\theta)(1-\cos\zeta)}{(1+\cos\theta)(1+\cos\zeta)}. \tag{A.29}$$

The case where $(\cos\theta + \cos\zeta) < 0$ is analogous. The complete expression for I_1 is therefore

$$I_1 = -\frac{\pi}{\sin\theta\sin\zeta}\begin{cases} \frac{(1-\cos\theta)(1-\cos\zeta)}{(1+\cos\theta)(1+\cos\zeta)}, & 0<\theta<\pi-\zeta \\ \frac{(1+\cos\theta)(1+\cos\zeta)}{(1-\cos\theta)(1-\cos\zeta)}, & \pi-\zeta<\theta<\pi \end{cases} \tag{A.30}$$

Therefore, any R_l^1 can be written as:

$$\begin{aligned} R_l^1 = &+2\pi N_l^1\frac{\beta}{\alpha}\sin\zeta\int_0^{\pi-\zeta}d\theta\frac{(1-\cos\theta)^2}{1+\cos\theta}P_l^1(\cos\theta) \\ &+2\pi N_l^1\frac{\alpha}{\beta}\sin\zeta\int_{\pi-\zeta}^{\pi}d\theta(1+\cos\theta)P_l^1(\cos\theta)\,. \end{aligned} \tag{A.31}$$

For $m=1, l=1$, it is now straightforward to write

$$R_1^1 = -\frac{\beta}{\alpha}\sqrt{\frac{3\pi}{2}}\sin\zeta\int_0^{\pi-\zeta}d\theta\frac{(1-\cos\theta)^2\sin\theta}{1+\cos\theta}$$

$$- \frac{\alpha}{\beta}\sqrt{\frac{3\pi}{2}}\sin\zeta\int_{\pi-\zeta}^{\pi}d\theta\sin\theta(1+\cos\theta), \tag{A.32}$$

$$= 2\beta\sqrt{\frac{3\pi}{2}}\sin\zeta\left[1+\frac{4}{\alpha}\ln\left(\sin\frac{\zeta}{2}\right)\right]. \tag{A.33}$$

Combining Eqs(A.23) and (A.33) one finds the final expression for Γ_1^1:

$$^{(ab)}\Gamma_1^1 = \frac{1}{2}\sqrt{\frac{\pi}{6}}\sin\zeta\left\{1+3\beta\left[1+\frac{4}{\alpha}\ln\left(\sin\frac{\zeta}{2}\right)\right]\right\}(1+\delta_{ab}), \tag{A.34}$$

and recalling that $^{(ab)}\Gamma_l^{-m} = {}^{(ab)}\Gamma_l^m(-1)^m$, one obtains $^{(ab)}\Gamma_1^{-1} = -{}^{(ab)}\Gamma_1^1$.

A.1.3 Quadrupole Anisotropy

Quadrupole anisotropy is described in terms of the $l = 2, m = 0, \pm1, \pm2$ spherical harmonic functions. Two of these solutions are found immediately: since $l = 2$, $^{(ab)}\Gamma_2^{-m} = {}^{(ab)}\Gamma_2^m$. We now evaluate $^{(ab)}\Gamma_2^{|m|}$, beginning with $^{(ab)}\Gamma_2^0$, where $N_2^0 = \sqrt{5/4\pi}$ and $P_2^0 = 1/2(3\cos^2\theta - 1)$. Firstly we find Q_2^0 using (A.17) with $l = 2$

$$\begin{aligned} Q_2^0 &= \pi\sqrt{\frac{5}{4\pi}}\int_0^\pi d\theta\sin\theta(1-\cos\theta)(1-\cos\zeta\cos\theta)(3\cos^2\theta-1) \\ &= \frac{4}{3}\sqrt{\frac{\pi}{5}}\cos\zeta, \end{aligned} \tag{A.35}$$

and R_2^0 can be found with (A.18) with $l = 2$:

$$\begin{aligned} R_2^0 &= -2\pi\sqrt{\frac{5}{4\pi}}\beta\int_0^{\pi-\zeta}d\theta\frac{(1-\cos\theta)^2}{\sin\theta}(3\cos^2\theta-1) \\ &- 2\pi\sqrt{\frac{5}{4\pi}}\alpha\int_{\pi-\zeta}^{\pi}d\theta\sin\theta(3\cos^2\theta-1), \qquad \text{(A.36)} \\ &= \beta\sqrt{5\pi}\left[\cos^2\zeta+4\cos\zeta+3+8\ln\left(\sin\frac{\zeta}{2}\right)\right]. \qquad \text{(A.37)} \end{aligned}$$

Combining these solutions we obtain:

A. DERIVATION OF THE GENERALIZED OVERLAP REDUCTION FUNCTIONS

$$ {}^{(ab)}\Gamma_2^0 = \frac{1}{3}\sqrt{\frac{\pi}{5}}\left\{\cos\zeta + \frac{15\beta}{4}\left[\alpha(\cos\zeta+3) + 8\ln\left(\sin\frac{\zeta}{2}\right)\right]\right\}(1+\delta_{ab}). \tag{A.38} $$

Using analogous techniques, we can find an expression for Γ_2^1. Here $N_2^1 = \sqrt{5/24\pi}$ and $P_2^1 = -3\cos\theta\sin\theta$, so Q_2^1 is given by substituting $l = 2$ into Equation (A.24):

$$ \begin{aligned} Q_2^1 &= 3\pi\sqrt{\frac{5}{24\pi}}\sin\zeta\int_0^\pi d\theta\sin^3\theta\cos\theta(1-\cos\theta) && \text{(A.39)} \\ &= -\sqrt{\frac{2\pi}{15}}\sin\zeta. && \text{(A.40)} \end{aligned} $$

Equation (A.31) is again used with $l = 2$ to write R_2^1:

$$ \begin{aligned} R_2^1 &= -6\pi\sqrt{\frac{5}{24\pi}}\frac{\beta}{\alpha}\sin\zeta\int_0^{\pi-\zeta} d\theta\frac{(1-\cos\theta)^2\cos\theta\sin\theta}{1+\cos\theta} \\ &- 6\pi\sqrt{\frac{5}{24\pi}}\frac{\alpha}{\beta}\sin\zeta\int_{\pi-\zeta}^{\pi} d\theta(1+\cos\theta)\cos\theta\sin\theta && \text{(A.41)} \\ &= -\frac{2\beta}{\alpha}\sqrt{\frac{5\pi}{6}}\sin\zeta\left[\alpha(\cos\zeta+4) + 12\ln\left(\sin\frac{\zeta}{2}\right)\right]. && \text{(A.42)} \end{aligned} $$

Hence we write the final solution as:

$$ {}^{(ab)}\Gamma_2^1 = \frac{1}{4}\sqrt{\frac{2\pi}{15}}\sin\zeta\left\{5\cos^2\zeta + 15\cos\zeta - 21 - 60\frac{\beta}{\alpha}\ln\left(\sin\frac{\zeta}{2}\right)\right\}(1+\delta_{ab}). \tag{A.43} $$

Finally we write down the exact expression for ${}^{(ab)}\Gamma_2^2$. Recall that for $m = 2$, $Q_2^2 = 0$ as shown in the introduction to this appendix. Here $N_2^2 = \sqrt{5/96\pi}$ and $P_2^2 = 3\sin^2\theta$ and using q and r as previously defined we first write down the

integral I_2:

$$I_2 \equiv \int_0^{2\pi} d\phi \frac{\cos 2\phi \sin^2 \phi}{q + r\cos\phi}, \tag{A.44}$$

$$= \frac{2\pi(\cos\theta + \cos\zeta)^2}{r^4|\cos\theta + \cos\zeta|}[2q|\cos\theta + \cos\zeta| - (\cos\theta + \cos\zeta)^2 - q^2]. \tag{A.45}$$

This expression must be evaluated in 2 separate regimes, as before, where $\cos\theta + \cos\zeta$ is positive for $0 \leq \theta \leq \pi - \zeta$ and negative for $\pi - \zeta \leq \theta \leq \pi$, i.e.

$$I_2 = 2\pi \begin{cases} \frac{-(\cos\theta + \cos\zeta)}{(1+\cos\theta)^2(1+\cos\zeta)^2}, & 0 < \theta < \pi - \zeta \\ \frac{(\cos\theta + \cos\zeta)}{(1-\cos\theta)^2(1-\cos\zeta)^2}, & \pi - \zeta < \theta < \pi \end{cases} \tag{A.46}$$

Therefore:

$$\begin{aligned} {}^{(ab)}\Gamma_2^2 &= \frac{3}{4}\sqrt{\frac{5\pi}{6}} \sin^2\zeta \int_0^{\pi-\zeta} d\theta \frac{\sin^3\theta(1-\cos\theta)(\cos\theta + \cos\zeta)}{\alpha^2(1+\cos\theta)^2}(1+\delta_{ab}) \\ &- \frac{3}{4}\sqrt{\frac{5\pi}{6}} \sin^2\zeta \int_{\pi-\zeta}^{\pi} d\theta \frac{\sin^3\theta(\cos\theta + \cos\zeta)}{\beta^2(1-\cos\theta)}(1+\delta_{ab}), \\ &= -\frac{1}{4}\sqrt{\frac{5\pi}{6}}\frac{\beta}{\alpha}\left\{\alpha(\cos^2\zeta + 4\cos\zeta - 9) - 24\beta \ln\left(\sin\frac{\zeta}{2}\right)\right\}(1+\delta_{ab}) \end{aligned} \tag{A.47}$$

A. DERIVATION OF THE GENERALIZED OVERLAP REDUCTION FUNCTIONS

Appendix B

FEATURES OF THE OVERLAP REDUCTION FUNCTIONS

B.1 Strong pulsar-term effects

Stochastic GW background searches all assume that many GWs separate pulsar pairs from each other and the Earth. We can write this assumption mathematically as $fL \gg 1$, where f is the frequency of the GW background and L is the distance to the pulsar. However, when the pulsars are separated by a few radiation wavelengths or less, there is a coherent addition of the GW phase between neighbouring pulsars, cf. Figs 3.2, 3.3. In Chapter 3, we probed the strong pulsar term regime by fixing pulsar a and moving pulsar b radially by ζfL_a and along the z-axis by $\delta fL = fL_b - fL_a$. This geometry is illustrated in Fig 3.1. Some of the contour plots in Figs 3.2, 3.3 showed new and interesting behaviour in the strong pulsar term regime, including large fractional difference between the magnitude of the ORF with respect to the Earth-term-only ORF, for pulsars separated by

a few degrees, cf. Table 3.1.

Here we try to explain these features by giving an example of the interplay between the geometry of the pulsar-Earth system its alignment with the GW energy density decomposed over the basis of spherical harmonics. The doubling of the ORF at $\zeta = 0$ is a known feature, cf. Eq (3.12). In the following geometry, pulsar a is aligned with the z-axis.

Take for example the Y_2^0 spherical harmonic, see Fig B.1. In Fig B.1, we show that the Y_2^0 spherical harmonic has both positive and negative regions which contribute positively and negatively to the ORF respectively. The the product of the positive/negative correlation introduced by the pulsar term (which is in turn a function of the separation of the pulsars) and the sign of the spherical harmonic in a particular region of the sky gives the overall sign of the ORF in that region. By studying how the correlated phase changes interact with the distribution of the GW energy density, we will gain some insight into the general features of the strong pulsar-term regime.

First we examine how moving pulsar b in the z-direction affects the ORF in the strong pulsar term regime. When the pulsar pair is separated by $\delta f L \leq 0.25$ the pulsar terms introduce a positive correlated phase change. Since the pulsars are embedded in a Y_2^0-type GW background, sign of the correlation in the $\theta < \cos^{-1}(1/\sqrt{3})$ region is also positive. Therefore the sign of the ORF here is positive. In Fig B.1, this is denoted by [+,+].

The pulsar terms are again positively correlated when $0.75 < \delta f L(1 - cos\theta) < 1$. Moreover, when $\cos^{-1}(-1/\sqrt{3}) < \theta < \pi$, the contribution from the Y_2^0 distributed GW energy density is also positive.

When pulsar b is between 0.25 and 0.75 radiation wavelengths from a, the

pulsar term phases will be anti-correlated. However, this region coincides with the region where the GW energy density is also negative, and therefore the overall contribution to the ORF is positive. This explains why some large ORF values are observed for pulsars which are separated by a small $\delta f L$.

Analogous arguments hold when moving pulsar b radially, separating the pulsars by $\zeta f L_a$ radiation wavelengths. Similar arguments can also be made to explain the feature seen in the other anisotropic ORFs.

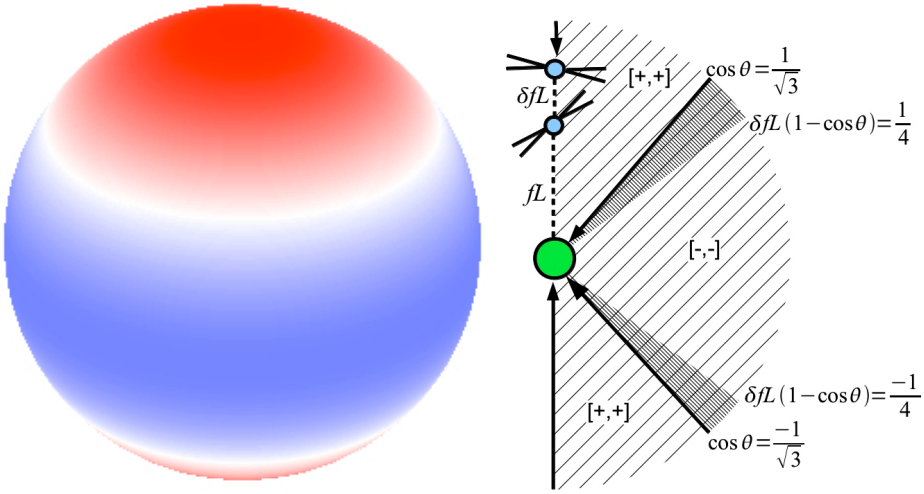

(a) The Y_2^0 spherical harmonic (b) Contributions to the ORF

Figure B.1: (a) The energy density distribution for Y_2^0. The red and blue regions are positive and negative, respectively. (b) The Earth (green) is at the center with the two pulsars above. The magnitude of the ${}^{(ab)}\Gamma_2^0(fL,\zeta)$ ORF is enhanced by small $0 < \delta f L \lesssim 1$ pulsar b displacements, over the $\delta f L = 0$ case. Going clockwise from the top, the arrows show the direction of GW propagation. The lighter shaded regions of the diagram show the regions of the sky from which the signal will contribute positively to the ORF. The darker shaded regions will contribute negatively to the ORF though their size and depend on $\delta f L$. The brackets indicate the sign of [pulsar term correlation, sign of the background energy density].

Bibliography

B. Allen and A. C. Ottewill. Detection of anisotropies in the gravitational-wave stochastic background. *Physical Review D*, 56:545–563, July 1997. doi: 10.1103/PhysRevD.56.545. 64, 65, 77, 107

B. Allen and J. D. Romano. Detecting a stochastic background of gravitational radiation: Signal processing strategies and sensitivities. *Physical Review D*, 59 (10):102001, May 1999. doi: 10.1103/PhysRevD.59.102001. 49

M. A. Alvarez, J. H. Wise, and T. Abel. Accretion onto the First Stellar-Mass Black Holes. *The Astrophysical Journal Letters*, 701:L133–L137, August 2009. doi: 10.1088/0004-637X/701/2/L133. 24

M. Anholm, S. Ballmer, J. D. E. Creighton, L. R. Price, and X. Siemens. Optimal strategies for gravitational wave stochastic background searches in pulsar timing data. *Physical Review D*, 79(8):084030, April 2009. doi: 10.1103/PhysRevD.79.084030. 39, 46, 49, 54, 74, 76, 78, 83, 85, 87, 96, 112, 137

T. A. Apostolatos, C. Cutler, G. J. Sussman, and K. S. Thorne. Spin-induced orbital precession and its modulation of the gravitational waveforms

from merging binaries. *Physical Review D*, 49:6274–6297, June 1994. doi: 10.1103/PhysRevD.49.6274. 123, 124, 127

G. Arfken. *Mathematical Methods for Physicists*. Academic, 3rd edition, 1985. 79

K. G. Arun, S. Babak, E. Berti, N. Cornish, C. Cutler, J. Gair, S. A. Hughes, B. R. Iyer, R. N. Lang, I. Mandel, E. K. Porter, B. S. Sathyaprakash, S. Sinha, A. M. Sintes, M. Trias, C. Van Den Broeck, and M. Volonteri. Massive black-hole binary inspirals: results from the LISA parameter estimation taskforce. *Classical and Quantum Gravity*, 26(9):094027, May 2009. doi: 10.1088/0264-9381/26/9/094027. 24

ATNF. Australia telescope national facility (atnf) pulsar catalogue. `http://www.atnf.csiro.au/people/pulsar/psrcat/`, March 2014. 94, 96, 110

W. Baade and F. Zwicky. On Super-novae. *Proceedings of the National Academy of Science*, 20:254–259, May 1934a. doi: 10.1073/pnas.20.5.254. 33

W. Baade and F. Zwicky. Cosmic Rays from Super-novae. *Proceedings of the National Academy of Science*, 20:259–263, May 1934b. doi: 10.1073/pnas.20.5.259. 33

S. Babak and A. Sesana. Resolving multiple supermassive black hole binaries with pulsar timing arrays. *Physical Review D*, 85(4):044034, February 2012. doi: 10.1103/PhysRevD.85.044034. 2, 63, 69, 119, 129

D. C. Backer, S. R. Kulkarni, C. Heiles, M. M. Davis, and W. M. Goss. A mil-

lisecond pulsar. *Nature*, 300:615–618, December 1982. doi: 10.1038/300615a0. 35

E. D. Barr, D. J. Champion, M. Kramer, R. P. Eatough, P. C. C. Freire, R. Karuppusamy, K. J. Lee, J. P. W. Verbiest, C. G. Bassa, A. G. Lyne, B. Stappers, D. R. Lorimer, and B. Klein. The Northern High Time Resolution Universe pulsar survey - I. Setup and initial discoveries. *Monthly Notices of the Royal Astronomical Society*, 435:2234–2245, November 2013. doi: 10.1093/mnras/stt1440. 94

S. V. W. Beckwith, M. Stiavelli, A. M. Koekemoer, J. A. R. Caldwell, H. C. Ferguson, R. Hook, R. A. Lucas, L. E. Bergeron, M. Corbin, S. Jogee, N. Panagia, M. Robberto, P. Royle, R. S. Somerville, and M. Sosey. The Hubble Ultra Deep Field. *The Astronomical Journal*, 132:1729–1755, November 2006. doi: 10.1086/507302. 28

E. Berti and M. Volonteri. Cosmological Black Hole Spin Evolution by Mergers and Accretion. *The Astrophysical Journal*, 684:822–828, September 2008. doi: 10.1086/590379. 119

BICEP2 Collaboration, P. A. R Ade, R. W. Aikin, D. Barkats, S. J. Benton, C. A. Bischoff, J. J. Bock, J. A. Brevik, I. Buder, E. Bullock, C. D. Dowell, L. Duband, J. P. Filippini, S. Fliescher, S. R. Golwala, M. Halpern, M. Hasselfield, S. R. Hildebrandt, G. C. Hilton, V. V. Hristov, K. D. Irwin, K. S. Karkare, J. P. Kaufman, B. G. Keating, S. A. Kernasovskiy, J. M. Kovac, C. L. Kuo, E. M. Leitch, M. Lueker, P. Mason, C. B. Netterfield, H. T. Nguyen, R. O'Brient, R. W. Ogburn, IV, A. Orlando, C. Pryke, C. D. Reintsema,

S. Richter, R. Schwarz, C. D. Sheehy, Z. K. Staniszewski, R. V. Sudiwala, G. P. Teply, J. E. Tolan, A. D. Turner, A. G. Vieregg, C. L. Wong, and K. W. Yoon. BICEP2 I: Detection Of B-mode Polarization at Degree Angular Scales. *ArXiv e-prints*, March 2014. 3, 4, 92

L. Blanchet. Gravitational Radiation from Post-Newtonian Sources and Inspiralling Compact Binaries. *Living Reviews in Relativity*, 9:4, June 2006. doi: 10.12942/lrr-2006-4. 121, 123

L. Blanchet. Gravitational Radiation from Post-Newtonian Sources and Inspiralling Compact Binaries. *Living Reviews in Relativity*, 17:2, February 2014. doi: 10.12942/lrr-2014-2. 21, 22

L. Blanchet, T. Damour, B. R. Iyer, C. M. Will, and A. G. Wiseman. Gravitational-Radiation Damping of Compact Binary Systems to Second Post-Newtonian Order. *Physical Review Letters*, 74:3515–3518, May 1995. doi: 10.1103/PhysRevLett.74.3515. 21

L. Blanchet, A. Buonanno, and G. Faye. Higher-order spin effects in the dynamics of compact binaries. II. Radiation field. *Physical Review D*, 74(10):104034, November 2006. doi: 10.1103/PhysRevD.74.104034. 123

C. Bona, J. Massó, E. Seidel, and J. Stela. New Formalism for Numerical Relativity. *Physical Review Letters*, 75:600–603, July 1995. doi: 10.1103/PhysRevLett.75.600. 21

L. G. Book and É. É. Flanagan. Astrometric effects of a stochastic gravitational wave background. *Physical Review D*, 83(2):024024, January 2011. doi: 10.1103/PhysRevD.83.024024. 46

A. Buonanno, B. R. Iyer, E. Ochsner, Y. Pan, and B. S. Sathyaprakash. Comparison of post-Newtonian templates for compact binary inspiral signals in gravitational-wave detectors. *Physical Review D*, 80(8):084043, October 2009. doi: 10.1103/PhysRevD.80.084043. 21, 22

M. Burgay, N. D'Amico, A. Possenti, R. N. Manchester, A. G. Lyne, B. C. Joshi, M. A. McLaughlin, M. Kramer, J. M. Sarkissian, F. Camilo, V. Kalogera, C. Kim, and D. R. Lorimer. An increased estimate of the merger rate of double neutron stars from observations of a highly relativistic system. *Nature*, 426:531–533, December 2003. doi: 10.1038/nature02124. 3

J. Centrella, J. G. Baker, B. J. Kelly, and J. R. van Meter. Black-hole binaries, gravitational waves, and numerical relativity. *Reviews of Modern Physics*, 82: 3069–3119, October 2010. doi: 10.1103/RevModPhys.82.3069. 21

J Chadwick. Possible existence of a neutron. *Nature*, 129:312, 1932. doi: doi: 10.1038/129312a0. 33

C. J. Conselice, M. A. Bershady, M. Dickinson, and C. Papovich. A Direct Measurement of Major Galaxy Mergers at z¡3. *The Astronomical Journal*, 126: 1183–1207, September 2003. doi: 10.1086/377318. 28

N. J. Cornish. Making maps with LISA. *Classical and Quantum Gravity*, 19: 1279–1283, April 2002. doi: 10.1088/0264-9381/19/7/306. 64

N. J. Cornish and A. Sesana. Pulsar timing array analysis for black hole backgrounds. *Classical and Quantum Gravity*, 30(22):224005, November 2013. doi: 10.1088/0264-9381/30/22/224005. 64

C. Cutler and É. E. Flanagan. Gravitational waves from merging compact binaries: How accurately can one extract the binary's parameters from the inspiral waveform? *Physical Review D*, 49:2658–2697, March 1994. doi: 10.1103/PhysRevD.49.2658. 21

T. Damour, B. R. Iyer, and A. Nagar. Improved resummation of post-Newtonian multipolar waveforms from circularized compact binaries. *Physical Review D*, 79(6):064004, March 2009. doi: 10.1103/PhysRevD.79.064004. 21

A. T. Deller, J. P. W. Verbiest, S. J. Tingay, and M. Bailes. Extremely High Precision VLBI Astrometry of PSR J0437-4715 and Implications for Theories of Gravity. *The Astrophysical Journal Letters*, 685:L67–L70, September 2008. doi: 10.1086/592401. 121

P. Demorest, J. Lazio, A. Lommen, A. Archibald, Z. Arzoumanian, D. Backer, J. Cordes, P. Demorest, R. Ferdman, P. Freire, M. Gonzalez, R. Jenet, V. Kaspi, V. Kondratiev, J. Lazio, A. Lommen, D. Lorimer, R. Lynch, M. McLaughlin, D. Nice, S. Ransom, R. Shannon, X. Siemens, I. Stairs, D. Stinebring, D. Reitze, D. Shoemaker, S. Whitcomb, and R. Weiss. Gravitational Wave Astronomy Using Pulsars: Massive Black Hole Mergers and the Early Universe. In *astro2010: The Astronomy and Astrophysics Decadal Survey*, volume 2010 of *Astronomy*, page 64, 2009. 34

P. B. Demorest, R. D. Ferdman, M. E. Gonzalez, D. Nice, S. Ransom, I. H. Stairs, Z. Arzoumanian, A. Brazier, S. Burke-Spolaor, S. J. Chamberlin, J. M. Cordes, J. Ellis, L. S. Finn, P. Freire, S. Giampanis, F. Jenet, V. M. Kaspi, J. Lazio, A. N. Lommen, M. McLaughlin, N. Palliyaguru, D. Perrodin, R. M.

Shannon, X. Siemens, D. Stinebring, J. Swiggum, and W. W. Zhu. Limits on the Stochastic Gravitational Wave Background from the North American Nanohertz Observatory for Gravitational Waves. *The Astrophysical Journal*, 762:94, January 2013. doi: 10.1088/0004-637X/762/2/94. 2, 63, 118

S. Detweiler. Pulsar timing measurements and the search for gravitational waves. *The Astrophysical Journal*, 234:1100–1104, December 1979. doi: 10.1086/157593. 1, 33, 39, 62, 92, 118, 120, 122

S. G. Djorgovski, M. Volonteri, V. Springel, V. Bromm, and G. Meylan. The Origins and the Early Evolution of Quasars and Supermassive Black Holes. In H. Kleinert, R. T. Jantzen, and R. Ruffini, editors, *The Eleventh Marcel Grossmann Meeting On Recent Developments in Theoretical and Experimental General Relativity, Gravitation and Relativistic Field Theories*, pages 340–367, September 2008. doi: 10.1142/9789812834300_0018. 24

M. Dotti, M. Volonteri, A. Perego, M. Colpi, M. Ruszkowski, and F. Haardt. Dual black holes in merger remnants - II. Spin evolution and gravitational recoil. *Monthly Notices of the Royal Astronomical Society*, 402:682–690, February 2010. doi: 10.1111/j.1365-2966.2009.15922.x. 119

J. A. Ellis, F. A. Jenet, and M. A. McLaughlin. Practical Methods for Continuous Gravitational Wave Detection Using Pulsar Timing Data. *The Astrophysical Journal*, 753:96, July 2012a. doi: 10.1088/0004-637X/753/2/96. 2, 63, 69, 119

J. A. Ellis, X. Siemens, and J. D. E. Creighton. Optimal Strategies for Continuous Gravitational Wave Detection in Pulsar Timing Arrays. *The Astrophysical*

Journal, 756:175, September 2012b. doi: 10.1088/0004-637X/756/2/175. 2, 63, 69, 119

EPTA. http://www.epta.eu.org/, 2013. 76

F. B. Estabrook and H. D. Wahlquist. Response of Doppler spacecraft tracking to gravitational radiation. *General Relativity and Gravitation*, 6:439–447, October 1975. doi: 10.1007/BF00762449. 1, 33, 62, 92, 118, 120, 122

Dan Falkowski. Resonaances blog. http://resonaances.blogspot.co.nz/2014/05/is-bicep-wrong.html, 2014. the title is really spelled with two a's. 4

R. D. Ferdman, R. van Haasteren, C. G. Bassa, M. Burgay, I. Cognard, A. Corongiu, N. D'Amico, G. Desvignes, J. W. T. Hessels, G. H. Janssen, A. Jessner, C. Jordan, R. Karuppusamy, E. F. Keane, M. Kramer, K. Lazaridis, Y. Levin, A. G. Lyne, M. Pilia, A. Possenti, M. Purver, B. Stappers, S. Sanidas, R. Smits, and G. Theureau. The European Pulsar Timing Array: current efforts and a LEAP toward the future. *Classical and Quantum Gravity*, 27(8):084014, April 2010. doi: 10.1088/0264-9381/27/8/084014. 2, 33, 62, 93, 118

L. Ferrarese and H. Ford. Supermassive Black Holes in Galactic Nuclei: Past, Present and Future Research. *Space Science Reviews*, 116:523–624, February 2005. doi: 10.1007/s11214-005-3947-6. 24

L. S. Finn, S. L. Larson, and J. D. Romano. Detecting a stochastic gravitational-wave background: The overlap reduction function. *Physical Review D*, 79(6): 062003, March 2009. doi: 10.1103/PhysRevD.79.062003. 47

É. É. Flanagan and S. A. Hughes. The basics of gravitational wave theory. *New Journal of Physics*, 7:204, September 2005. doi: 10.1088/1367-2630/7/1/204. 7, 9, 11, 13

C. F. Gammie, S. L. Shapiro, and J. C. McKinney. Black Hole Spin Evolution. *The Astrophysical Journal*, 602:312–319, February 2004. doi: 10.1086/380996. 119

R. Genzel, F. Eisenhauer, and S. Gillessen. The Galactic Center massive black hole and nuclear star cluster. *Reviews of Modern Physics*, 82:3121–3195, October 2010. doi: 10.1103/RevModPhys.82.3121. 24

A. M. Ghez, S. Salim, S. D. Hornstein, A. Tanner, J. R. Lu, M. Morris, E. E. Becklin, and G. Duchêne. Stellar Orbits around the Galactic Center Black Hole. *The Astrophysical Journal*, 620:744–757, February 2005. doi: 10.1086/427175. 24

L. P. Grishchuk. Amplification of gravitational waves in an isotropic universe. *Soviet Journal of Experimental and Theoretical Physics*, 40:409, September 1975. 33

A. H. Guth. Inflationary universe: A possible solution to the horizon and flatness problems. *Physical Review D*, 23:347–356, January 1981. doi: 10.1103/PhysRevD.23.347. 4

M. G. Haehnelt and M. J. Rees. The formation of nuclei in newly formed galaxies and the evolution of the quasar population. *Monthly Notices of the Royal Astronomical Society*, 263:168–178, July 1993. 25

D. Hanson, S. Hoover, A. Crites, P. A. R. Ade, K. A. Aird, J. E. Austermann, J. A. Beall, A. N. Bender, B. A. Benson, L. E. Bleem, J. J. Bock, J. E. Carlstrom, C. L. Chang, H. C. Chiang, H.-M. Cho, A. Conley, T. M. Crawford, T. de Haan, M. A. Dobbs, W. Everett, J. Gallicchio, J. Gao, E. M. George, N. W. Halverson, N. Harrington, J. W. Henning, G. C. Hilton, G. P. Holder, W. L. Holzapfel, J. D. Hrubes, N. Huang, J. Hubmayr, K. D. Irwin, R. Keisler, L. Knox, A. T. Lee, E. Leitch, D. Li, C. Liang, D. Luong-Van, G. Marsden, J. J. McMahon, J. Mehl, S. S. Meyer, L. Mocanu, T. E. Montroy, T. Natoli, J. P. Nibarger, V. Novosad, S. Padin, C. Pryke, C. L. Reichardt, J. E. Ruhl, B. R. Saliwanchik, J. T. Sayre, K. K. Schaffer, B. Schulz, G. Smecher, A. A. Stark, K. T. Story, C. Tucker, K. Vanderlinde, J. D. Vieira, M. P. Viero, G. Wang, V. Yefremenko, O. Zahn, and M. Zemcov. Detection of B-Mode Polarization in the Cosmic Microwave Background with Data from the South Pole Telescope. *Physical Review Letters*, 111(14):141301, October 2013. doi: 10.1103/PhysRevLett.111.141301. 4

S. W. Hawking and W. Israel. *300 Years of Gravitation*. Cambridge University Press, 1987. 7, 12

R. W. Hellings and G. S. Downs. Upper limits on the isotropic gravitational radiation background from pulsar timing analysis. *The Astrophysical Journal Letters*, 265:L39–L42, February 1983. doi: 10.1086/183954. 2, 50, 63, 92, 97, 118, 137

A. Hewish, S. J. Bell, J. D. H. Pilkington, P. F. Scott, and R. A. Collins. Observation of a Rapidly Pulsating Radio Source. *Nature*, 217:709–713, February 1968. doi: 10.1038/217709a0. 34

G. Hobbs, A. Archibald, Z. Arzoumanian, D. Backer, M. Bailes, N. D. R. Bhat, M. Burgay, S. Burke-Spolaor, D. Champion, I. Cognard, W. Coles, J. Cordes, P. Demorest, G. Desvignes, R. D. Ferdman, L. Finn, P. Freire, M. Gonzalez, J. Hessels, A. Hotan, G. Janssen, F. Jenet, A. Jessner, C. Jordan, V. Kaspi, M. Kramer, V. Kondratiev, J. Lazio, K. Lazaridis, K. J. Lee, Y. Levin, A. Lommen, D. Lorimer, R. Lynch, A. Lyne, R. Manchester, M. McLaughlin, D. Nice, S. Oslowski, M. Pilia, A. Possenti, M. Purver, S. Ransom, J. Reynolds, S. Sanidas, J. Sarkissian, A. Sesana, R. Shannon, X. Siemens, I. Stairs, B. Stappers, D. Stinebring, G. Theureau, R. van Haasteren, W. van Straten, J. P. W. Verbiest, D. R. B. Yardley, and X. P. You. The International Pulsar Timing Array project: using pulsars as a gravitational wave detector. *Classical and Quantum Gravity*, 27(8):084013, April 2010. doi: 10.1088/0264-9381/27/8/084013. 2, 33, 62, 93, 118

S. A. Hughes and R. D. Blandford. Black Hole Mass and Spin Coevolution by Mergers. *The Astrophysical Journal Letters*, 585:L101–L104, March 2003. doi: 10.1086/375495. 119

R. A. Hulse and J. H. Taylor. Discovery of a pulsar in a binary system. *The Astrophysical Journal Letters*, 195:L51–L53, January 1975. doi: 10.1086/181708. 2, 92

IPTA. International pulsar timing array mock data challenge 1. `http://www.ipta4gw.org/?page_id=214`, 2012. 110

A. H. Jaffe and D. C. Backer. Gravitational Waves Probe the Coalescence Rate of

Massive Black Hole Binaries. *The Astrophysical Journal*, 583:616–631, February 2003. doi: 10.1086/345443. 2, 62, 92, 118

F. Jenet, L. S. Finn, J. Lazio, A. Lommen, M. McLaughlin, I. Stairs, D. Stinebring, J. Verbiest, A. Archibald, Z. Arzoumanian, D. Backer, J. Cordes, P. Demorest, R. Ferdman, P. Freire, M. Gonzalez, V. Kaspi, V. Kondratiev, D. Lorimer, R. Lynch, D. Nice, S. Ransom, R. Shannon, and X. Siemens. The North American Nanohertz Observatory for Gravitational Waves. *ArXiv e-prints*, September 2009. 2, 33, 62, 93, 118

F. A. Jenet, A. Lommen, S. L. Larson, and L. Wen. Constraining the Properties of Supermassive Black Hole Systems Using Pulsar Timing: Application to 3C 66B. *The Astrophysical Journal*, 606:799–803, May 2004. doi: 10.1086/383020. 2, 63, 119, 126

F. A. Jenet, G. B. Hobbs, W. van Straten, R. N. Manchester, M. Bailes, J. P. W. Verbiest, R. T. Edwards, A. W. Hotan, J. M. Sarkissian, and S. M. Ord. Upper Bounds on the Low-Frequency Stochastic Gravitational Wave Background from Pulsar Timing Observations: Current Limits and Future Prospects. *The Astrophysical Journal*, 653:1571–1576, December 2006. doi: 10.1086/508702. 2, 33, 63, 118

M. Kamionkowski, A. Kosowsky, and A. Stebbins. Statistics of cosmic microwave background polarization. *Physical Review D*, 55:7368–7388, June 1997. doi: 10.1103/PhysRevD.55.7368. 136

M. J. Keith, A. Jameson, W. van Straten, M. Bailes, S. Johnston, M. Kramer, A. Possenti, S. D. Bates, N. D. R. Bhat, M. Burgay, S. Burke-Spolaor,

N. D'Amico, L. Levin, P. L. McMahon, S. Milia, and B. W. Stappers. The High Time Resolution Universe Pulsar Survey - I. System configuration and initial discoveries. *Monthly Notices of the Royal Astronomical Society*, 409: 619–627, December 2010. doi: 10.1111/j.1365-2966.2010.17325.x. 94

L. E. Kidder. Coalescing binary systems of compact objects to (post)$^{5/2}$-Newtonian order. V. Spin effects. *Physical Review D*, 52:821–847, July 1995. doi: 10.1103/PhysRevD.52.821. 124

L. E. Kidder, C. M. Will, and A. G. Wiseman. Spin effects in the inspiral of coalescing compact binaries. *Physical Review D*, 47:4183, May 1993. doi: 10.1103/PhysRevD.47.R4183. 123

M. Kidger, L. Takalo, and A. Sillanpaa. A new analysis of the 11-year period in OJ287 - Confirmation of its existence. *Astronomy and Astrophysics*, 264: 32–36, October 1992. 25

A. King. Black Holes, Galaxy Formation, and the M_{BH}-σ Relation. *The Astrophysical Journal Letters*, 596:L27–L29, October 2003. doi: 10.1086/379143. 25

S. M. Koushiappas and A. R. Zentner. Testing Models of Supermassive Black Hole Seed Formation through Gravity Waves. *The Astrophysical Journal*, 639: 7–22, March 2006. doi: 10.1086/499325. 63, 119

M Kramer and N Wex. TOPICAL REVIEW: The double pulsar system: a unique laboratory for gravity. *Classical and Quantum Gravity*, 26(7):073001, April 2009. doi: 10.1088/0264-9381/26/7/073001. 3, 34, 92

M. Kramer, I. H. Stairs, R. N. Manchester, M. A. McLaughlin, A. G. Lyne, R. D. Ferdman, M. Burgay, D. R. Lorimer, A. Possenti, N. D'Amico, J. M. Sarkissian, G. B. Hobbs, J. E. Reynolds, P. C. C. Freire, and F. Camilo. Tests of General Relativity from Timing the Double Pulsar. *Science*, 314:97–102, October 2006. doi: 10.1126/science.1132305. 34, 92

S. Kuroyanagi, K. Miyamoto, T. Sekiguchi, K. Takahashi, and J. Silk. Forecast constraints on cosmic strings from future CMB, pulsar timing, and gravitational wave direct detection experiments. *Physical Review D*, 87(2):023522, January 2013. doi: 10.1103/PhysRevD.87.023522. 62, 93

T. J. W. Lazio. The Square Kilometre Array pulsar timing array. *Classical and Quantum Gravity*, 30(22):224011, November 2013. doi: 10.1088/0264-9381/30/22/224011. 94

K. J. Lee, N. Wex, M. Kramer, B. W. Stappers, C. G. Bassa, G. H. Janssen, R. Karuppusamy, and R. Smits. Gravitational wave astronomy of single sources with a pulsar timing array. *Monthly Notices of the Royal Astronomical Society*, 414:3251–3264, July 2011. doi: 10.1111/j.1365-2966.2011.18622.x. 2, 63, 119, 121, 126, 129

L. Lentati, P. Alexander, M. P. Hobson, S. Taylor, J. Gair, S. T. Balan, and R. van Haasteren. Hyper-efficient model-independent Bayesian method for the analysis of pulsar timing data. *Physical Review D*, 87(10):104021, May 2013. doi: 10.1103/PhysRevD.87.104021. 136

A. D. Linde. A new inflationary universe scenario: A possible solution of the horizon, flatness, homogeneity, isotropy and primordial monopole problems.

Physics Letters B, 108:389–393, February 1982. doi: 10.1016/0370-2693(82)91219-9. 4

K. Liu, J. P. W. Verbiest, M. Kramer, B. W. Stappers, W. van Straten, and J. M. Cordes. Prospects for high-precision pulsar timing. *Monthly Notices of the Royal Astronomical Society*, 417:2916–2926, November 2011. doi: 10.1111/j.1365-2966.2011.19452.x. 2, 118

A. N. Lommen and D. C. Backer. Using Pulsars to Detect Massive Black Hole Binaries via Gravitational Radiation: Sagittarius A* and Nearby Galaxies. *The Astrophysical Journal*, 562:297–302, November 2001. doi: 10.1086/323491. 126

D. R. Lorimer. Binary and Millisecond Pulsars. *Living Reviews in Relativity*, 11:8, November 2008. doi: 10.12942/lrr-2008-8. 38

D. R. Lorimer and M. Kramer. *Handbook of Pulsar Astronomy*. Cambridge University Press, October 2012. 35, 38

A. G. Lyne, M. Burgay, M. Kramer, A. Possenti, R. N. Manchester, F. Camilo, M. A. McLaughlin, D. R. Lorimer, N. D'Amico, B. C. Joshi, J. Reynolds, and P. C. C. Freire. A Double-Pulsar System: A Rare Laboratory for Relativistic Gravity and Plasma Physics. *Science*, 303:1153–1157, February 2004a. doi: 10.1126/science.1094645. 3

A. G. Lyne, M. Burgay, M. Kramer, A. Possenti, R. N. Manchester, F. Camilo, M. A. McLaughlin, D. R. Lorimer, N. D'Amico, B. C. Joshi, J. Reynolds, and P. C. C. Freire. A Double-Pulsar System: A Rare Laboratory for Relativistic Gravity and Plasma Physics. *Science*, 303:1153–1157, February 2004b. doi: 10.1126/science.1094645. 34

M. Maggiore. Gravitational wave experiments and early universe cosmology. *Physics Reports*, 331:283–367, July 2000. doi: 10.1016/S0370-1573(99)00102-7. 33

M. Maggiore. *Gravitational Waves: Theory and experiments*, volume 1 of *Gravitational Waves*. Oxford University Press, 2007. ISBN 9780198570745. URL http://books.google.co.uk/books?id=AqVpQgAACAAJ. 37, 41

J. Magorrian, S. Tremaine, D. Richstone, R. Bender, G. Bower, A. Dressler, S. M. Faber, K. Gebhardt, R. Green, C. Grillmair, J. Kormendy, and T. Lauer. The Demography of Massive Dark Objects in Galaxy Centers. *The Astronomical Journal*, 115:2285–2305, June 1998. doi: 10.1086/300353. 24

R. K. Malbon, C. M. Baugh, C. S. Frenk, and C. G. Lacey. Black hole growth in hierarchical galaxy formation. *Monthly Notices of the Royal Astronomical Society*, 382:1394–1414, December 2007. doi: 10.1111/j.1365-2966.2007.12317.x. 63, 119

D. Merritt and R. D. Ekers. Tracing Black Hole Mergers Through Radio Lobe Morphology. *Science*, 297:1310–1313, August 2002. doi: 10.1126/science.1074688. 119

C. M. F. Mingarelli, K. Grover, T. Sidery, R. J. E. Smith, and A. Vecchio. Observing the Dynamics of Supermassive Black Hole Binaries with Pulsar Timing Arrays. *Physical Review Letters*, 109(8):081104, August 2012. doi: 10.1103/PhysRevLett.109.081104. i, ii, 117

C. M. F. Mingarelli, T. Sidery, I. Mandel, and A. Vecchio. Characterizing gravitational wave stochastic background anisotropy with pulsar timing arrays.

Physical Review D, 88(6):062005, September 2013. doi: 10.1103/PhysRevD.88.062005. i, ii, 54, 61, 94, 96, 98, 102, 107, 112, 113, 135, 137, 138

C. W. Misner, K. S. Thorne, and J. A. Wheeler. *Gravitation*. W. H. Freeman and Company, 1973. 7, 9, 12, 13, 15, 119

R. Nan. Introduction to FAST: five hundred meter Aperture Spherical radio Telescope. In *Society of Photo-Optical Instrumentation Engineers (SPIE) Conference Series*, volume 7012 of *Society of Photo-Optical Instrumentation Engineers (SPIE) Conference Series*, August 2008. doi: 10.1117/12.791288. 94

Nobelprize.org. The nobel prize in physics 1974. http://www.nobelprize.org/nobel_prizes/physics/laureates/1974/, 1974. The Nobel Prize in Physics 1974 was awarded jointly to Sir Martin Ryle and Antony Hewish "for their pioneering research in radio astrophysics: Ryle for his observations and inventions, in particular of the aperture synthesis technique, and Hewish for his decisive role in the discovery of pulsars". 34

Nobelprize.org. The nobel prize in physics 1993. http://www.nobelprize.org/nobel_prizes/physics/laureates/1993/, 1993. The Nobel Prize in Physics 1993 was awarded jointly to Russell A. Hulse and Joseph H. Taylor Jr. "for the discovery of a new type of pulsar, a discovery that has opened up new possibilities for the study of gravitation". 3

NRAO. Pulsar timing. http://www.cv.nrao.edu/course/astr534/PulsarTiming.html, May 2014. 37

J. R. Oppenheimer and G. M. Volkoff. On Massive Neutron Cores. *Physical Review*, 55:374–381, February 1939. doi: 10.1103/PhysRev.55.374. 33

P. J. E. Peebles. Large-scale background temperature and mass fluctuations due to scale-invariant primeval perturbations. *The Astrophysical Journal Letters*, 263:L1–L5, December 1982. doi: 10.1086/183911. 25

A. Perego, M. Dotti, M. Colpi, and M. Volonteri. Mass and spin co-evolution during the alignment of a black hole in a warped accretion disc. *Monthly Notices of the Royal Astronomical Society*, 399:2249–2263, November 2009. doi: 10.1111/j.1365-2966.2009.15427.x. 119

D. Perrodin, F. Jenet, A. Lommen, L. Finn, P. Demorest, R. Ferdman, M. Gonzalez, D. Nice, S. Ransom, and I. Stairs. Timing Noise Analysis of NANOGrav Pulsars. *ArXiv e-prints*, November 2013. 38

A. Petiteau, S. Babak, A. Sesana, and M. de Araújo. Resolving multiple supermassive black hole binaries with pulsar timing arrays. II. Genetic algorithm implementation. *Physical Review D*, 87(6):064036, March 2013. doi: 10.1103/PhysRevD.87.064036. 69

E. S. Phinney. A Practical Theorem on Gravitational Wave Backgrounds. *ArXiv Astrophysics e-prints*, August 2001. 29, 30, 32

Planck Collaboration, P. A. R. Ade, N. Aghanim, C. Armitage-Caplan, M. Arnaud, M. Ashdown, F. Atrio-Barandela, J. Aumont, C. Baccigalupi, A. J. Banday, and et al. Planck 2013 results. XXII. Constraints on inflation. *ArXiv e-prints*, March 2013. 4

E. Poisson and C. M. Will. Gravitational waves from inspiraling compact binaries: Parameter estimation using second-post-Newtonian waveforms. *Physical Review D*, 52:848–855, July 1995. doi: 10.1103/PhysRevD.52.848. 21

F. Pretorius. Evolution of Binary Black-Hole Spacetimes. *Physical Review Letters*, 95(12):121101, September 2005. doi: 10.1103/PhysRevLett.95.121101. 21

D. Psaltis. Probes and Tests of Strong-Field Gravity with Observations in the Electromagnetic Spectrum. *Living Reviews in Relativity*, 11:9, November 2008. doi: 10.12942/lrr-2008-9. 119

M. S. Pshirkov and A. V. Tuntsov. Local constraints on cosmic string loops from photometry and pulsar timing. *Physical Review D*, 81(8):083519, April 2010. doi: 10.1103/PhysRevD.81.083519. 62, 93

M. Rajagopal and R. W. Romani. Ultra–Low-Frequency Gravitational Radiation from Massive Black Hole Binaries. *The Astrophysical Journal*, 446:543, June 1995. doi: 10.1086/175813. 2, 32, 62, 93, 118

V. Ravi, J. S. B. Wyithe, G. Hobbs, R. M. Shannon, R. N. Manchester, D. R. B. Yardley, and M. J. Keith. Does a "Stochastic" Background of Gravitational Waves Exist in the Pulsar Timing Band? *The Astrophysical Journal*, 761:84, December 2012. doi: 10.1088/0004-637X/761/2/84. 64

J. A. Regan and M. G. Haehnelt. Pathways to massive black holes and compact star clusters in pre-galactic dark matter haloes with virial temperatures greater than 10000K. *Monthly Notices of the Royal Astronomical Society*, 396:343–353, June 2009. doi: 10.1111/j.1365-2966.2009.14579.x. 24

C. Roedig, J. H. Krolik, and M. C. Miller. Observational Signatures of Binary Supermassive Black Holes. *The Astrophysical Journal*, 785:115, April 2014. doi: 10.1088/0004-637X/785/2/115. 25

BIBLIOGRAPHY

M. E. Rose. *Elementary Theory of Angular Momentum*. Wiley, 1957. 79, 80

S. A. Sanidas, R. A. Battye, and B. W. Stappers. Constraints on cosmic string tension imposed by the limit on the stochastic gravitational wave background from the European Pulsar Timing Array. *Physical Review D*, 85(12):122003, June 2012. doi: 10.1103/PhysRevD.85.122003. 33, 62, 93

M. V. Sazhin. Opportunities for detecting ultralong gravitational waves. *Soviet Astronomy*, 22:36–38, February 1978. 1, 33, 62, 92, 118, 120, 122

B. F Schutz and F. Ricci. Gravitational Waves, Sources, and Detectors. *ArXiv e-prints*, May 1999. 82 pages, 9 figures, lecture notes from 1999, not posted to ArXiV at the time because they exceeded the article/figure size limits; Schutz, B. F.; Ricci, F.: Gravitational Waves, Sources and Detectors. In: Gravitational Waves, Ciufolini, I, et al, eds. (Institute of Physics, Bristol, 2001). 7, 12

A. Sesana. A Practical Guide to the Massive Black Hole Cosmic History. *Advances in Astronomy*, 2012, 2012. doi: 10.1155/2012/805402. 93, 118

A. Sesana. Systematic investigation of the expected gravitational wave signal from supermassive black hole binaries in the pulsar timing band. *Monthly Notices of the Royal Astronomical Society*, 433:L1–L5, June 2013. doi: 10.1093/mnrasl/slt034. 62, 63, 94, 96

A. Sesana and A. Vecchio. Measuring the parameters of massive black hole binary systems with pulsar timing array observations of gravitational waves. *Physical Review D*, 81(10):104008–+, May 2010. doi: 10.1103/PhysRevD.81.104008. 2, 63, 119, 120, 123, 126, 129

A. Sesana, F. Haardt, P. Madau, and M. Volonteri. Low-Frequency Gravitational Radiation from Coalescing Massive Black Hole Binaries in Hierarchical Cosmologies. *The Astrophysical Journal*, 611:623–632, August 2004. doi: 10.1086/422185. 2, 24, 118

A. Sesana, M. Volonteri, and F. Haardt. The imprint of massive black hole formation models on the LISA data stream. *Monthly Notices of the Royal Astronomical Society*, 377:1711–1716, June 2007. doi: 10.1111/j.1365-2966.2007.11734.x. 24

A. Sesana, A. Vecchio, and C. N. Colacino. The stochastic gravitational-wave background from massive black hole binary systems: implications for observations with Pulsar Timing Arrays. *Monthly Notices of the Royal Astronomical Society*, 390:192–209, October 2008. doi: 10.1111/j.1365-2966.2008.13682.x. 2, 27, 62, 63, 71, 72, 93, 118, 136

A. Sesana, A. Vecchio, and M. Volonteri. Gravitational waves from resolvable massive black hole binary systems and observations with Pulsar Timing Arrays. *Monthly Notices of the Royal Astronomical Society*, 394:2255–2265, April 2009. doi: 10.1111/j.1365-2966.2009.14499.x. 2, 62, 93, 119

A. Sesana, C. Roedig, M. T. Reynolds, and M. Dotti. Multimessenger astronomy with pulsar timing and X-ray observations of massive black hole binaries. *Monthly Notices of the Royal Astronomical Society*, 420:860–877, February 2012. doi: 10.1111/j.1365-2966.2011.20097.x. 130

C. Shang, G. L. Bryan, and Z. Haiman. Supermassive black hole formation by direct collapse: keeping protogalactic gas H_2 free in dark matter haloes with

virial temperatures $T_{vir} >\approx 10^4$ K. *Monthly Notices of the Royal Astronomical Society*, 402:1249–1262, February 2010. doi: 10.1111/j.1365-2966.2009.15960.x. 24

R. M. Shannon, V. Ravi, W. A. Coles, G. Hobbs, M. J. Keith, R. N. Manchester, J. S. B. Wyithe, M. Bailes, N. D. R. Bhat, S. Burke-Spolaor, J. Khoo, Y. Levin, S. Oslowski, J. M. Sarkissian, W. van Straten, J. P. W. Verbiest, and J.-B. Want. Gravitational-wave limits from pulsar timing constrain supermassive black hole evolution. *Science*, 342:334–337, October 2013. 32

S. L. Shapiro and S. A. Teukolsky. *Black holes, white dwarfs, and neutron stars: The physics of compact objects*. Wiley VCH, 1983. 12

X. Siemens, J. Ellis, F. Jenet, and J. D. Romano. The stochastic background: scaling laws and time to detection for pulsar timing arrays. *Classical and Quantum Gravity*, 30(22):224015, November 2013. doi: 10.1088/0264-9381/30/22/224015. 63

J. L. Sievers and ABS Collaboration. The Atacama B-Mode Search. In *American Astronomical Society Meeting Abstracts*, volume 223 of *American Astronomical Society Meeting Abstracts*, page 204.04, January 2014. 4

A. Sillanpaa, S. Haarala, M. J. Valtonen, B. Sundelius, and G. G. Byrd. OJ 287 - Binary pair of supermassive black holes. *The Astrophysical Journal*, 325: 628–634, February 1988. doi: 10.1086/166033. 25

SKA. www.skatelescope.org, 2014. 2, 118

R. Smits, S. J. Tingay, N. Wex, M. Kramer, and B. Stappers. Prospects for

accurate distance measurements of pulsars with the Square Kilometre Array: Enabling fundamental physics. *Astronomy & Astrophysics*, 528:A108, April 2011. doi: 10.1051/0004-6361/201016141. 121, 129

I. H. Stairs. Testing General Relativity with Pulsar Timing. *Living Reviews in Relativity*, 6:5, September 2003. doi: 10.12942/lrr-2003-5. 119

H. Stephani, D. Kramer, M. MacCallum, C. Hoenselaers, and E. Herlt. *Exact solutions of Einstein's field equations*. Cambridge University Press, 2 edition, 2003. 21

K. Stovall, D. R. Lorimer, and R. S. Lynch. Searching for millisecond pulsars: surveys, techniques and prospects. *Classical and Quantum Gravity*, 30(22): 224003, November 2013. doi: 10.1088/0264-9381/30/22/224003. 94

T. Tanaka, K. Menou, and Z. Haiman. Electromagnetic counterparts of supermassive black hole binaries resolved by pulsar timing arrays. *Monthly Notices of the Royal Astronomical Society*, 420:705–719, February 2012. doi: 10.1111/j.1365-2966.2011.20083.x. 130

J. H. Taylor and J. M. Weisberg. A new test of general relativity - Gravitational radiation and the binary pulsar PSR 1913+16. *The Astrophysical Journal*, 253: 908–920, February 1982. doi: 10.1086/159690. 2, 3, 34, 92

S. R. Taylor and J. R. Gair. Searching for anisotropic gravitational-wave backgrounds using pulsar timing arrays. *Physical Review D*, 88(8):084001, October 2013. doi: 10.1103/PhysRevD.88.084001. 73, 89, 96, 135

The POLARBEAR Collaboration, P. A. R. Ade, Y. Akiba, A. E. Anthony,

K. Arnold, M. Atlas, D. Barron, D. Boettger, J. Borrill, S. Chapman, Y. Chinone, M. Dobbs, T. Elleflot, J. Errard, G. Fabbian, C. Feng, D. Flanigan, A. Gilbert, W. Grainger, N. W. Halverson, M. Hasegawa, K. Hattori, M. Hazumi, W. L. Holzapfel, Y. Hori, J. Howard, P. Hyland, Y. Inoue, G. C. Jaehnig, A. H. Jaffe, B. Keating, Z. Kermish, R. Keskitalo, T. Kisner, M. Le Jeune, A. T. Lee, E. M. Leitch, E. Linder, M. Lungu, F. Matsuda, T. Matsumura, X. Meng, N. J. Miller, H. Morii, S. Moyerman, M. J. Myers, M. Navaroli, H. Nishino, H. Paar, J. Peloton, D. Poletti, E. Quealy, G. Rebeiz, C. L. Reichardt, P. L. Richards, C. Ross, I. Schanning, D. E. Schenck, B. D. Sherwin, A. Shimizu, C. Shimmin, M. Shimon, P. Siritanasak, G. Smecher, H. Spieler, N. Stebor, B. Steinbach, R. Stompor, A. Suzuki, S. Takakura, T. Tomaru, B. Wilson, A. Yadav, and O. Zahn. A Measurement of the Cosmic Microwave Background B-Mode Polarization Power Spectrum at Sub-Degree Scales with POLARBEAR. *ArXiv e-prints*, March 2014. 4

M. J. Valtonen, H. J. Lehto, K. Nilsson, J. Heidt, L. O. Takalo, A. Sillanpää, C. Villforth, M. Kidger, G. Poyner, T. Pursimo, S. Zola, J.-H. Wu, X. Zhou, K. Sadakane, M. Drozdz, D. Koziel, D. Marchev, W. Ogloza, C. Porowski, M. Siwak, G. Stachowski, M. Winiarski, V.-P. Hentunen, M. Nissinen, A. Liakos, and S. Dogru. A massive binary black-hole system in OJ287 and a test of general relativity. *Nature*, 452:851–853, April 2008. doi: 10.1038/nature06896. 25

M. J. Valtonen, S. Ciprini, and H. J. Lehto. On the masses of OJ287 black holes. *Monthly Notices of the Royal Astronomical Society*, 427:77–83, November 2012. doi: 10.1111/j.1365-2966.2012.21861.x. 25

R. van Haasteren. Accelerating pulsar timing data analysis. *Monthly Notices of the Royal Astronomical Society*, 429:55–62, February 2013. doi: 10.1093/mnras/sts308. 89

R. van Haasteren, Y. Levin, P. McDonald, and T. Lu. On measuring the gravitational-wave background using Pulsar Timing Arrays. *Monthly Notices of the Royal Astronomical Society*, 395:1005–1014, May 2009. doi: 10.1111/j.1365-2966.2009.14590.x. 49, 73

R. van Haasteren, Y. Levin, G. H. Janssen, K. Lazaridis, M. Kramer, B. W. Stappers, G. Desvignes, M. B. Purver, A. G. Lyne, R. D. Ferdman, A. Jessner, I. Cognard, G. Theureau, N. D'Amico, A. Possenti, M. Burgay, A. Corongiu, J. W. T. Hessels, R. Smits, and J. P. W. Verbiest. Placing limits on the stochastic gravitational-wave background using European Pulsar Timing Array data. *Monthly Notices of the Royal Astronomical Society*, 414:3117–3128, July 2011. doi: 10.1111/j.1365-2966.2011.18613.x. 2, 33, 38, 63, 118

J. P. W. Verbiest, M. Bailes, W. van Straten, G. B. Hobbs, R. T. Edwards, R. N. Manchester, N. D. R. Bhat, J. M. Sarkissian, B. A. Jacoby, and S. R. Kulkarni. Precision Timing of PSR J0437-4715: An Accurate Pulsar Distance, a High Pulsar Mass, and a Limit on the Variation of Newton's Gravitational Constant. *The Astrophysical Journal*, 679:675–680, May 2008. doi: 10.1086/529576. 38

J. P. W. Verbiest, M. Bailes, W. A. Coles, G. B. Hobbs, W. van Straten, D. J. Champion, F. A. Jenet, R. N. Manchester, N. D. R. Bhat, J. M. Sarkissian, D. Yardley, S. Burke-Spolaor, A. W. Hotan, and X. P. You. Timing stability of millisecond pulsars and prospects for gravitational-wave detection. *Monthly*

Notices of the Royal Astronomical Society, 400:951–968, December 2009. doi: 10.1111/j.1365-2966.2009.15508.x. 2, 118

J. P. W. Verbiest, M. Bailes, N. D. R. Bhat, S. Burke-Spolaor, D. J. Champion, W. Coles, G. B. Hobbs, A. W. Hotan, F. Jenet, J. Khoo, K. J. Lee, A. Lommen, R. N. Manchester, S. Oslowski, J. Reynolds, J. Sarkissian, W. van Straten, D. R. B. Yardley, and X. P. You. Status update of the Parkes pulsar timing array. *Classical and Quantum Gravity*, 27(8):084015, April 2010. doi: 10.1088/0264-9381/27/8/084015. 2, 33, 62, 93, 118

M. Volonteri. Formation of supermassive black holes. *The Astronomy and Astrophysics Review*, 18:279–315, July 2010. doi: 10.1007/s00159-010-0029-x. 24, 25, 118

M. Volonteri. The Formation and Evolution of Massive Black Holes. *Science*, 337:544–, August 2012. doi: 10.1126/science.1220843. 25

M. Volonteri, P. Madau, and F. Haardt. The Formation of Galaxy Stellar Cores by the Hierarchical Merging of Supermassive Black Holes. *The Astrophysical Journal*, 593:661–666, August 2003. doi: 10.1086/376722. 63, 119

M. Volonteri, P. Madau, E. Quataert, and M. J. Rees. The Distribution and Cosmic Evolution of Massive Black Hole Spins. *The Astrophysical Journal*, 620:69–77, February 2005. doi: 10.1086/426858. 119

J. M. Weisberg and J. H. Taylor. The Relativistic Binary Pulsar B1913+16: Thirty Years of Observations and Analysis. In F. A. Rasio and I. H. Stairs, editors, *Binary Radio Pulsars*, volume 328 of *Astronomical Society of the Pacific Conference Series*, page 25, July 2005. 3

Z. L. Wen, F. A. Jenet, D. Yardley, G. B. Hobbs, and R. N. Manchester. Constraining the Coalescence Rate of Supermassive Black-hole Binaries Using Pulsar Timing. *The Astrophysical Journal*, 730:29, March 2011. doi: 10.1088/0004-637X/730/1/29. 2, 62, 93, 119

D. J. Whalen and C. L. Fryer. The Formation of Supermassive Black Holes from Low-mass Pop III Seeds. *The Astrophysical Journal Letters*, 756:L19, September 2012. doi: 10.1088/2041-8205/756/1/L19. 24

James T. Wheeler. Gravitational waves. From online notes, `http://www.physics.usu.edu/Wheeler/GenRel2013/Notes/GravitationalWaves.pdf`, 2013. 15, 17

S. D. M. White and M. J. Rees. Core condensation in heavy halos - A two-stage theory for galaxy formation and clustering. *Monthly Notices of the Royal Astronomical Society*, 183:341–358, May 1978. 25

C. M. Will. The Confrontation between General Relativity and Experiment. *Living Reviews in Relativity*, 9:3, March 2006. doi: 10.12942/lrr-2006-3. 119

J. H. Wise, M. J. Turk, and T. Abel. Resolving the Formation of Protogalaxies. II. Central Gravitational Collapse. *The Astrophysical Journal*, 682:745–757, August 2008. doi: 10.1086/588209. 24

J. S. B. Wyithe and A. Loeb. Low-Frequency Gravitational Waves from Massive Black Hole Binaries: Predictions for LISA and Pulsar Timing Arrays. *The Astrophysical Journal*, 590:691–706, June 2003. doi: 10.1086/375187. 2, 62, 93, 119

BIBLIOGRAPHY

D. R. B. Yardley, G. B. Hobbs, F. A. Jenet, J. P. W. Verbiest, Z. L. Wen, R. N. Manchester, W. A. Coles, W. van Straten, M. Bailes, N. D. R. Bhat, S. Burke-Spolaor, D. J. Champion, A. W. Hotan, and J. M. Sarkissian. The sensitivity of the Parkes Pulsar Timing Array to individual sources of gravitational waves. *Monthly Notices of the Royal Astronomical Society*, 407:669–680, September 2010. doi: 10.1111/j.1365-2966.2010.16949.x. 2, 63, 119, 126

J. Yoo, J. Miralda-Escudé, D. H. Weinberg, Z. Zheng, and C. W. Morgan. The Most Massive Black Holes in the Universe: Effects of Mergers in Massive Galaxy Clusters. *The Astrophysical Journal*, 667:813–825, October 2007. doi: 10.1086/521015. 63, 119

M. Zaldarriaga and U. Seljak. Gravitational lensing effect on cosmic microwave background polarization. *Physical Review D*, 58(2):023003, July 1998. doi: 10.1103/PhysRevD.58.023003. 4

W. Zhao. Constraint on the early Universe by relic gravitational waves: From pulsar timing observations. *Physical Review D*, 83(10):104021, May 2011. doi: 10.1103/PhysRevD.83.104021. 62, 93